UNIVERSITÀ DEGLI STUDI DI ROMA TOR VERGATA

MACROAREA DI SCIENZE MATEMATICHE, FISICHE E NATURALI

MASTER'S DEGREE IN PHYSICS

Curriculum in Astrophysics and Space Science

Shedding Light on Active Galactic Nuclei in the Early Universe: Investigating the Average X-ray Spectrum of Quasars at the Epoch of Reionization

Supervisors

Prof. Francesco Tombesi
Department of Physics
Tor Vergata University of Rome

Prof. Luka Č. Popović
Faculty of Mathematics
University of Belgrade

Dr. Luca Zappacosta
INAF - Astronomical Observatory of Rome

Author

Sagarika Paul
Matricola: 0325657

Anno Accademico 2023/2024

MASTER IN ASTROPHYSICS AND SPACE SCIENCE

Erasmus Mundus Master
in Astrophysics and Space Science

Master Thesis

Shedding Light on Active Galactic Nuclei in the Early Universe: Investigating the Average X-ray Spectrum of Quasars at the Epoch of Reionization

Supervisors

Prof. Francesco Tombesi
Department of Physics
Tor Vergata University of Rome

Prof. Luka Č. Popović
Faculty of Mathematics
University of Belgrade

Dr. Luca Zappacosta
INAF - Astronomical Observatory of Rome

Author

Sagarika Paul
Matricola: 0325657

Academic Year 2023/2024

TOR VERGATA UNIVERSITÀ DEGLI STUDI DI ROMA
University of Bremen
UNIVERSITÉ CÔTE D'AZUR
UNIVERSITY OF BELGRADE
Funded by the European Union

This master's thesis is submitted in partial fulfillment of the requirements for the degree *Fisica Curriculum Erasmus Mundus* as part of a multiple degree awarded in the framework of the Erasmus Mundus Joint Master in Astrophysics and Space Science − MASS jointly delivered by a Consortium of four Universities: Tor Vergata University of Rome, University of Belgrade, University of Bremen, and Université Cote d'Azur, regulated by the MASS Consortium Agreement and funded by the EU under the call ERASMUS-EDU-2021-PEX-EMJM-MOB.

"*Too impressive to ignore,*
Too fleeting to enshrine."
-Michael Stevens, Vsauce

Contents

Acknowledgments vii

Abstract ix

1 What are Active Galactic Nuclei? 1

1.1 Classification of AGNs . . . 2

1.1.1 UV/Optical Classification . . . 2

1.1.2 X-ray Classification . . . 3

1.1.3 Radio Classification . . . 5

1.1.4 Quasars . . . 5

1.1.5 Blazars . . . 8

1.2 The Unified Model . . . 9

1.2.1 The Central Supermassive Black Hole . . . 10

1.2.2 Accretion Disk . . . 11

1.2.3 Corona . . . 13

1.2.4 Broad and Narrow Line Regions . . . 13

1.2.5 The Obscuring Torus . . . 14

1.2.6 Mass Outflows and Winds . . . 15

1.2.7 Relativistic Jets . . . 15

1.3 The AGN Spectral Energy Distribution . . . 16

1.3.1 UV Disk Emission . . . 16

1.3.2 X-ray Coronal Emission . . . 17

1.3.3 IR Emission from Dusty Torus . . . 20

1.3.4 Radio Emission . . . 22

1.3.5 Gamma Ray Emission . . . 23
1.4 The X-ray Emission of AGNs . . . 24
1.5 SMBH Mass Estimates . . . 29
1.5.1 Dynamical Mass Estimates . . . 30
1.5.2 Reverberation Mapping . . . 33
1.5.3 Single Epoch Virial Mass Estimates . . . 35
1.6 AGN Formation, Co-Evolution and Feedback Mechanism . . . 37

2 Quasars at the Epoch of Reionization **39**
2.1 The Growth of SMBHs . . . 43
2.2 Multiwavelength Properties of $z > 6$ QSO . . . 46
2.3 The HYPERION Sample . . . 50

3 The XMM-Newton X-ray Observatory and The XMM Heritage Program on HYPERION **57**
3.1 Basics principles of X-ray astronomy . . . 57
3.2 The Observatory . . . 63
3.2.1 The European Photon Imaging Camera (EPIC) . . . 65
3.2.2 Reflection Grating Spectrometers (RGS) . . . 67
3.2.3 The Optical Monitor (OM) . . . 67
3.3 The XMM Heritage Program on HYPERION . . . 68

4 The Average Spectrum of Quasars at $z > 6$ **74**
4.1 Analysis Methods of Limited Quality X-ray Spectra . . . 74
4.2 Combining the X-ray Spectra . . . 75
4.3 Testing the Spectral Combination Procedure . . . 80
4.4 Averaging the HYPERION pn Spectra . . . 88

5 Results and Discussion **109**
5.1 Single QSOs X-ray Properties . . . 109
5.2 On the Average X-ray Constraints . . . 113

5.3 Looking for Additional Spectral Components on the Average X-ray Spectrum 118
5.4 The Implication of Steep Spectra 122

6 Conclusions **125**

References 128

Acknowledgments

The Erasmus Mundus - MASS program has been an extraordinary experience and over the course of the past two years, innumerable people have contributed to my growth.

I would like to thank my supervisors, Prof. Francesco Tombesi, Prof. Luka Č. Popović, and Dr. Luca Zappacosta. I am especially grateful to Prof. Tombesi for his guidance and support, and to Dr. Zappacosta, whose unwavering patience and mentorship throughout the course of this thesis have been instrumental in its completion. I am thankful for their encouragement and support, which greatly enriched my academic journey.

I sincerely appreciate the efforts of the MASS Project Office, specifically Dr. Adalia Caroli. Without her help studying and living in Italy would have been much harder than it was. There are sayings about there being light at the end of the tunnel, but she is the guiding light in a dark tunnel.

I would like to thank my classmates of MASS Edition 1, or "MASS OG" as we like to call ourselves. Struggling, persevering, and growing together has not only pushed me to my limits but also shown me what I am truly capable of. We have had a great run and I am really glad that I got to share an amazing experience with them. I would especially like to thank my very good friend, Sreeparna, who has stood by me, come hell or high water, for the past 10 years. I look forward to many more years of friendship and shared adventures.

I would like to extend my gratitude to the MASS committee; professors, administrative staff, and friends from all the consortium universities. Their incredible support made the transitions between universities smooth and manageable. Their interest and dedication towards our holistic well-being and growth have made the past two years incredibly adventurous and enriching.

I would also like to thank my parents and my extended family and friends back in India. Without their incredible support I wouldn't have thrived, not just in this program, but in life itself. Words will never be enough to express my gratitude to them. I can only aspire to be the person they already think I am so that I can make them proud.

Lastly, and as significant as everything else, I should thank my younger self who dared to dream of becoming an astrophysicist. The journey hasn't been easy but I am sure that the young, stubborn girl, who brought an advanced book on astrophysics when she was 12, would be proud of who I have become.

The analysis and results presented in this work are based on observations obtained with *XMM-Newton* an ESA science mission with instruments and contributions directly funded by ESA Member States and NASA. We thank the *XMM-Newton* Science Operation Centre and Norbert Schartel for their help, prompt support and advice for the scheduling and optimisation of the XMM-HYPERION program. We acknowledge financial support from the Bando Ricerca Fondamentale INAF 2022 Large Grant "Toward an holistic view of the Titans: multi-band observations of z $>$ 6 QSOs powered by greedy supermassive black holes".

Sagarika Paul acknowledges support through an Erasmus Mundus Joint Master EMJM scholarship funded by the European Union in the framework of the Erasmus+, Erasmus Mundus Joint Master in Astrophysics and Space Science – MASS. Views and opinions expressed are however those of the author(s) only and do not necessarily reflect those of the European Union or granting authority European Education and Culture Executive Agency (EACEA). Neither the European Union nor the granting authority can be held responsible for them.

Abstract

Quasars (QSOs) are luminous ($> 10^{45}$ erg/s) galactic nuclei powered by accretion of matter at high rates onto a central supermassive black hole (SMBH) of mass $> 10^8 M_\odot$. The existence of luminous QSOs powered by SMBHs with masses $> 10^9 M_\odot$ at the Epoch of Reionization (EoR; i.e, z > 6) when the universe was < 1 Gry old challenges models of early SMBH formation and growth.

The aim of this thesis is to characterize the average nuclear X-ray properties of luminous $z = 6$ - 7.5 QSOs constituting the HYPERION QSO sample. This sample is specifically selected to include QSOs with SMBHs which experienced the most extreme and rapid growth during their assembly at EoR. In this way we can study the nature of the most puzzling sources for SMBH formation models. The HYPERION sample of QSOs represents the best available data for the most distant QSOs for such a large sample of sources at the EoR. This sample is part of the Heritage XMM program designed specifically to obtain constraints of nuclear properties of early QSOs.

The QSO X-ray emission takes the form of a power-law spectrum with an exponential cutoff at ~ 100 keV energies and is produced by Comptonization of accretion disk UV photons in a compact corona of hot electrons. The corona in luminous QSOs is estimated to be located a few tens of gravitational radii from the growing SMBH and hence characterizing its X-ray emission can give clues on the inner nuclei of these sources and on their nature. We perform a preliminary spectral analysis of the single source spectra from EPIC-pn, the most sensitive detector on-board the *XMM-Newton*. The analysis focuses on the ~ 3 - 50 keV rest-frame energy band allowing us to characterize the true hard X-ray emission coming from few tens of gravitational radii from the SMBH. We report, on average, spectra modeled with power-laws with slopes steeper than that reported for the bulk of the QSO population at lower redshifts (i.e. $z < 6$)

with a mean Γ value for the entire sample as $\Gamma = 2.37 \pm 0.1$.

We implement an algorithm to create 3 - 50 keV rest-frame X-ray average spectrum of these 18 QSOs free from Galactic interstellar medium absorption. We performed extensive simulations to test this method for the limited quality spectra available for the single HYPERION QSO. An average spectrum can constrain the spectral properties and evaluate possible deviations from the simple power-law model and hence the existence of additional spectral components since it gives a higher signal-to-noise ratio. For the average spectrum we report a steep photon index with $\Gamma = 2.54 \pm 0.2$. This measure average Γ is inconsistent with the canonical value ($\Gamma = 1.8$ - 2.0) reported for QSOs at $z < 6$. This slope is significantly steeper than what is reported in QSOs at lower$-z$ that are similar to our sources in terms of luminosity or accretion rate, suggesting a genuine redshift evolution.

We also implement an alternative spectral model assuming that the slope is due to the presence of a relatively low energy exponential cutoff over a standard $\Gamma = 1.9$ power-law. In this case we measured a very low energy cutoff at $\sim$ 20 keV which is rarely reported at $z < 6$ and at similar luminosities. Both steep Γ and low energy cutoff are indications of a low temperature corona possibly due to very high accretion regime enhancing the Compton cooling of the corona in these sources.

We don't find remarkable deviations from a canonical power-law model with the only exception of a relatively broad and low significance emission feature at $\sim$ 20 - 30 keV of unknown origin (physical or instrumental) which needs to be confirmed with more data.

In Chapter 1, the fundamental properties of Active Galactic Nuclei (AGNs) are explained and in Chapter 2 we provide an overview of high-z QSOs at the EoR, including details about the dataset used in this work. Following this, in Chapter 3, we cover the essential concepts of X-ray astronomy and offer an introduction to the *XMM-Newton* observatory, emphasizing its role and relevance to our study. In Chapter 4 we discuss our procedure to create the average spectrum and the method with extensive simulations and analysis. In Chapters 5 and 6 we discuss our findings and conclusions.

Chapter 1

What are Active Galactic Nuclei?

Active Galactic Nuclei (AGNs) are extremely bright regions at the center of galaxies outshining the rest of the galaxy. These are the most luminous persistent sources of electromagnetic (EM) radiation in the universe. AGNs are powered by accretion processes onto a central supermassive black holes (SMBHs) with masses in the range of $10^6 - 10^{10} M_\odot$. The gravitational potential of the accreting material is partly converted into radiation and the rate of emission or bolometric luminosity (L_{bol}) can be expressed as $L_{bol} = \eta \dot{M} c^2$ where η is the radiative efficiency, i.e., the mass-energy conversion efficiency, $\dot{M}$ is the mass accretion rate and c is the speed of light. η is a black hole (BH) spin dependent parameter with an expected range between 0.05 and 0.42 (Kerr 1963, Thorne 1974). For non rotating BH, η is estimated to be 0.1. A standard length scale used to describe the proximity of the BH is the Schwarzschild radius which indicates the size of the BH event horizon. For a non rotating BH, $R_s = 2GM_{BH}/c^2$. Accretion onto a BH is limited by the effects of radiation pressure experienced by the infalling matter. This has a direct consequence on the observed luminosity and it has a theoretical upper limit, which was first pointed out by Eddington (1920). The Eddington limit is calculated, assuming spherical symmetry and fully ionized hydrogen gas accreting onto a BH with mass M_{BH}, matching the outward radiation force to the gravity force:

$$F_{rad} = \frac{L_{bol}\sigma_T}{4\pi r^2 c} = F_{grav} = \frac{GM_{BH}m_p}{r^2} \tag{1.1}$$

In this case the bolometric luminosity reaches a luminosity limit called Eddington

luminosity, L_{Edd}

$$L_{Edd} = \frac{4\pi G M_{BH} m_p c}{\sigma_T} \sim 1.3 \times 10^{38} \frac{M_{BH}}{M_\odot} ergs/s \tag{1.2}$$

where G is the gravitational constant, m_p is the proton mass and σ_T is the Thomson cross-section for an electron. The AGN accretion activity is usually quantified by the Eddington ratio (λ_{Edd}) where $\lambda_{Edd} = L_{bol}/L_{Edd}$ is the ratio between the AGN bolometric luminosity and the Eddington luminosity. So the Eddington ratio is directly related with the accretion rate $\dot{M}$ because $\lambda_{Edd} \propto \dot{M}/M_{BH} \propto \dot{M}/M_{Edd}$ where M_{BH} is the black hole mass, $\dot{M}_{Edd} = L_{Edd}/(\eta c^2)$, and η is the radiative efficiency.

The manifestations of this accretion process can be observed across the entire EM spectrum. Based on the observational properties, we discuss next, the classification of AGNs.

1.1 Classification of AGNs

1.1.1 UV/Optical Classification

Based on optical emission lines, AGNs are classified as broad-line AGNs (Type 1 AGNs) with at least one broad emission line (Full Width at Half Maxima (FWHM) = 2000 km/s) or as narrow-line AGNs (Type 2 AGNs) with only narrow lines. The most common class of AGNs observed in the local universe ($z \leq 0.1$) are *Seyfert galaxies*. These are characterised by a bright, central, point-like core with respect to non-active galaxies. Because of their proximity to us, we can observe them in great detail with spectroscopy and imaging. This has allowed us to study most of the typical AGN physical processes. Seyfert galaxies have luminosities of the order of 10^{42} -10^{44} erg/s , which is comparable to the luminosities of an entire galaxy. Quasi-Stellar Objects (QSOs, Schmidt and Green 1983) appear as point-like and have a luminosity from 10 to 10^5 times greater than the host galaxy which is therefore outshined by the core emission. The distinction between Seyferts and QSOs is based on a luminosity threshold. A QSO has $L_{bol} > 10^{46}$ erg/s, with an absolute magnitude of $M_B <$ - 23 (Véron-Cetty and Véron, 2003). Today, the identification of Seyfert galaxies and QSOs are based

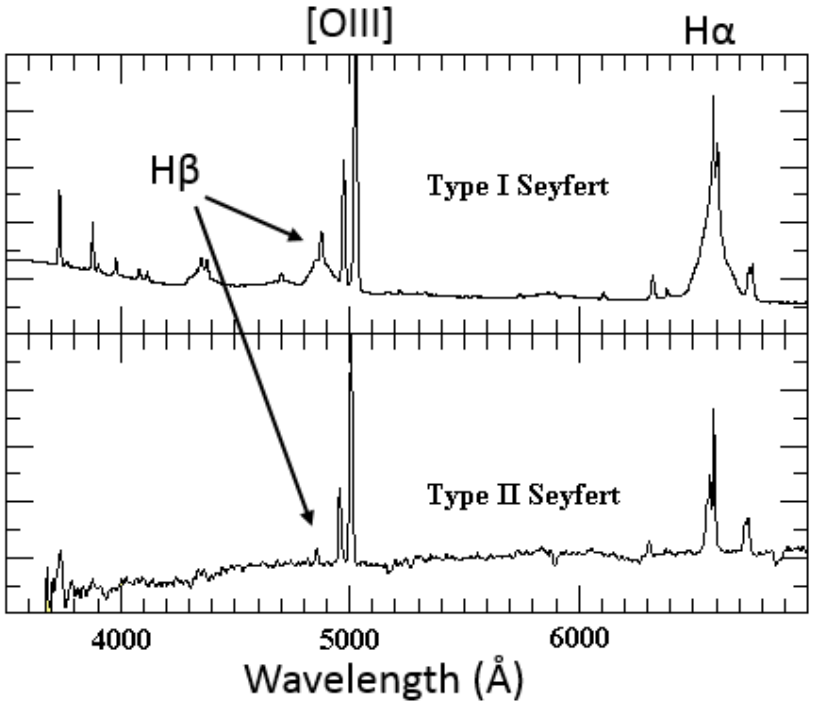

Figure 1.1: An example of Seyfert-1 and Seyfert-2 spectra highlighting their differences. The broad Hβ and Hα lines are only present in type-1 Seyferts. The strong [OIII] emission line is narrow in both cases. Flux is in arbitrary units and wavelength is in $\mathring{A}$. Image from Morgan, 2002.

on spectral signatures of the AGN cores where we see highly ionized emission lines. There are two distinct classes of Seyferts and QSOs based on the width of the narrow (forbidden) and Balmer lines and then these characteristics were identified with the Narrow Line Region (NLR) and Broad Line Region (BLR) of an AGN.

In Type 1 AGNs, Balmer lines, Hα, Hβ and Hγ lines appear broader (i.e. FWHM $>$ 2000 - 3000 km/s) than the forbidded lines ([O II], [O III], [N II], [N III]). So we can see both BLR and NLR. In Type 2 AGNs, both the forbidden lines and Balmer lines have narrow widths ($\approx$ hundreds of km/s) so, mostly we observe the NLR. Figure 1.1 highlights the difference between type 1 and 2 Seyfert galaxies.

1.1.2 X-ray Classification

The X-ray opacity of atomic gas depends strongly on wavelength. Absorption is conventionally measured as an equivalent column density of hydrogen along line of sight (N_H). At around a column density of $1.5\times\ 10^{24}$ cm^{-2} the neutral or lowly ionized gas is Compton thick, which prevents the transmission of almost all the X-ray radiation below

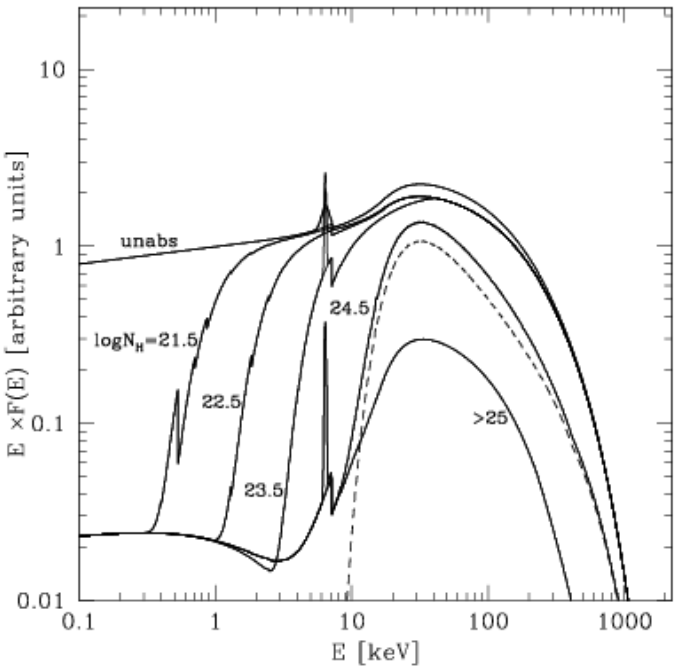

Figure 1.2: The AGN X-ray spectra with different absorptions assumed in the model. Solid lines from top to bottom: $N_H = 0$ (i.e. unabsorbed AGN), $\log N_H = 21.5$, 22.5, 23.5, 24.5, > 25. A primary powerlaw with $\Gamma = 1.9$ and cut off energy 200 keV is assumed. See (Gilli et al., 2007) and references therein.

$\sim$ 8 keV. In both local (Risaliti et al., 1999) and distant sources (Norman et al., 2002), we see very low ($N_H \leq 10^{21}$ cm^{-2}) to very high column densities ($N_H \geq 10^{24}$ cm^{-2}). Based on intrinsic absorption measurement in the soft X-ray portion of the spectrum ($\leq$ 2 keV), we classify sources as obscured or unobscured. A column density of $\sim 10^{22}$ cm^{-2} is typically used as a threshold. Generally, there is a link that unobscured AGNs in the X-ray are Seyfert 1 galaxies and obscured AGNs belong to Seyfert 2 AGN classification. But this is not always true. At least a fraction of the Type 2 AGN population appears to be unobscured and intrinsically lacking a BLR (e.g. Bianchi et al. 2012). Figure 1.2 shows the AGN X-ray spectrum of a model with different absorption assumed. Some sources show variation in intrinsic absorption with time and thereforew undergo a change in the X-ray classification. These sources are known as the *changing look AGNs* (Matt et al., 2003).

Narrow-Line Seyfert 1 galaxies (NLSy1s), a subset of the Seyfert 1 galaxies, are strong X-ray emitters but they have broad Hα lines and narrow Hβ lines. SMBHs in NLSy1s appear to be, on average, less massive than other Seyferts, being in the

range 10^5 - 10^7 $M_\odot$. Yet their bolometric luminosities are comparable leading to the conclusion that NLSy1s are accreting at a higher rate, closer to the Eddington limit than other Seyfert galaxies. NLSy1s also show strong X-ray variability, but they vary only marginally in the UV band.

1.1.3 Radio Classification

AGNs which are characterized by a significant emission in the radio band from the relativistic jets and their related phenomenon are known as Radio Galaxies. The most commonly used classification of Radio Galaxies are based on the appearance and intensity of the extended emission source. This is known as the Fanaroff-Riley (FR) Classification (Fanaroff and Riley, 1974). The low-luminosity FR I have a radio emission peak near the nucleus and the high-luminosity FR II have radio lobes with prominent hot spots and bright outer edges. Figure 1.3 shows the two types of Radio Galaxies. The origin of this dichotomy is still debatable but it is possible that the jets in FR I are not as collimated or/and powerful as in FR II (a threshold is $L_R(175MHz) = 10^{32}$ erg/s/Hz). When studying the AGN cores in Radio Galaxies, one finds similarities to the cores of Seyfert galaxies. Both Seyfert 1 and Seyfert 2 optical types are present in Radio Galaxies, and also the intermediate Seyfert types. Radio Galaxies with a Type 2 AGN are referred to as Narrow-Line Radio Galaxies (NLRGs), while those with broad optical-UV lines are called Broad-Line Radio Galaxies (BLRGs).

1.1.4 Quasars

In the late 1950s and early 1960s, radio telescope surveys led to the discovery of Quasi-Stellar Objects (QSOs) among Radio Galaxies. Optical follow-up confirmed that these as extra-galactic sources revealed strong emission lines (Balmer lines, but redshifted by 16%) implying that these were extra-galactic sources with enormous luminosity. Spectroscopy of 3C (the third Cambridge catalog) galaxies revealed distant quasars, suspected to be distant counterparts of nearby Seyfert galaxies. As the gap between Seyferts and quasars were bridged, an arbitrary dividing line based on absolute magnitudes was introduced and Seyfert galaxies with absolute magnitude brighter than $<$ - 23 mag were referred to as QSOs. QSOs have luminosities exceeding 10^{44} erg/s and

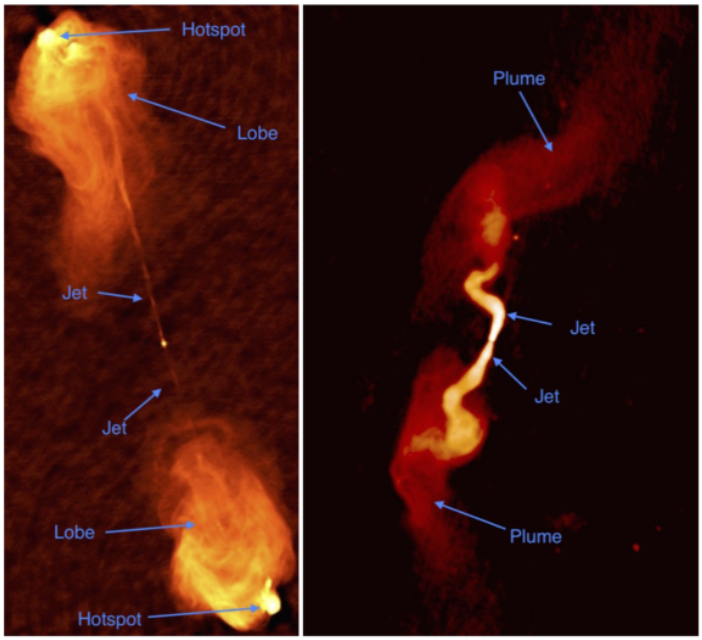

Figure 1.3: VLA (Very Large Array) radio maps of powerful FR II radio jets in CygnusA (left) and the weak FRI jets in 3C 31 (right). The jets are launched and powered by a black hole feeding at the centre of a galaxy. (To get a sense of the immense scale of these objects, the tiny dot at the centre of the left image is the galaxy from which the FRII jet is launched). Lighter colours correspond to regions with strong radio emission, the darker colours correspond to regions with weak or no radio emission. Note that the colour scale used in these images is not the same and the FRII jets on the left emit significantly stronger radio emission compared to the FRI jets on the right. image credit: NRAO/AUI.

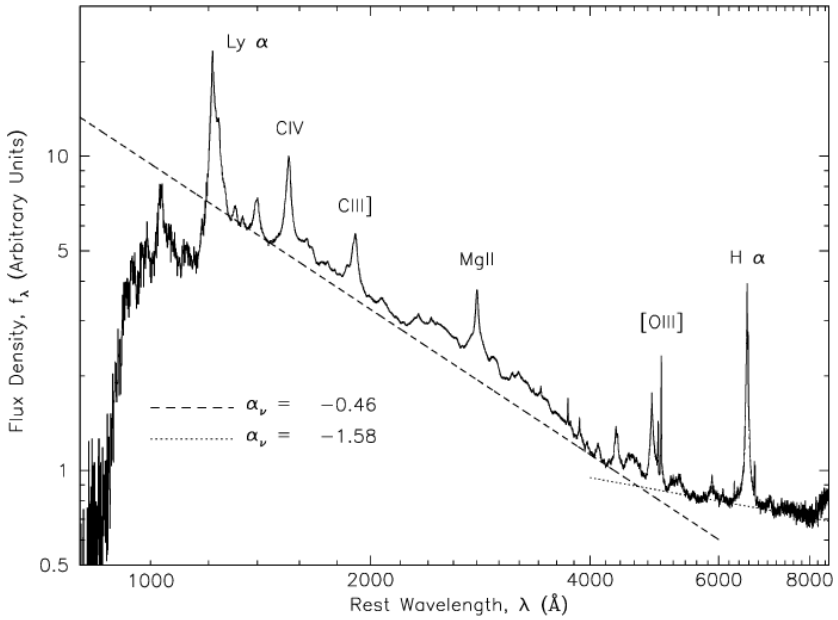

Figure 1.4: Composite quasar spectrum using median combining. Power-law fits to the estimated continuum flux are shown. The resolution of the input spectra is $\sim$ 1800, which gives a wavelength resolution of about 1 $\AA$ in the rest frame.

can go up to 10^{47} erg/s making them significantly brighter than galaxies. QSOs are distinguishable by their blue appearance due to the big blue bump in their spectra from the accretion disk surrounding the central SMBH. Figure 1.4 shows a composite spectrum based on 2200 QSOs from the Sloan Digital Sky Survey (Berk et al., 2001).

About 90% of all QSOs are radio quiet and the transition between Radio Quiet and Radio Loud is not smooth. Radio Galaxies are classified on the basis of flux ratio between the radio band over the optical band. This is given as $R = f_{5GHz}/f_{2500\AA}$. If a source has $R > 10$, the source is considered *Radio Loud (RL)* while for $0.1 < R < 1$ it is considered *Radio Quiet (RQ)*. Only about 10% of all QSOs are RL and there is no smooth transition between the two classes. RL QSOs are further divided into radio bright *Flat Spectrum Radio Quasars* (FSRQs) and *Steep Spectrum Radio Quasars* (SSRQs) based on their radio spectral shape. FSRQs have a compact radio structure and are often referred to as Blazars while SSRQs are dominated by radio lobe emission. In addition to those we also know about another class of QSOs called *Broad Absorption Line Quasars (BAL QSOs)*. BAL QSOs are usually radio quiet and X-ray weak but they show powerful winds and they represent $\sim$ 15 - 20% of RQ QSOs. Their detection frequency indicates that the winds are an evolutionary phenomenon, independent on

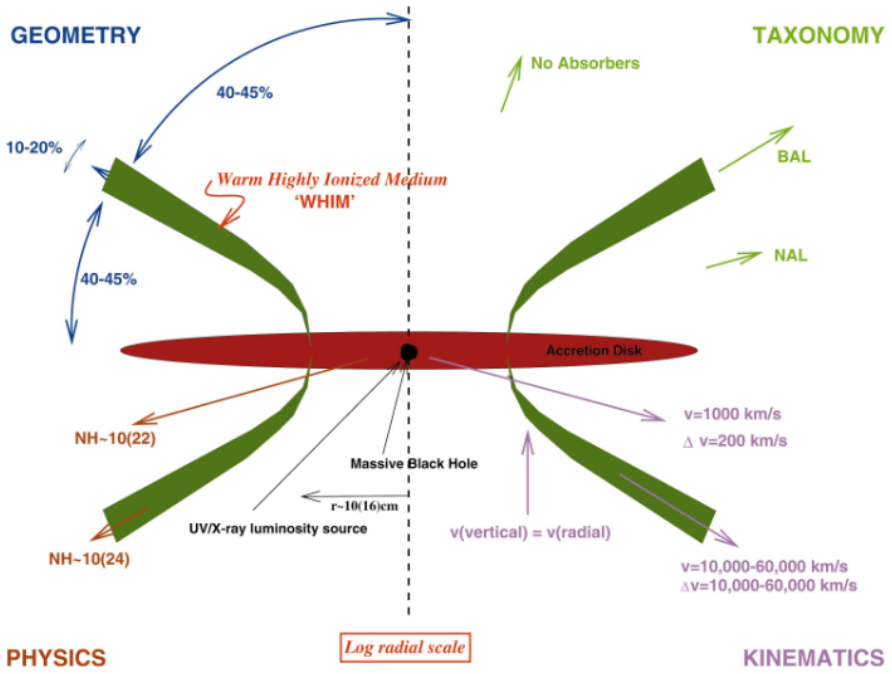

Figure 1.5: Proposed structure for QSOs. The four symmetric quadrants illustrate the following (clockwise from top left) : the opening angles of the structure, the spectroscopic appearance to a distant observer at various angles, the outfow velocities along different lines of sight, and some representative radii (appropriate for the Seyfert 1 galaxy NGC 5548) and some typical column densities. Figure from (Elvis, 2000)

orientation, and are present with a certain duty cycle and/or winds are present in every quasar, but cover only $\sim 20\%$ of the solid angle. Figure 1.5 shows the a possible structure for quasars suggested by (Elvis, 2000).

1.1.5 Blazars

Blazars, a subset of QSOs, are RL sources with relativistic jets pointing towards the observer. They exhibit high variability and are prominent emitters from radio to very high energies above 1 TeV. Blazars are always RL and comprise a few percent of the overall AGN population. They are subdivided into *BL Lac* and *FSRQs*. BL Lac objects are continuum dominated and almost featureless (see Figure 1.6) but FSRQs show broad emission lines like normal quasars (but the lines can disappear if the continuum from the jet is too high). Blazars, such as FSRQs and BL Lacs, are distinguished by the equivalent width of optical emission lines, with a cut-off at 5 $\AA$ for BL Lacs. Blazars exhibit highly varied emissions across the electromagnetic spectrum. They are

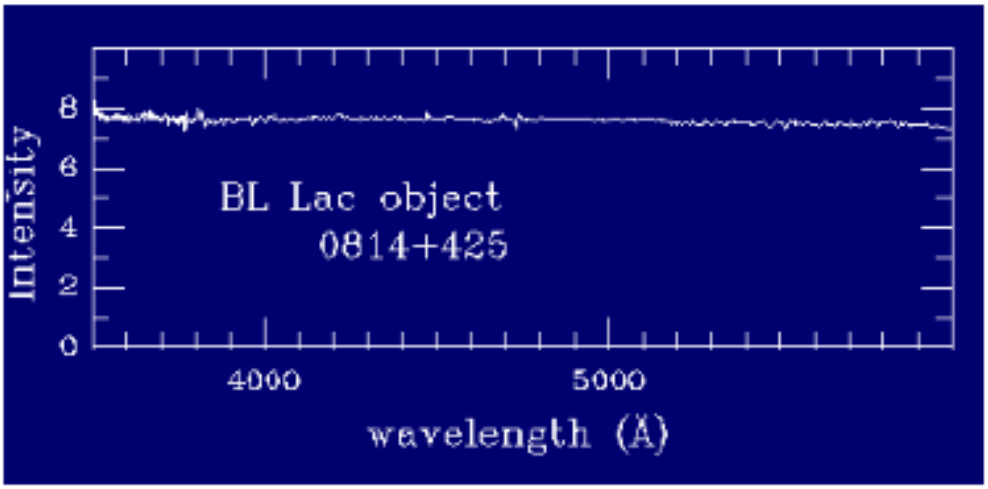

Figure 1.6: Typical spectrum of a BL Lac.

identified by strong and polarized radio emission or sources with a high flux in the X-ray band compared to their optical emission. These blazars show significant variations on different time-scales, including intraday variability (IDV). BL Lac objects, particularly X-ray selected ones, experience periods of quiescence interrupted by intense outbursts, with variability dependent on their spectral type.

1.2 The Unified Model

AGNs refer to a broad class of objects that were classified historically based on how they were viewed in the different waveband of the EM spectrum. We discuss here a broad but standard classification for each class and their observational properties.

A recurring and important question in the study of AGNs is whether the distinct appearances of the AGN phenomenon can be explained by a common underlying model or if the classes are intrinsically distinct. In mid 1980s, Antonucci and Miller (1985) first reported by means of spectro-polarimetric observations, that NGC 1068 (prototype of Type 2 Seyfert galaxy) showed a very broad systemic Balmer line ($\sim$ 7500 km s^{-1}) and also permitted Fe II lines, indicating a very close similarity with Type 1 Seyfert galaxies. In this paper they said, "We favor an interpretation in which the continuum source and broad line clouds are located inside a thick disk, with electrons above and below the disk scattering continuum and broad line photons in to the line of sight". This

paper coincides with the beginning of the "Unification Era" that attempts to explain the spectral features of an AGN as a function of its orientation with respect to line of sight and obscuration of the inner regions. Figure 1.7 shows a schematic representation of the unified model.

The AGN structure includes, amongst other components, the Broad Line Region (BLR) and the Narrow Line Region (NLR) and the obscuring torus. The torus is thought to be a doughnut-shaped structure of dust and gas that surrounds the central SMBH. This torus can block or obscure the view of the BLR and the central engine, depending on the observer's line of sight. If there exists an optically thick torus around the accretion disk and the BLR, then we see an absence of broad emission lines in the edge on view, (i.e., the accretion disk axis is perpendicular to the observer line of sight) and for these galaxies the BLR is hidden. Alternatively, if the AGN is seen face on, then the BLR is visible. Since NLR is outside the torus, emission from this is still visible for views from all orientation. The viewing angle and the torus geometry are therefore the determining factors for the Type 1 and 2 optical classification mentioned before.

Furthermore, the theory distinguishes between Radio Loud and Radio Quiet AGNs based on the presence or absence of powerful relativistic jets. RL and RQ AGNs can be differentiated by the presence or absence of relativistic jet along line of sight. If the jet is exactly along the LOS, the jet luminosity is enhanced by relativistic beaming which also causes the strong variability and polarization observed in blazar emission. Observing the jet from increasing inclination implies that the sources are recognized first as Radio Loud QSOs and subsequently as Radio Galaxies.

Below we discuss the components of an AGN.

1.2.1 The Central Supermassive Black Hole

It has been assumed that AGN must be powered by accretion onto SMBH at the dynamical centers of their host galaxies. These central BH are estimated to have masses in the range $M_{BH} = 10^6$ - $10^{10} M_{\odot}$. Mounting evidence shows that SMBHs reside at the center of almost all galaxies. The most basic characteristic of a BH is the presence of event horizon which is the boundary through which matter and light can fall towards the center of the BH but never re-emerge. At this boundary, the gravitational

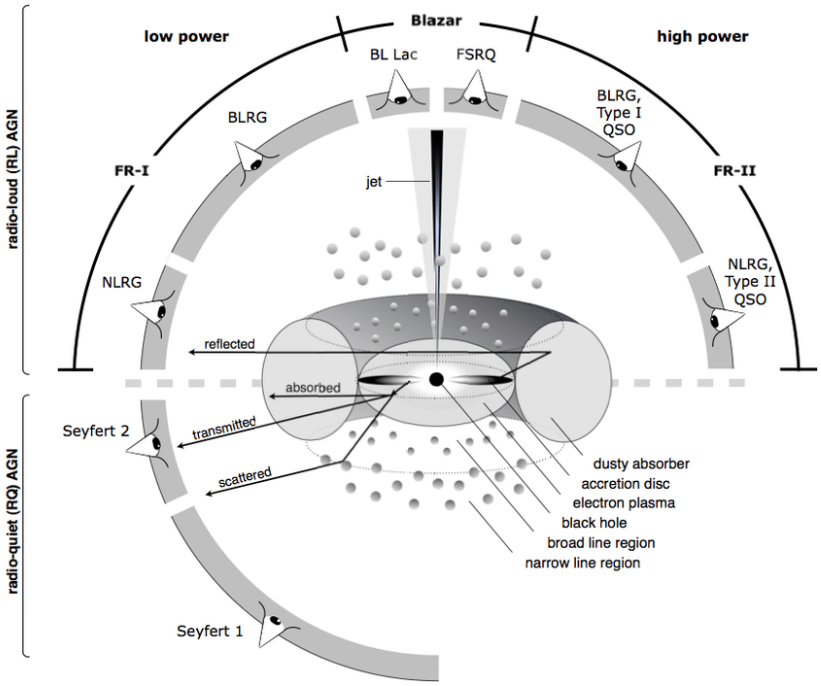

Figure 1.7: The unified model of Active Galactic Nuclei (AGNs) by Beckmann and Shrader (2012).

escape velocity is equal to the speed of light. This is called a Schwarzchild radius for a non-rotating BH and is given as, $R_S = \frac{2GM_{BH}}{c^2}$. The no-hair theorem states that all stationary black hole solutions of the Einstein–Maxwell equations of gravitation and electromagnetism in general relativity can be completely characterized by only three independent externally observable classical parameters: mass (M_{BH}), electric charge (Q), and angular momentum (J). J is usually characterized in terms of dimensionless spin parameter $a = cJ/GM_{BH}^2$ where $0 \leq |a| \leq 1$ where a = 0 indicates a non rotating BH or Schwarzschild BH, while a = 1 is a maximally spinning Kerr BH. BH usually are expected to have Q = 0 because it is discharged on the surrounding plasma and depending on J, we go from Schwarzchild BH (non-rotating, spherically symmetric horizon) to Kerr BH (maximally spinning).

1.2.2 Accretion Disk

The basic mechanism underlying the AGN central engine is accretion. Matter falls onto the compact object, a SMBH, leading to the conversion of gravitational potential energy to EM radiation. The simplest configuration that we can consider is an

approximately spherically symmetric accretion flow onto the black hole. This type of "spherical accretion" is often referred to as Bondi accretion (Bondi, 1952) but it is an extremely idealistic model. It is unlikely to be significant in powering luminous AGNs because η is low and in the absence of angular momentum, the plasma falls onto the SMBH before it had time to radiate its thermal energy. More realistic models include the "alpha disk" or standard accretion disk model which assumes a geometrically thin and optically thick accretion disks with a constant rate of accretion. This was proposed in the 1970s by Shakura and Sunyaev (1973). The disk material in this case is optically thick and the emitted spectrum at radius, r, is a black body with temperature T(r). In this case the disk temperature, $T(r) \propto r^{-3/4}$ implying that the EM disk emission moves up from the UV to the soft X-ray band going from SMBH to stellar mass BH. If the accretion rate significantly exceeds the Eddington value, and/or the cooling of the disk becomes highly inefficient, the flow cannot be vertically confined and the standard alpha disk model is not stable. Toroidal or thick disk geometries are then required to model the accretion flow, depending on whether the pressure is dominated by radiation or by hot gas (e.g., Abramowicz and Fragile 2013). The conditions in thick disks may also be more favorable with respect to standard disks for the formation of powerful winds outflows and jets. These disks are called advection-dominated accretion flow (ADAF) disks and are geometrically thick and optically thin. The accreting gas is heated viscously and cooled radiatively, but in an inefficient way. Any excess heat is stored in the gas and then transported in the flow. This process represent an "advection" mechanism for the transport of thermal energy. The conditions for an ADAF disk to form requires a low (sub-Eddington) accretion rate and a very low gas opacity. In ADAFs, an element of gas is unable to radiate its thermal energy in less time than it takes it to be transported through the disk into the black hole. ADAF disks are shown to be likely associated to the production of jets. The structure of the AD is mainly determined by the ratio, $\lambda = \dot{M}/\dot{M_{Edd}}$. For $\lambda << 1$, the disk becomes optically thin and cooling of the disk is ineffective. This creates and ADAF. For medium accretion rates $\lambda < 1$ and high opacities, the AD is thin and $\eta = 0.1$ resulting in an α disk. For $\lambda >> 1$ and high opacities, radiation is partially trapped by the accreting material and the disk expands vertically into a "radiation torus" or a thick disk which radiates ineffectively. Figure

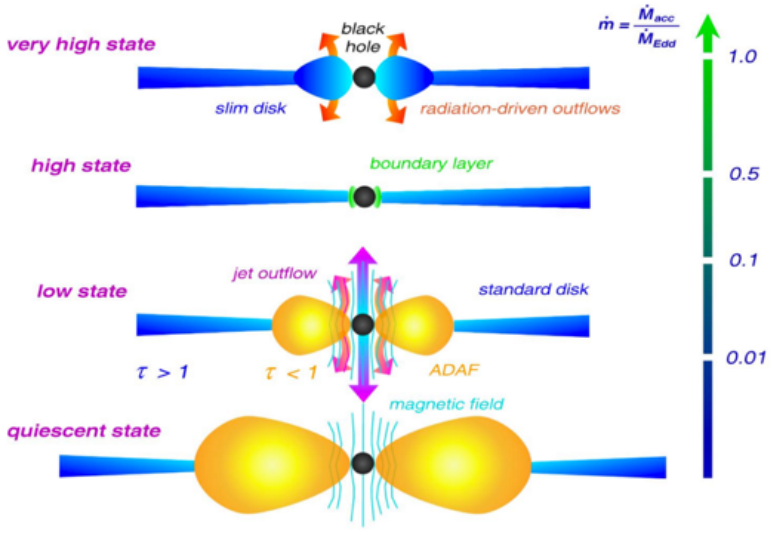

Figure 1.8: The schematic figure of the state of a black hole accretion disk (Müller 2004). The label on the left of each model indicates the X-ray state.

1.8 shows the different states of a black hole accretion disk as discussed.

1.2.3 Corona

The SMBH is surrounded by the X-ray corona which is a region of hot electrons responsible for X-ray emission via Inverse Compton scattering of optical/UV photons from the AD. The corona is often treated as a point-like source above the BH's spin axis for modelling (Lamp-post geometry, Miniutti and Fabian 2004). The actual shape might be more likely to be extended or outflowing rather than being point-like (Wilkins et al., 2016). We discuss in more details the physics of the corona in Section 1.4.

1.2.4 Broad and Narrow Line Regions

One of the distinguishing observational properties of AGN in the optical/UV band is the presence of (cosmologically) redshifted and time variable emission lines with Doppler widths from 10^3 to 10^4 km/s. The most prominent line are the hydrogen Balmer series Hα ($\lambda = 6563\mathring{A}$), H$\beta$ ($\lambda = 4861\mathring{A}$), H$\gamma$ ($\lambda = 4340\mathring{A}$) and Ly$\alpha$ ($\lambda = 1216\mathring{A}$). The narrower width and the lack of variability of the narrow lines with respect to the broad lines led to the conclusion that they are emitted from distinct regions, the broad lines originating closer to the AGN. This led to the designation of the broad-line region

(BLR) and narrow-line region (NLR). The large Doppler widths of the BLR is a strong indication that they reside deep inside the gravitational potential well of the SMBH, as largely demonstrated by reverberation mapping studies. Thus, the BLR provides important insights into the central engine and a method to estimate the SMBH mass. The BLR has emission line width of $\sim$ 1000 - 10,000 km/s, with gas temperature of 10^4 - 10^5 and densities of $> 10^9$ cm^{-3}. In comparison the NLR had emission line width of $\sim$ hundreds of km/s, and densities of $\sim 10^3$ - 10^5 cm^{-3}. BLR mass is not more than few $M_\odot$ with sizes ranging from from $\sim$ 1 to 100s light-days while the mass of the NLR is of the order of millions of $M_\odot$ with size $>$ 100 pc. BLR is not spherically symmetric, it likely includes disk and wind components while NLR might be an extended AGN outflow and/or it is influenced by the AGN jet in radio-loud sources.

1.2.5 The Obscuring Torus

AGN models generally invoke an obscuring dusty structure with a toroidal geometry surrounding the central accretion disk, the so-called "obscuring torus". With respect to this component, Type 1 objects represent cases where the observer has a relatively unobstructed view of the inner AGN and BLR. Instead, Type 2 objects are observed through an obscuring structure, which largely absorb the optical-UV emission. The obscuring torus is expected to be located well at distances of $<$ 1pc. Dynamical studies tend to favor a clumpy structure, rather than a uniform toroid with a torus scale height-radius of H/R $\sim$ 1. The classification of AGN in Type 1 and 2 is based on the visibility of the nuclear region. For a clumpy torus the distinction between Type 1 and 2 is not only due to orientation but mostly to the probability of the observer having direct view of the AGN nucleus through the clouds. The origin of the torus is not clear yet. The clouds may be due to matter coming off the relatively cool, outer regions, of the accretion disk or they could be accreted from the ambient material within the host galaxy. Another scenario involves outflowing clouds from the disk embedded in a disk wind. The torus structure seems not to be the same for all sources, but at least dependent on the luminosity. In more luminous AGN, the distance of the torus is expected to be larger because dust will reach the sublimation temperature already at relatively large distances.

1.2.6 Mass Outflows and Winds

Mass outflows are found in a large fraction (if not all) of AGN. This is evident from blue-shifted absorption lines in the UV and X-ray spectra at different widths and velocities. Multiple outflowing components, characterized by distinct velocities relative to the systemic (cosmological) redshift of the AGN are often observed. About 50% of Seyfert 1 galaxies exhibit UV absorption from gas outflowing with velocities v $\leq$ 1,000 km/s (e.g., Crenshaw et al. 1999; Crenshaw and Kraemer 2012) and also X-ray absorption (George et al., 1998). The source of the outflowing material, relative to the central SMBH, may be near the inner nucleus (r $<$ 0.01 pc) or as remote as the galactic disk or halo (r $>$ 1 kpc). The acceleration (or launching) mechanisms for AGN disk winds are still discussed, but they are based on three main scenarios: (i) thermal, (ii) radiation pressure, and (iii) magneto-hydrodynamics (MHD), or, more likely, a combination of these. Strong Ultra Fast Outflows (UFO) are seen in AGNs, as blue shifted, highly ionized H and He-like iron K absorption features (e.g. King and Pounds 2003; Pounds et al. 2003; Reeves et al. 2009). Systematic studies of X-ray show that UFOs are detected in about a half of AGNs across a wide range of mass and mass accretion rate (Mizumoto et al., 2021); the outflowing gas is fast ($\nu_w \sim$ 0.05 - 0.3c, where c is the light velocity) and highly ionized, with large column density of $N_H \sim 10^{22}$ - 10^{24} cm^{-2} (e.g. Tombesi et al. 2011a). The kinetic power and momentum carried by this wind can affect the host galaxy evolution (e.g. King and Muldrew 2016), with the sub-pc scale UFO coupling to and powering kpc-scale cold outflows.

1.2.7 Relativistic Jets

AGN jets formation and their composition are still a matter of research. The conventional view involves magnetic fields running parallel to the disk axis, leading to the collimation of the outflow. Jets emerge from each face of the disk with a bipolar structure. Differential rotation of magnetic fields within the disk or black hole ergosphere is believed to launch the jet. The Blandford-Znajek mechanism (Blandford and Znajek, 1977) is a common theory for powering the jet by extracting rotational energy from the black hole. Relativistic material is launched through the reconfiguration of magnetic field lines. Numerical simulations in 3D relativistic MHD confirm the Blandford & Zna-

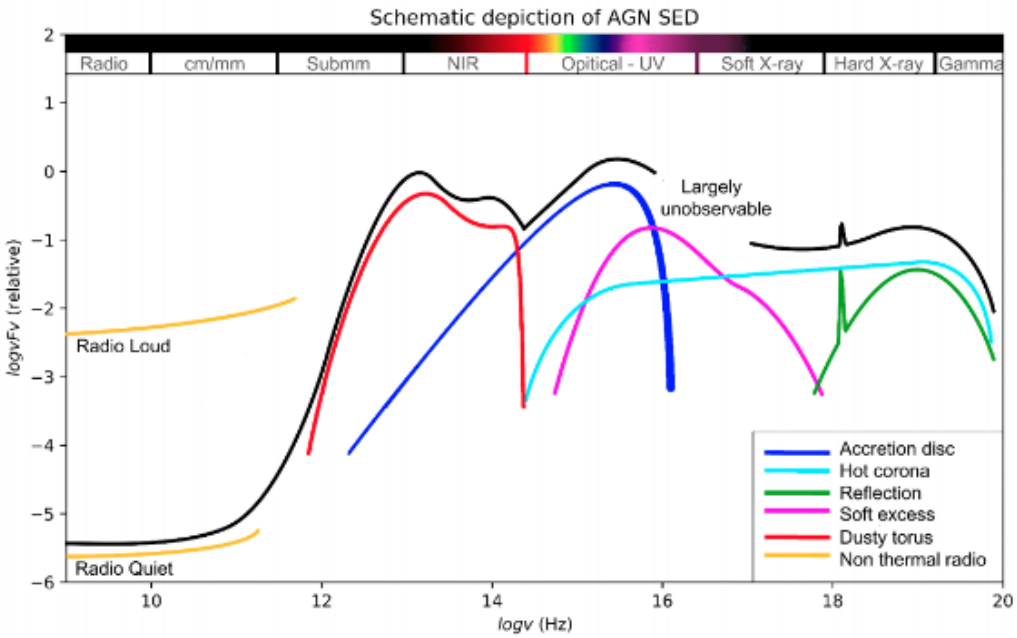

Figure 1.9: Schematic view of AGN SED. Courtesy of F. Shankar.

jek scenario, showing powerful jets from a spinning black hole. When the black hole is maximally spinning, around 140% of the energy available from accretion onto the black hole is channeled into the jet. These models emphasize the importance of magnetic field geometry in launching and powering the jets. Challenges remain in understanding jet acceleration and gamma-ray emission in AGNs, pointing towards the need for more detailed numerical simulations.

1.3 The AGN Spectral Energy Distribution

Since we can observe AGNs across the entire EM spectrum, we can discover and study them using multi-wavelength observations, allowing us to gain a comprehensive understanding of their physical properties and behaviors. In this section we discuss the main components of an AGN Spectral Energy Distribution (SED) (see figure 1.9), where each spectral component arises from and their characteristic properties.

1.3.1 UV Disk Emission

The largest contribution to the AGN bolometric luminosity is emitted as a strong, broad feature in the spectral energy distribution (SED) that peaks in the UV/optical

wavelength. This is produced by accretion processes very close to the central SMBH. This feature of the SED is knows as the Big Blue Bump (Sanders et al., 1989) and is likely due to the thermal emission arising from the geometrically thin, optically thick accretion disk (Shields 1978, Malkan and Sargent 1982, Ward et al. 1987). If we assume a standard Shakura-Sunayev α-disk model (Shakura and Sunyaev, 1973) where accretion disk emission is expected to have a thermal origin, we can write its luminosity as

$$dL_\nu = 2\pi r^2 B_\nu(\nu, T) dr \tag{1.3}$$

where each annulus at radius r has temperature T(r) and emits as a black body. Hence, the total luminosity at any wavelength can be calculated by the integration of dL_ν over the entire disk and is given as:

$$L_\nu(\nu) = \frac{4\pi h\nu^3}{c^2} \int_{r_{in}}^{r_{out}} \frac{r}{e^{\frac{h\nu}{k_B T}} - 1} dr \tag{1.4}$$

In the standard α disk model (see section 1.2.2) T $\propto$ r$^{-3/4}$, we get:

$$L_\nu(\nu) = \nu^{1/3} \int_{x(r_{in})}^{x(r_{out})} \frac{x^{5/3}}{e^x - 1} dx \tag{1.5}$$

by changing two variables in the integral from r to 1/T and by putting $x = \frac{h\nu}{k_b T}$. So for this portion of the spectrum we can see a slope $\propto 1/3$ (see figure 1.9; blue line and Figure 1.10).

1.3.2 X-ray Coronal Emission

AGNs emit primary X-rays from a hot corona near the SMBH. The corona scatters UV and optical photons from the accretion disk, creating hard X-rays. These X-rays from the corona can be reflected off the AD, producing a "Compton hump" and iron Kα line. An obscuring torus surrounding the central engine can also absorb and reprocess X-rays. The typical AGN X-ray spectrum can be modeled as a power law extending from 2 keV to 200 keV, with a cut-off observed for high energies and an excess emission ("soft excess") for energies lower than 2 keV. Another deviation from the power law is seen between 10 - 100 keV as a hump peaking at approximately 30 keV. A typical

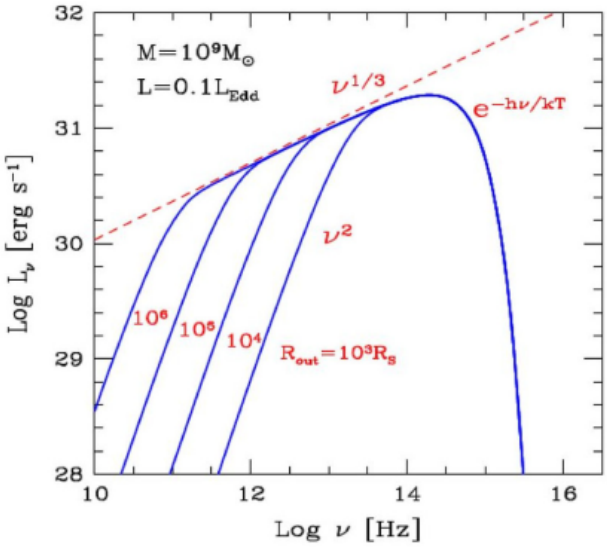

Figure 1.10: Spectral energy distribution for an α-disk emission model with a black hole mass of 10^9 $M_\odot$ and a bolometric luminosity equal to 10% of the Eddington luminosity. The central portion of the spectrum has a spectral slope $\propto 1/3$. A greater R_{out} value implies that we are considering colder (outer) regions of the disk therefore the black body emission will have a lower temperature component. The spectral slopes of both tails are the approximated black body spectral slope in the high and low energy regime (Ghisellini, 2013).

AGN X-ray spectrum is shown in Figure 1.16. The X-ray continuum can be affected by reprocessing through photoelectric absorption and Compton reflection from nearby material, such as the outer accretion disk or the inner edge of the obscuring torus. An important signature of reflection processes is the Fe Kα fluorescence emission line at 6.4 keV which gives us insight into the kinematics and gravitational field near the BH. Additional absorption components seen in the X-ray spectra of an AGN include warm absorber and ultra-fast outflows. We discuss the AGN X-ray emission components in more details in section 1.4.

The relation between the X-ray and optical-UV emission as a dependence between the logarithm of the monochromatic luminosity at 2500 $\mathring{A}$, and the α_{OX} parameter, defined as the slope of a power law connecting the monochromatic luminosity at 2 keV and L_{2500}: α_{OX} = -0.384 $\times$ log [$L_{2keV}/L_{2500\mathring{A}}$]. The α_{OX}-$L_{2500\mathring{A}}$ relation is the by-product of the non-linear correlation between L_{2keV} and $L_{2500\mathring{A}}$ given as: (log L_{2keV} = γlog $L_{2500\mathring{A}}$+β) with a slope γ of 0.5 - 0.7 found in both optically and X-ray selected AGN samples (see Lusso and Risaliti (2016) and references therein, Figure 1.11).

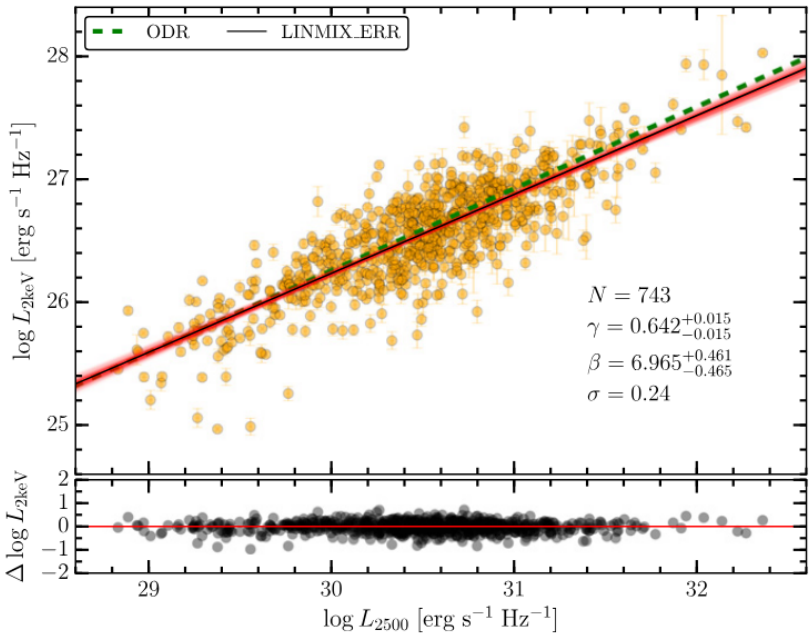

Figure 1.11: Rest-frame monochromatic luminosities L_{2keV} vs $L_{2500\mathring{A}}$ for the X-ray detected (orange circles) quasar samples in (Lusso and Risaliti, 2016). The dashed line and thin solid line shows regression for the samples. The red thin lines show 400 different realization of the L_{2keV}-$L_{2500\mathring{A}}$ relation from regression algorithm. The inserted values show the regression results for the dispersion, slope, and intercept (with their uncertainties).

An important parameter to study AGNs is the X-ray luminosity and the bolometric correction to derive the AGN bolometric luminosity. This is which is defined as the ratio between the bolometric luminosity and the luminosity in a given spectral band, that is, $K_{band} = L_{BOL}/L_{band}$. Duras et al. (2020) converted the $K_X(L_{BOL})$ into a relation in which the bolometric correction depends on the X-ray luminosity and fit this relation using the following equation:

$$K_X(L_X) = a\left[1 + \left(\frac{log\frac{L_X}{(L_\odot)}}{b}\right)^c\right] \tag{1.6}$$

where a, b and c are constant terms, K_X is the X-ray bolometric correction, L_X is the X-ray luminosity and $L_\odot$ is the solar luminosity. Figure 1.12 shows the best-fit relations for type 1 and type 2 AGN as a black continuous line (see Duras et al. (2020) and references therein).

1.3.3 IR Emission from Dusty Torus

Approximately 30% of the AGN bolometric output, comes from the IR band. The UV/optical AD radiation heats up the dust in the torus causing it to radiate in the IR band. The IR spectrum has a minimum at ~ 1 μm and a bump peaking at $\sim 20\mu$m with a steep powerlaw decline at $\sim 100\mu$m. The IR components can be roughly assumed to be comprised of (i) Thermal radiation from the dust in the compact region called the "dusty torus", (ii) Thermal dust continuum associated with star formation processes in the host galaxy, (iii) Additional lines due to molecular, atomic and ionic species in the AGN or host galaxy. The distance of the torus is expected to be luminosity dependent, implying that for higher luminosity the dust will reach the sublimation temperature even at larger radii. The dust sublimation radius can be estimated as:

$$r = 1.3 \times L_{UV46}^{0.5} T_{1500}^{-2.8} pc \tag{1.7}$$

where L_{UV46} is the UV luminosity in 10^{46} erg/s and T_{1500} is the temperature in 1500 K. This dust is composed of a mixture of silicates and graphite grains. Here we do not assume to have an ideal black body. The emission from the central engine is absorbed

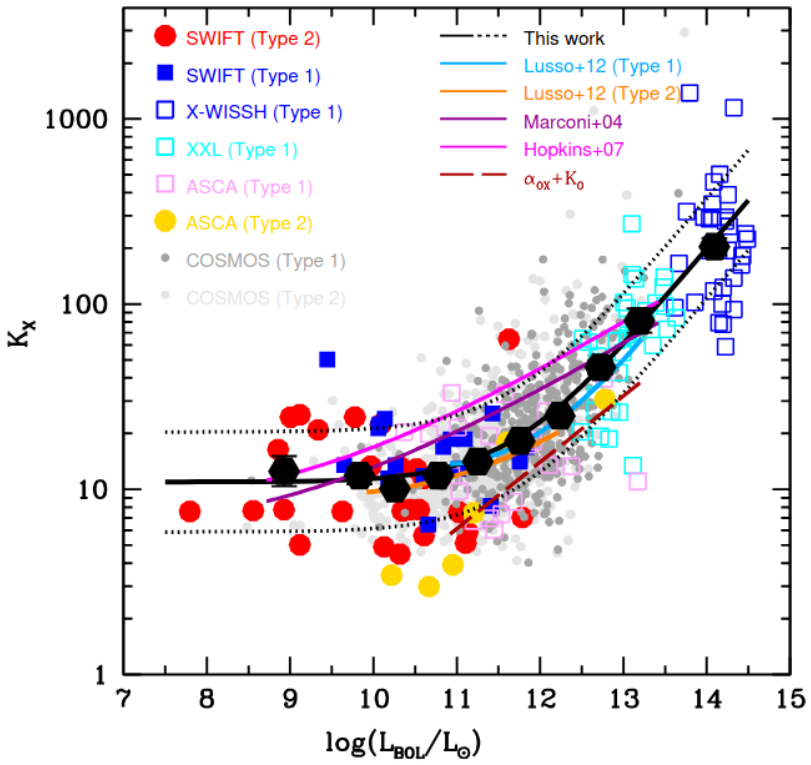

Figure 1.12: General hard X-ray bolometric correction in the 2 - 10 keV band as a function of the bolometric correction for type 1 and type 2 AGN. Black filled triangles and open circles show the average values for type 1 and type 2 sources respectively. Black hexagons are the average bolometric correction values, in bins of bolometric luminosity. The black solid line is our best-fit solution; the brown solid line is the analytical prediction obtained by assuming the relation between the X-ray luminosity and the optical luminosity by (Lusso and Risaliti, 2016).

and re-emitted in the outer regions of the torus which has high optical depth τ_ν as a function of frequency. If we assume an isothermal emitting matter, we can write the emitted luminosity as (Polletta et al. 2006, Soldi et al. 2008):

$$L_\nu = 4\pi A_{dust} B_\nu(T)(1 - e^{-\tau_\nu}) \tag{1.8}$$

where A_{dust} is the projected surface area that the observer sees but this doesn't necessarily have to be the torus. $B_\nu(T)$ is the Plank function of a black body of temperature T. We can approximate the frequency dependent optical depth by a power-law in the form: $\tau_\nu = \left(\frac{\nu}{\nu_0}\right)^\beta$ where $\nu_0 = \nu(\tau = 1)$ is the frequency at which the dust becomes optically thin and β is the dust emissivity index with typical values of 1.5 - 2 (Boselli et al., 2012).

1.3.4 Radio Emission

The dominant emission process in the radio band is synchrotron emission. This is the radiation emitted by relativistic charged particles when they are subject to an acceleration perpendicular to their velocity. In the simplest scenario we assume an uniformly distributed optically thin population of electrons with a power law energy distribution ($n(E) \propto E^{-p}$) in a magnetic field B with constant intensity and direction. The emission can then be parametrized as $S_\nu \propto \nu^{-\alpha}$ where in this simple case the spectral index of the radio spectrum is $\alpha = (p-1)/2$. Radio observations allows identification of compact and extended radio components. The compact component is called the radio core. This is unresolved at less than arcsec scales and it is thought to be coincident with a position close to the SMBH where the gas is optically thin. The extended emission is produced by jets and radio lobes. These structures are due to extremely energetic and highly collimated outflowing plasma launched from the inner accretion disk regions. These jets can extend up to 1 Mpc scales and often retain a very high degree of collimation. Jets are formed when magnetic field threads through the accreting matter roughly parallel to the disk axis. The twisting of these magnetic fields through their interaction with ionized gas leads to collimation of the outflow along the direction of the BH rotation axis. Thus under specific circumstance a jet will emerge

from each face of the accretion disk with a bipolar structure.

1.3.5 Gamma Ray Emission

Gamma rays in AGNs primarily originate from relativistic jets emitted by the SMBHs, where charged particles are accelerated to near-light speeds. If the jets point towards the observer, relativistic Doppler-boosting makes the jet emission appear much brighter and have more variability than in the co-moving frame. These AGNs are beamed and are characterized by non-thermal spectra and polarization. This non-thermal emission can be modeled by a power-law distribution of charged particles in a magnetic field which is the source of synchrotron emission. Additionally, inverse Compton up-scattering of seed photons by a population of relativistic particles. This power-law shape photon spectrum extends from radio to optical domain. Then through inverse Compton or synchrotron-self Compton (Maraschi et al. 1992; Bloom and Marscher 1996) or external Compton processes, these sources will have a secondary hump in their SED which typically peaks in the X-ray to gamma-ray band. Figure 1.13 show the two-hump "camel back" shape with the two bumps being synchrotron and inverse Compton spectra respectively.

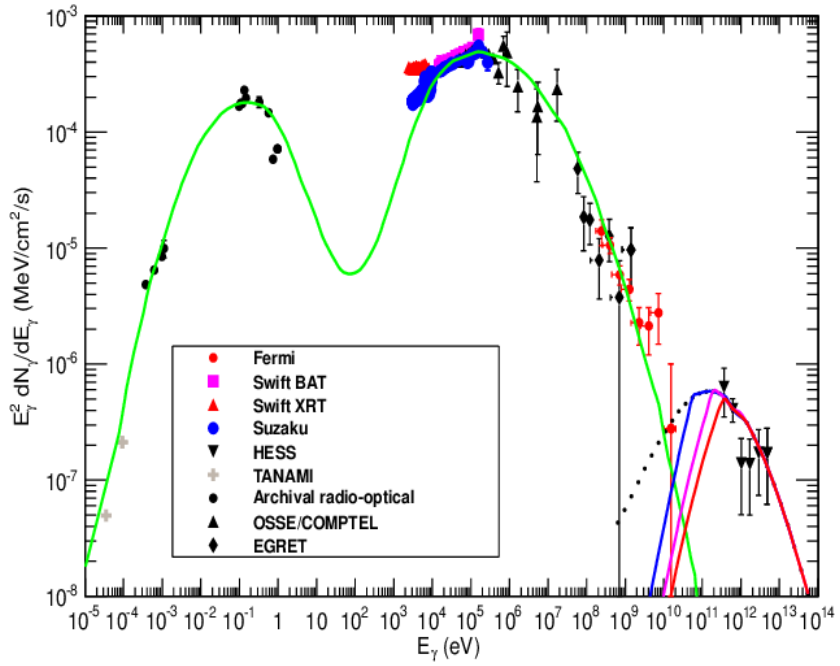

Figure 1.13: Broadband EM spectrum of the Radio Galaxy Centaurus A from radio up to γ rays. Colored symbol points are observations (with different sources marked in the figure), and the curves are model fits: The green curve is synchrotron + SSC fit from Abdo et al. (2010)

1.4 The X-ray Emission of AGNs

X-rays give us instantaneous information about the innermost accreting regions of a BH. The X-ray emission from AGNs is thought to be originating in a compact region known as the ***corona*** which lies above the accretion disk of an AGN. The broad-band X-ray emission can be modelled as a power law between 2 - 200 keV. The X-ray emission is thought to be produced through the process of inverse Compton scattering, where optical/UV photons from the AD are up-scattered by an optically thin, quasi-relativistic electrons population (typical temperature kT of the order of 1 - 100 keV, Fabian et al. 2017) in a corona ("hot corona") and is shown in Figure 1.16. Each upscattered photon has a final energy equal to:

$$E_f = e^{\gamma} E_i \tag{1.9}$$

$$\gamma = < \Delta\epsilon/\epsilon > \times < N > = \frac{4kT}{m_e c^2} max(\tau, \tau^2) \tag{1.10}$$

where m_e is the electron mass and γ is called Comptonization parameter which is the average fractional energy gain of a photon per scattering times the mean number N of expected scatterings. The resulting inverse Compton spectrum has a ***high energy cut-off*** ($\approx$ 128 keV, Malizia et al. 2014) due to temperature limitations of the disk and corona. Figure 1.14 shows the typical spectrum of an unabsorbed AGN with the high energy cutoff marked in the figure. Applying coronal models to observations is currently limited by our lack of knowledge in the mechanism for heating the electrons and the geometry of the hot corona. There are different models involving different corona geometries and energy input that are still being discussed. Figure 1.15 shows different accretion disk geometries.

The ***photon index***, Γ, (see Equation 1.11), characterizes the power law model, with typical values in AGN spectra ranging from 1.7 to 2.1 (Nandra and Pounds 1994, Piconcelli et al. 2005, Mainieri et al. 2007, Marchesi et al. 2016). The photon index can indicate accretion rate of the AGN as parameterized by the Eddington ratio, λ_{Edd}, that is, the mass-normalized bolometric luminosity (Shemmer et al., 2008). The photon number density is given as a function of energy (E) as follows:

$$n(E) \propto E^{-\Gamma} \tag{1.11}$$

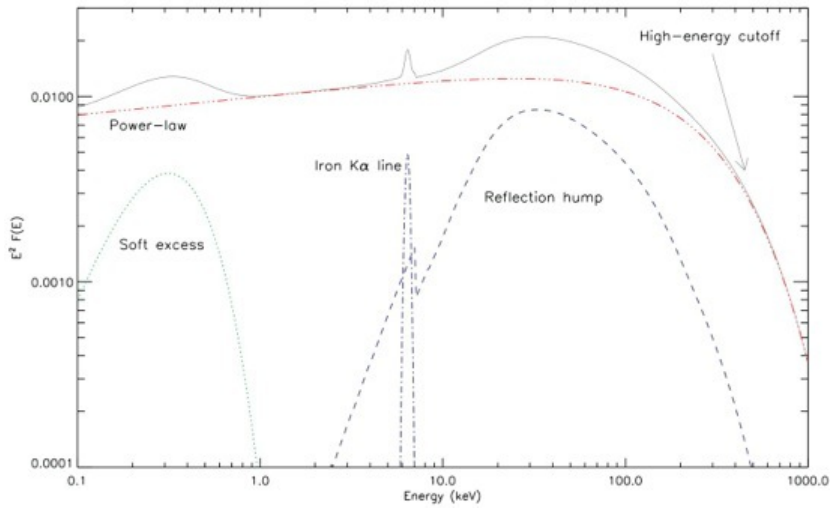

Figure 1.14: The typical 0.1 - 1000 keV spectrum of an unabsorbed AGN. Ricci et al. 2011, PhD thesis.

where spectral index, $\alpha_\nu = 1 - \Gamma$

The X-ray continuum can be affected by reprocessing through photoelectric absorption and Compton reflection from nearby material, such as the outer AD or the inner edge of the obscuring torus. Ghisellini et al. (1994) proposed that fraction of photons scattered towards the disk are reflected back to the hot corona, causing the observed hard X-ray bump. Some photons undergo photoelectric absorption followed by fluorescence line emission, while others are completely absorbed. The energy boundaries of the hard X-ray hump are determined by the cross section of photoelectric absorption. The cross section of the photoelectric absorption is inversely proportional to the photon energy ($\sigma \propto E^{-7/2}$) therefore those with energies lower than 10 keV are more likely to be absorbed than reflected hence the ***Compton hump*** decline around that energy (see Figure 1.16); for photons with energies higher than 100 keV the disk gas becomes optically thin and so they are scattered in deeper layers losing energy and eventually are absorbed.

The reflection spectrum of an AGN shows several emission lines. When hard X-ray photons interact with the cold gas around the SMBH, a number of possible interactions can occur: Compton scattering by free or bound electrons, photoelectric absorption followed by fluorescent metal line emission, or photoelectric absorption followed by Auger de-excitation. A given incident photon can either be destroyed by Auger de-

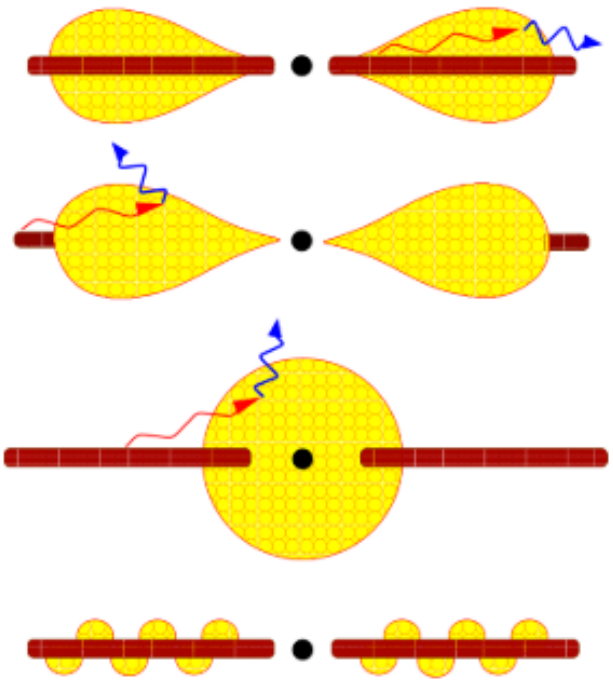

Figure 1.15: Possible geometries for an accretion disk (red) and comptonizing corona (yellow). The top figure is referred to as "slab" geometry; however it tends to predict spectra softer than observed. The remaining three show "photon starved geometries" wherein the corona is less effectively cooled by soft photons from the disk. The middle two geometries are referred as "sphere+disk" geometries, while the bottom as "patchy corona" model (Reynolds and Nowak, 2003).

excitation, scattered out of the cold gas region, or reprocessed into a fluorescent line photon which escapes the slab.

The ***fluorescent iron line*** is produced when one of the 2 K-shell (i.e. n = 1) electrons of an iron atom (or ion) is ejected following photoelectric absorption of an X-ray. The threshold for the absorption by neutral iron is 7.1 keV. Following the photoelectric event, the resulting excited state can decay in one of two ways. An L-shell (n = 2) electron can then drop into the K-shell releasing 6.4 keV of energy either as an emission line photon (34 per cent probability) or an Auger electron (66 per cent probability). This second case is equivalent to the photon produced by the n = 2 $\rightarrow$ n = 1 transition being internally absorbed by another electron which is then ejected from the ion. The study of Fe Kα profiles (seen at 6.4 keV, see Figure 1.16) in AGN can help us study general relativistic effects and probe the immediate environment of a black hole because they are thought to arise from X-ray irradiation of the inner accretion disk

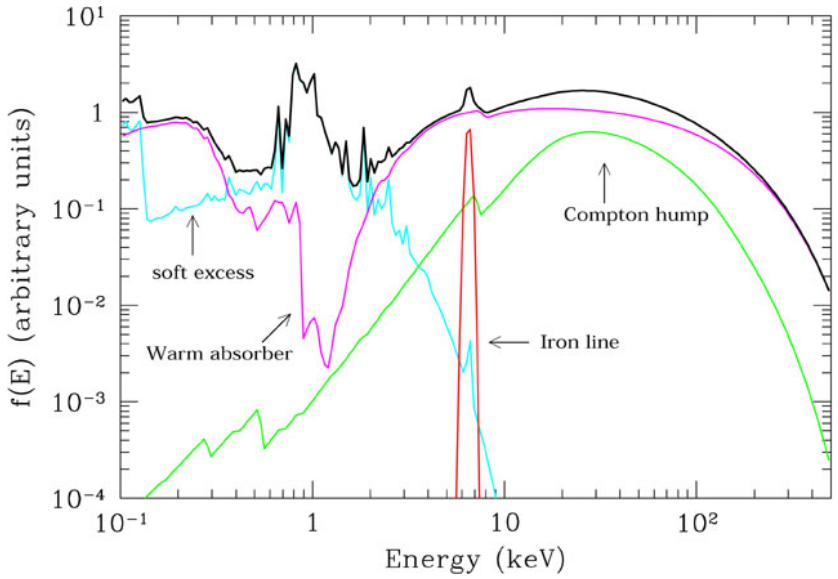

Figure 1.16: Average total spectrum (thick black line) and main components (thin grey lines) in the X-ray spectrum of a type I AGN. The main primary continuum component is a power law with an high energy cut-off at E $\sim$ 100 - 300 keV, absorbed at soft energies by warm gas with $N_H \sim 10^{21}$ - 10^{23} cm^{-2}.We also see the iron K α emission line at 6.4 keV along with a "soft excess" is shown. (Risaliti and Elvis, 2004)

orbiting the BH. These line profiles can be used to explore the central regions of AGN in detail. An important feature of this line is the Iwasawa-Taniguchi effect. Iwasawa and Taniguchi (1993) suggested an X-ray Baldwin effect in AGN, whereby the equivalent width (EW) of the Fe Kα line decreased with increasing luminosity (see Figure 1.17).

It is possible to detect many soft X-ray emission lines in Seyfert 2 galaxies, which are rarely detected in Seyfert1s. Hydrogen-like and helium-like lines are detected from Fe, Ne, Si, S, Ar and Mg and these cannot be explained only by the presence of starburst emission (Turner et al., 1997). Figure 1.18 shows the results of a Monte Carlo calculation which includes all of the above processes (Reynolds 1996[1]; based on similar calculations by George and Fabian 1991).

In the low energy tail ($\approx$ 1 keV) of AGN X-ray spectra, an additional component called the ***soft excess*** is observed (see Figure 1.16). The origin of this component is still uncertain, but possible explanations include additional comptonization ("warm" corona with a temperature in the range $\approx$ 0.1 - 1 keV), ionized reflection from the disk, or complex/ionized absorption. Recent studies suggest that the "warm" corona may be the most realistic explanation for the soft excess in both low and high luminosity AGN

[1]Reynolds C. S., 1996, Ph.D thesis, Univ. of Cambridge.

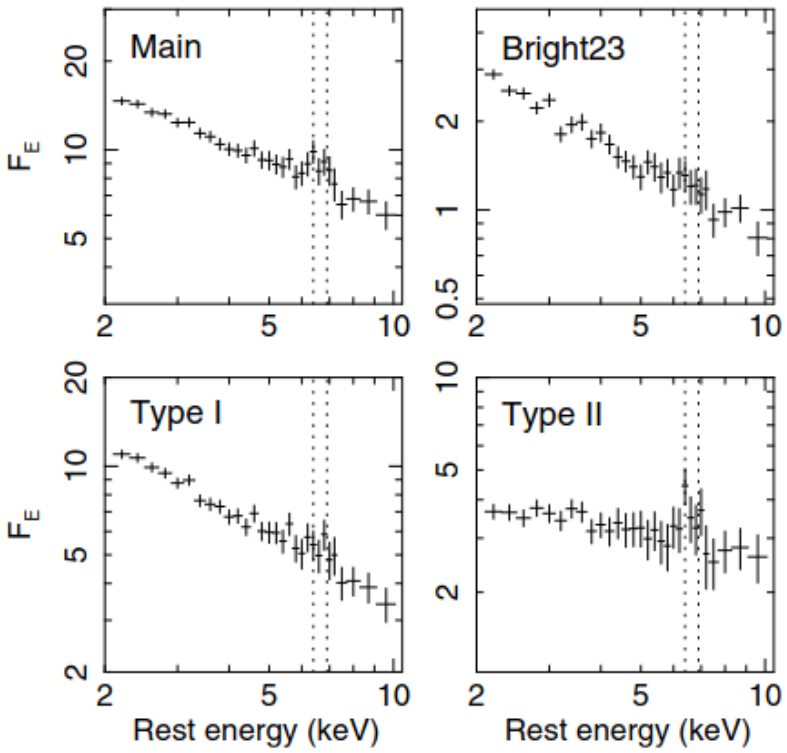

Figure 1.17: An excess emission is seen at $\sim$ 6.6 keV which appears to consist of two unresolved emission line components at 6.4 $\pm$ 0.2 keV and 6.8 $\pm$ 0.2 keV rather than a single broad line. The EW of the lines are 0.04 $\pm$ 0.02 keV and 0.05 $\pm$ 0.02 keV, respectively. The width of this 6.4 keV line agrees with what is expected from the Iwasawa-Taniguchi effect. See (Iwasawa et al., 2012) and references therein.

(Krawczynski et al., 2022).

The partially ionized, optically thin gas along our line of sight to the central X-ray source can also have a substantial effect on the soft X-ray spectrum. This partially ionized material is known as the warm absorber. Observational signatures of warm absorbers are discussed on a theoretical basis by Netzer (1993). Warm absorbers are characterized by hydrogen column densities of $\sim 10^{20}$ - 10^{22} cm^{-2}, ionization parameter ranging from -1 $<$ log(ξ) [ergs cm^{-1}] $<$ 4, slow to moderate line of sight velocities (v $\sim$ 100 - 1000 km s^{-1} and variability on time scales of months to years. They are detected in more than 50% of AGN. The inferred electron temperature of the X-ray absorbing gas is T $< 10^5$K which is lower than typical collisionally ionized thermal plasma at similar level of ionization (Fukumura et al., 2022).

An extreme type of absorbers are Ultra Fast Outflows (UFOs) which are identified through the detection of highly blue-shifted and ionized iron absorption lines (Tombesi

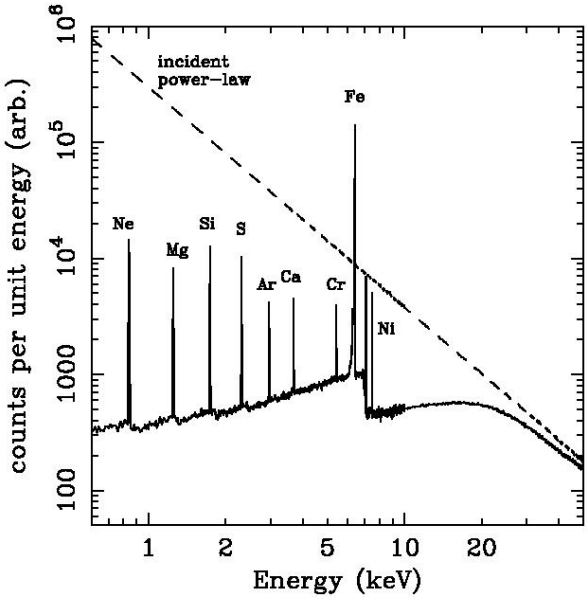

Figure 1.18: X-ray reflection from an illuminated slab. Dashed line shows the incident continuum and solid line shows the reflected spectrum (integrated over all angles). Monte Carlo simulation from Reynolds (1996).

et al. 2010, Tombesi et al. 2011b) (see figure 1.19). These indicate gas outflows with mildly relativistic velocities upto $\sim$ 50 % of the speed of light. These are characterized by column densities of $\leq 10^{24}$ cm^{-2}, ionization parameter ranging from $4 < \log(\xi)$ [ergs cm^{-1}] < 6, relativistic line of sight velocities and variability on a time scale of days (Fukumura et al. 2022, Kraemer et al. 2018). UFOs are produced well within the sphere of influence of BHs and when AGN luminosity increases or the ionization parameter increases, the UFO velocity increases. These UFOs might be the main mechanism responsible for AGN feedback (see Section 1.6).

1.5 SMBH Mass Estimates

A SMBH can be described by three fundamental quantities, i.e, mass, charge and angular momentum. The mass estimation of a SMBH is of paramount importance in the study of SMBHs. The knowledge of the SMBH mass is important to understand BH mass distribution at different epochs, to study the evolution and phenomenology of QSOs, accretion physics and the dynamics of the BLR. We can estimate the mass of a SMBH in various ways but a few commonly used methods are described below:

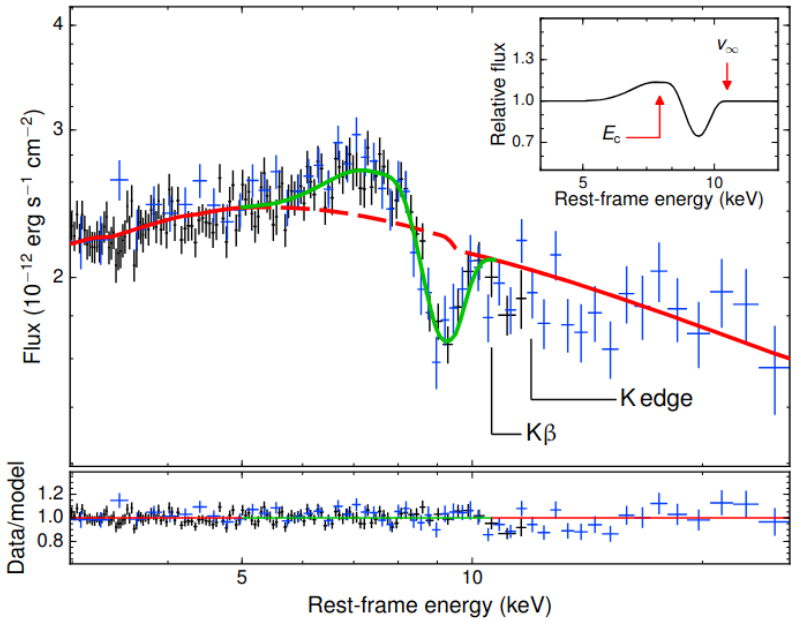

Figure 1.19: X-ray spectrum of PDS-456 with the typical P-Cygni profile in Fe XXVI Kα. The green curve represent the fit obtained using a model of P-Cygni profile due to a spherically symmetric outflow and the red curve indicate the continuum emission (Nardini et al., 2015).

1.5.1 Dynamical Mass Estimates

High-resolution imaging and spectroscopy of the central engines of nearby galaxies reveal large mass concentrations, especially in bulge-dominated systems, likely due to SMBHs. These SMBHs, like Sgr A* in our Galaxy, are typically nonactive or have very low accretion rates but they must have had an active history resulting in significant increase in their masses. Observing Keplerian stellar orbits around SMBHs, such as in our Galactic center, provides the most accurate way to estimate their mass. Given the high angular resolution necessary to resolve the motion of each star, this method can reliably be applied only to our Galactic center Sgr A* with a SMBH of $4.31 \pm 0.36 \times 10^6\ M_\odot$ (Gillessen et al., 2009). The stars in the innermost arcsecond (S-stars) of our Galaxy are used as test particles to probe the gravitational potential in which they move. The motion of these stars, unlike gas, is solely determined by gravitational forces. Therefore by fitting each star orbital parameters it is possible to determine the SMBH gravitation field. Figure 1.20 show stellar orbits at the Galactic center of Sag A* confirming the presence of a BH.

There is high interstellar extinction of ~ 30 magnitudes in the optical towards the

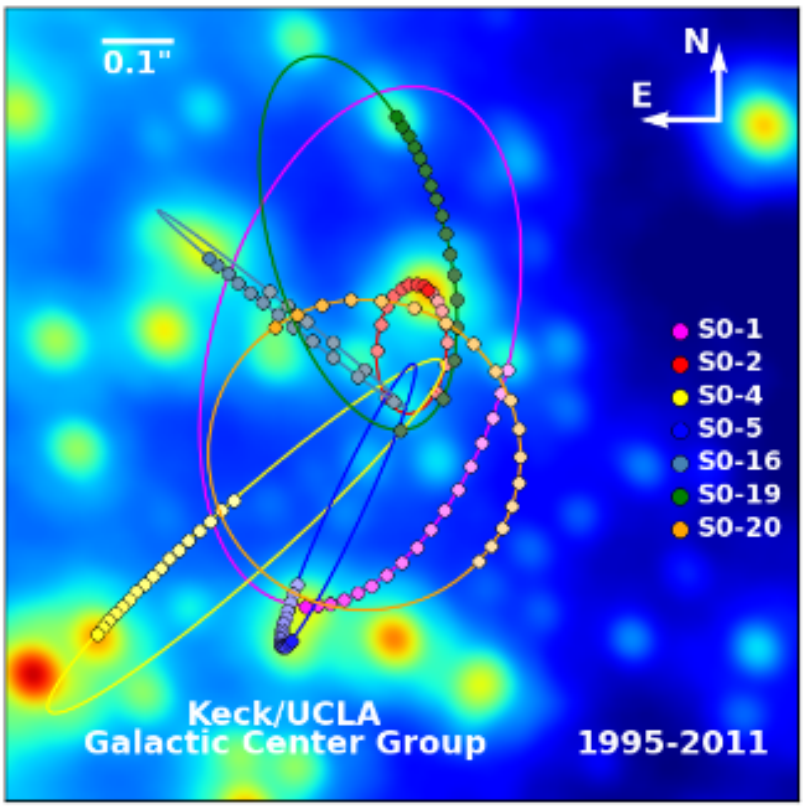

Figure 1.20: Stellar orbits at the Galactic center proving the existence of a black hole. The star S0-2 dominates our knowledge about the central potential, since with an orbital period of 16 years it has been tracked throughout a whole orbit. The other stars have longer orbital periods and therefore only a fraction of their orbits is covered by observations. Taken from Morris et al. (2012).

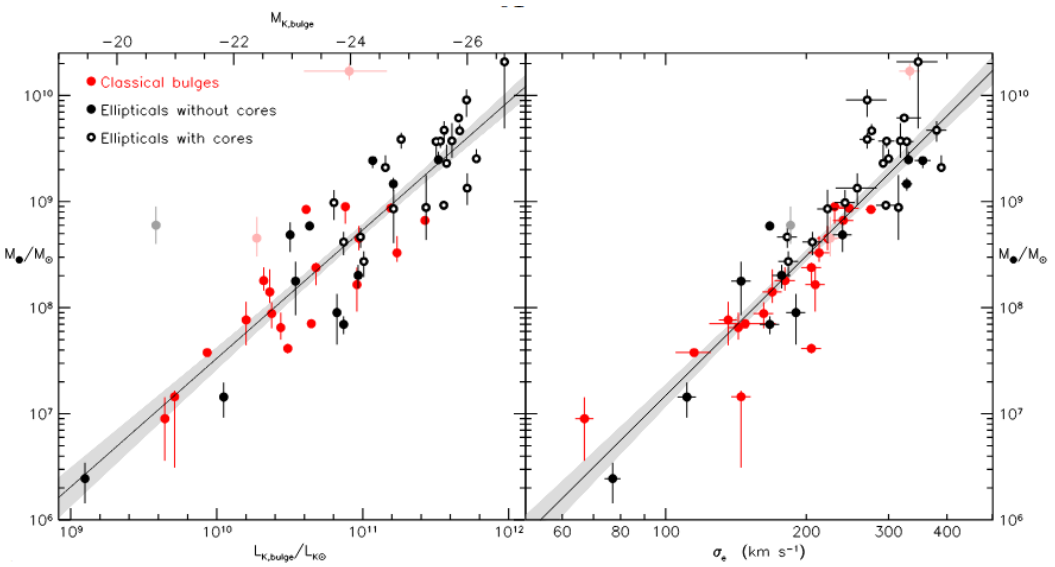

Figure 1.21: This figure from (Kormendy and Ho, 2013) suggests that the M_* -σ relation becomes vertical at $\sigma > 270$ km/s.

Galactic center. So the measurements have to be performed in the NIR where the extinction decreases to ~ 3 magnitudes. For more than a decade, the most important tool for this research was the Hubble Space Telescope (HST). Except for our Galactic center, for which the center can be resolved, it is still possible to measure a SMBH mass studying the kinematics of the bulge stellar populations through their absorption line spectra. In elliptical and bulge-dominated galaxies, the radius of this sphere is

$$r_{BH} = \frac{GM_{BH}}{\sigma_*^2} \sim 10.7 \times \frac{M_{BH}}{10^8 M_\odot} \left[\frac{\sigma_*}{200 kms^{-1}}\right]^{-2} pc \tag{1.12}$$

where σ_* is the stellar velocity dispersion in the bulge. For large elliptical galaxies $\sigma_* \sim 200$ km s^{-1}. Measurement of masses of SMBHs using this method has revealed useful correlations between M_{BH} and other properties of bulge dominated galaxies. One of the most important correlation between SMBH mass and stellar velocity dispersion in the bulge σ_*. This is called the M-σ_* relation given as:

$$log\frac{M_{BH}}{M_\odot} = \alpha_{BH} + b_{BH} log\frac{\sigma_*}{200 kms^{-1}} \tag{1.13}$$

Kormendy and Ho (2013) estimated $\alpha_{BH} \sim 8.29$ and $b_{BH} \sim 3.75$ based on a sample of 85 galaxies (see Figure 1.21). But this method has limited applicability. A higher angular resolution is required to observe a galaxy's SMBH sphere of influence.

Also, attempting to estimate and AGN SMBH mass is observationally challenging with this method because the overwhelming AGN continuum dilutes the stellar absorption features.

1.5.2 Reverberation Mapping

Reverberation mapping (RM), a technique that swaps spatial resolution for time resolution and allows BH mass measurements and the determination of the size scales of emitting regions associated with X-rays, the UV/optical continuum, BLR, and dusty torus. Bahcall et al. (1972) recognized that time variability in the intensity of emission from a central source would affect the observed intensity of emission from photoionized gas in active galaxies and some novae. Based on this, Blandford and McKee (1982) developed a framework for inverting the observed time-dependence of broad emission-line variations to map out the structure of the BLR. The principle of the RM is based on measuring the time delay between flux variation in the ionizing sources and the surrounding BLR (Figure 1.22 shows lag between different energy band on a range of timescales). A single compact central source emits irradiating flux. Changes in the irradiating flux will drive changes in the reprocessed emission. So light curves from the two regions should be strongly correlated. But the light from the reprocessed emission has to travel an extra distance to get to the observer, the variations in the reprocessed emission will arrive later than the variations in the ionizing flux. The light travel timescale is far smaller than the timescale with which the BLR substantially changes and the relation between the observed reprocessed and ionizing fluxes is assumed to be linear.

The lag, τ ,depends on the exact geometry of the system, but the average lag will be of the order R/c, where R is the typical radius of the emitting region.

The delay is measured usually using the cross-correlation function. This is defined as:

$$CCF(\tau) = \int_{-\infty}^{\infty} L(t)C(t-\tau)\,dt \tag{1.14}$$

where L(t) is the emission line flux while C(t - τ) is the continuum light curve. In

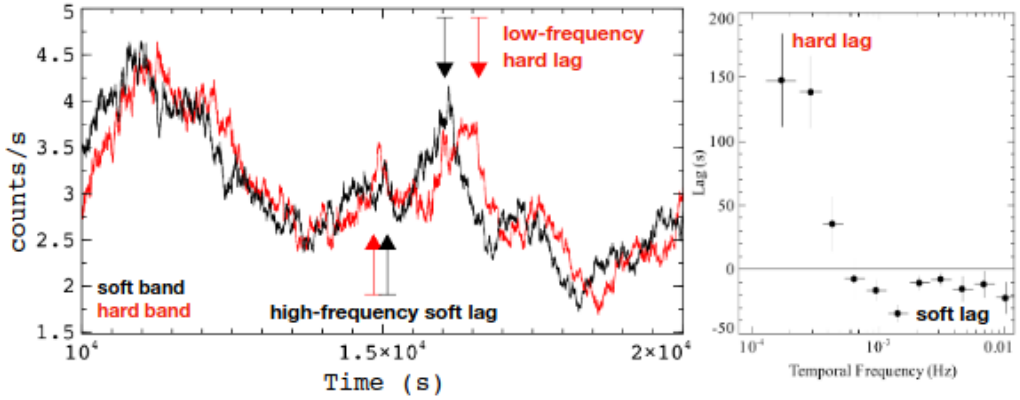

Figure 1.22: Left: A portion of a simulated (noiseless) hard band (1 - 4 keV; red) and soft band (0.3 – 1 keV; black) light curve based on the properties of 1H0707-495, displaying variability on a range of timescales. On long timescales (low temporal frequencies), the hard band lag the soft, but on short timescales (high temporal frequencies), the soft band lags the soft. This demonstrates the benefit of studying X-ray reverberation (soft lags) using frequency-resolved timing analysis. Right: The observed lag-frequency spectrum of Seyfert galaxy 1H0707-495 (Zoghbi et al., 2010), showing the hard lags (positive lags) at low frequencies and the soft lags (negative lags) at high frequencies.Taken from Cackett et al. (2021).

practice the light curves are shifted with respect to each other in the time domain and for each time lag a degree of correlation is measured. With non-continuous light curves (e.g. optical light curves) a linear interpolation is often used (Peterson et al., 2004). So in this technique we have to measure flux variation of the AGN over different wavelengths and for long period of time but this is still a practical and powerful tool to study the BLRs whose spatial extent is too small to be resolved by current instrumentation. As of now, there are about hundred AGNs and QSOs ($z < 0.3$) with average time delay measurements (Kaspi et al. 2000, Woo et al. 2010) although only a small fraction of them have sufficiently accurate velocity resolved delay map (Grier et al., 2013).

Assuming that the BLR is virialized and that the motion of the emitting clouds is dominated by the gravitational field of the BH, the mass of the BH can be determined by the following

$$M_{RM} = \frac{v_{vir}^2 R}{G} = f\frac{W^2 R}{G} \tag{1.15}$$

where v_{vir} is the cloud viral velocity and R is the BLR size and G is the universal Gravitational constant, W is the width of the broad line which serves as an indicator

of the virial velocity, assuming that the broad line is Doppler broadened primarily by the virial motion of the emitting gas. The line width definition commonly used is the FWHM. The structure and geometry of the BLR remain uncertain, affecting the relationship between virial and line of sight velocity. A virial coefficient (or geometrical factor), f is introduced to account for this uncertainty. But even with f, the complexity of the system is only approximated due to factors like BLR structure and viewing angle influencing the line profile. It is also an approximation to describe the BLR with a single radius R. Nevertheless the above equation is still used universally.

Now, the value of f is empirically determined by requiring that the derived RM masses are consistent with those predicted from the BH mass-bulge stellar velocity dispersion relation of local inactive galaxies. This f value is then averaged for the subset of the RM AGNs with bulge stellar velocity dispersion measurements. The uncertainty in f and its assumptions remain one of the major uncertainties in RM mass determinations which is typically of $\sim$ 0.4 - 0.5 dex (Peterson et al., 2013).

Using RM observations a tight correlation between the measured BLR size and the adjacent optical continuum luminosity L_{opt}($R \propto L^{\alpha}$) over $\sim$ 4 orders of magnitude in luminosity has been found. This is known as the BLR size-luminosity relation (R-L) (e.g. Kaspi et al. 2000, Woo et al. 2010). A slope of $\alpha = 0.5$ can be predicted if the BLR size is set by dust sublimation (Netzer and Laor, 1993). Carefully accounting for the host galaxy starlight contamination (Woo et al., 2010) reports also an $\alpha \sim 0.5$. The intrinsic scatter of the R-L relation is estimated to be $\sim$ 0.11 dex (Peterson et al., 2010). The latest version of the R-L relation based on Hβ RM measurements is (Woo et al., 2010):

$$log\frac{R}{light \quad days} = -21.3 + 0.519 \times log\frac{\lambda L_{\lambda}(5100\mathring{A})}{erg \quad s^{-1}} \tag{1.16}$$

1.5.3 Single Epoch Virial Mass Estimates

The radius-luminosity relation has also been used to develop the so called virial mass estimator. In this method, the BLR size is measured from the measured quasar luminosity using the R-L relation and the width of the broad emission line. These are then combined to give an estimate of the BH mass using calibration coefficients determined

from the sample of AGNs with RM mass estimates. These take the form:

$$log\frac{M_{SE}}{M_{\odot}} = a + b \quad log\frac{L}{10^{44} erg \quad s^{-1}} + c \quad log\frac{FWHM}{km \quad s^{-1}} \tag{1.17}$$

where L is the monochromatic QSO continuum luminosity and FWHM is the width for the specific line. The coefficients a,b and c are calibrated against RM AGNs. Based on the general similarity of quasars SEDs, different luminosities have been used, including continuum luminosities in X-ray, restframe UV and optical, as well as different lines, in various version of these SE (e.g., Vestergaard 2002; McLure and Dunlop 2004; Vestergaard and Peterson 2006; Zhang et al. 2010; Vestergaard and Osmer 2009; Shen et al. 2011). The uncertainty of the SE virial estimators can be inferred from the residual in the calibrations against the RM masses, and is estimated to be on the order of $\sim$0.5 dex.

Hβ, Hα, Mg II, and C IV are commonly used in virial calibrations depending on the redshifts. Hβ is widely used in reverberation mapping. Mg II (Reichert et al., 1994) is used for intermediate redshifts, with some cases showing time-lag measurements consistent with Hβ (McLure and Dunlop, 2004). At high redshifts, C IV is typically adopted and its SE is calibrated with Hβ RM AGNs. Previous studies show strong correlations between Hα, Hβ, and Mg II widths (Shen et al., 2008), but C IV width poorly correlates with Hβ (Shen and Liu, 2012). Different kinematics of C IV compared to Hβ may be due to varied origins of high and low ionization emission lines. These findings suggest a different kinematics of the C IV with respect to the Hβ one, likely due to the different origin of the high ionization emission lines with respect to the low-ionization lines, (see Vietri et al. 2018). Coatman et al. (2017) analyzed a sample of high luminosity quasars having both C IV and Hα coverage and find that in the presence of large blueshift of the C IV the BH mass derived from the C IV emission line tends to be a factor of five larger than those measured by the Hα line and even larger in case of highly blueshifted CIV emission lines in luminous QSOs.

1.6 AGN Formation, Co-Evolution and Feedback Mechanism

AGNs are among the most energetic phenomena in the universe and their formation requires an initial BH onto which accretion-driven growth can occur. The nature of how and when these initial seeds were formed remains an important open question. A primary challenge for any model of seed BH formation is posed by the existence of luminous quasars with $M_{BH} > 10^9 M_\odot$ at $z > 6$, when the Universe was 1 Gyr old. There are currently three main candidate mechanisms for seed formation: (1) remnants of massive population III stars (2) direct collapse of primordial gas clouds, and (3) runaway collisions in dense stellar clusters. We discuss this is details in Chapter 2.

Discussions on BH growth often focus on the impact of energy released through accretion on surrounding gas. In principle, a growing BH releases plenty of energy to impact its surroundings. Therefore, given a sufficiently strong coupling between the radiative or mechanical output of the BH and the surrounding gas, the AGN should be able to disrupt its environment and potentially regulate its own growth and star formation in the host galaxy. This is known as the feedback mechanism and occurs through physical processes such as winds and jets can couple energy from the BH to the surrounding gas. Winds comprises of wide-angle, sub-relativistic outflows that tend to be driven by the radiative output of the AGN. Jets (often referred to as radio-mode) are relativistic outflows with narrow opening angles that are launched directly from the accretion flow itself. The radiatively-dominated AGN that drive winds are expected to be relatively high-Eddington ratio systems, while jets are most commonly produced (except for the highest-power sources) by lower-Eddington ratio accretion flows (see Section 1.2.5 and 1.2.6). High$-z$ QSOs in SDSS exhibit blueshifted broad C IV emission peaks, indicating outflows of approximately 1000 km/s (Richards et al., 2011). QSOs with larger blueshifts have higher C IV equivalent widths and weaker X-ray emissions. Broad absorption line quasars, accounting for 20 - 40% of quasars, also show this trend with X-ray emissions. Evidence suggests that all quasars may host energetic winds (Ganguly and Brotherton, 2008). The maximum blueshift in BAL quasars is associated with weaker X-ray emissions. Both these and the results on C

IV blueshifts can be understood in terms of radiation driving of the QSO wind; with a weaker X-ray continuum, the gas close to the BH is less highly ionized and so more easily driven by the UV continuum radiation from the QSOs.

Understanding the formation and growth of AGNs is essential for cosmic evolution. Questions remain about seed BH origins and the role of feedback mechanisms in regulating BH growth and star formation. High-redshift QSOs challenge early black hole formation models, while outflows and jets in AGNs highlight complex interactions with their environments. In the following chapter we discuss in details, BH growth and the multi-wavelength properties of QSOs at the Epoch of Reionization.

Chapter 2

Quasars at the Epoch of Reionization

After the recombination epoch at $z > 1100$, the universe became mostly neutral until the first generation of stars and QSOs reionized the intergalactic medium (IGM) and ended the cosmic "dark ages" (Holt and Smith, 1999). Cosmological models predict reionization between $z \approx 6$ - 20. In the beginning of this century, the first QSO at $z > 5.6$ was discovered meaning that this quasar was seen within the first gigayear of the formation of the universe (Fan et al., 2000). The advent of increasingly sensitive multi-band wide area surveys (optical/infrared), allowing efficient searches of luminous QSOs at z > 5.5 - 6 (e.g. in the SDSS, PanSTARRS1 and UKIDSS fields; Jiang et al. 2016, Bañados et al. 2016, Venemans et al. 2007), allowed the study QSOs in the first billion years of cosmic evolution ($z \sim 6$), witnessing the final phases of the Hydrogen Reionization Epoch (called the Epoch of Reionization, EoR, Fan et al. 2006).

The study of QSOs within the first gigayear of the universe helps to constrain BH formation models. Furthermore, they are fundamental to probe of the final phases of EoR. As SMBHs play a crucial role in galaxy formation processes, QSOs provide crucial probes of galaxy evolution and cosmology across cosmic history. Their nuclear emission is crucial for understanding BH accretion and AGN activity. QSOs also offer insights into early large-scale structure growth, study of IGM properties, cosmic reionization history, baryon distribution, and circum-galactic medium's role in galaxy formation from tens of kpc to Mpc scales. Observations of $z \sim 6$ QSOs tell us that SMBHs

with masses up to a few billion solar masses already existed in the Universe within one billion years after the Big Bang implying that BH must have occurred at least either via early massive BH seeds or rapid BH accretion. Early luminous QSOs are sites of intensive galaxy-scale star formation and the assembly of early massive galaxies and the detection of strong IGM absorption in quasar spectra, especially the emergence of complete Gunn–Peterson absorption troughs (Gunn and Peterson, 1965), shows a rapid transition of the ionization state of the IGM at $z \sim 5 - 6$, marking this epoch as the end of cosmic reionization.

Pre-JWST mass estimates for SMBHs powering high-z QSOs are based on the Mg II emission line in the NIR spectrum for a sizable number of sources ($\geq$ 40% - 50%). By fitting the continuum NIR spectra and the Mg II emission line, the M_{BH} and λ_{Edd} of a number of $z > 6$ QSOs have been derived (Wu et al. 2015, Farina et al. 2022). They show M_{BH} similar to those derived in lower-z QSOs matched in luminosity and high accretion rates roughly close to the Eddington limit. Figure 2.1 shows 83 such high-z QSOs. These measurements have improved our understanding of early universe SMBH and high-z QSO and also raised numerous questions about their nature, host and the environment.

Surveys of the highest-z QSOs pose three main challenges. Primarily, these QSOs are extremely rare objects in the Universe, making their discovery difficult. The final SDSS $z \sim 6$ QSO sample, covering over 11,000 sq. deg, only contains 52 QSOs (Jiang et al., 2016). Secondly high-z QSOs can be confused with other celestial objects like cool Galactic dwarf stars (M, L, T type) and compact early-type intermediate z galaxies because they have similar optical and NIR colors. To address this, various photometric selection techniques have been developed to improve efficiency and accuracy. Lastly, identifying candidate QSOs requires observations from large aperture telescopes.

Wang et al. (2017) utilized low-resolution long-slit NIR spectroscopy to enhance spectroscopic identification efficiency, capturing Lyman break features in QSO spectra and rejecting contaminants with shorter exposure compared to higher resolution spectra. Luminous type 1 QSOs are distinguished by their distinct SED, characterized by a blue power-law continuum and strong broad emission lines in the rest-frame UV and optical wave bands. At $z > 3$, the strong IGM neutral hydrogen (HI) absorption

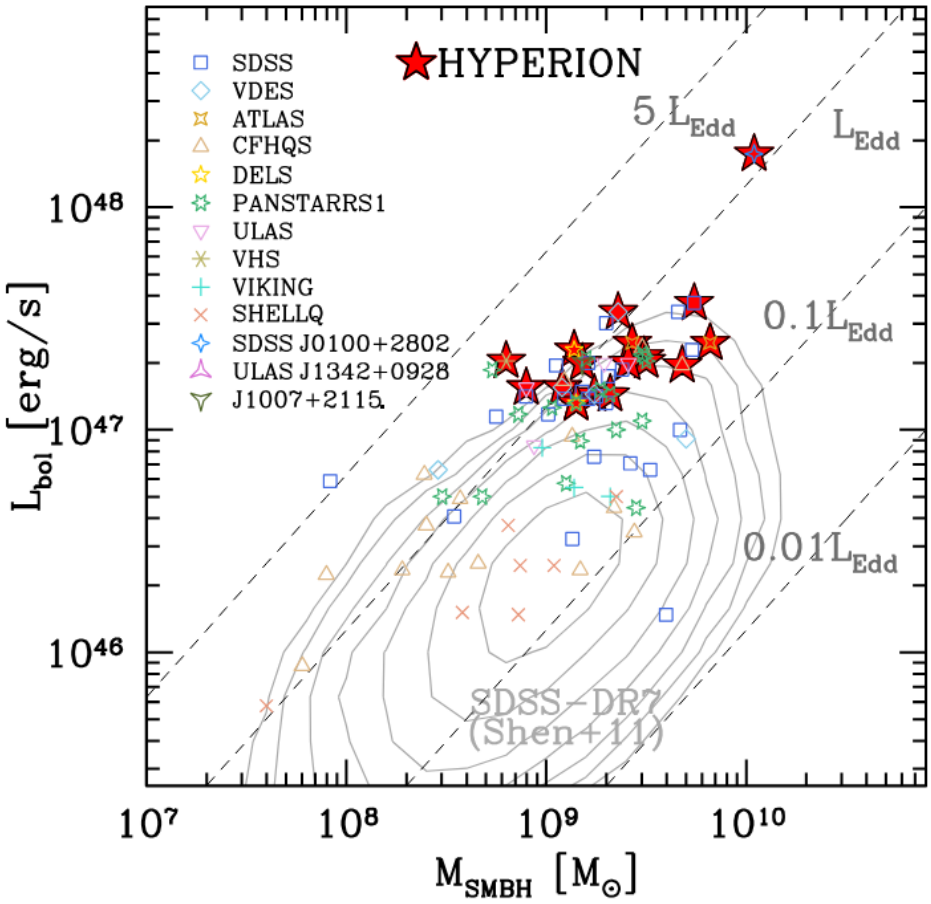

Figure 2.1: Distribution of the 83 $z > 6$ QSOs with available M_{SMBH} (based on single-epoch Mg II virial estimator) and L_{bol} from literature. Dashed lines report the location of sources emitting a fixed fractions of L_{Edd}. The contours report the location of the lower redshift (z = 0.7 - 1.9) SDSS-DR7 QSOs from (Shen et al., 2011) with Mg II-derived masses. (Zappacosta et al., 2023)

from Lyman series lines and Lyman continuum redshifts into the observed optical wavelength. So, high-z QSOs exhibit "dropout" characteristics due to strong Lyman breaks at observed wavelengths, with the Lyman dropout selection technique being employed since the discovery of the first $z > 4$ QSOs (Warren and Hewett, 1990). A more recent development is the inclusion of mid-IR (MIR) photometric surveys in the candidate selection (e.g. Wu et al. 2015). The long wavelength baseline from NIR to MIR, in particular using the WISE (Wright et al., 2010) data, allows more effective separation of high-z QSOs and MLT dwarfs by colors. QSO J0313–1806 at $z = 7.64$ (Wang et al., 2021) is currently the farthest luminous QSO observed with approximately 300 known QSOs at $z \geq 6$ (Fan et al., 2023).

Most high-z QSO are identified through color selection, where a series of "color cuts" are used to select objects meeting specific criteria in the flux/flux-error space. High-redshift surveys conducted using SDSS (Jiang et al., 2016), PanSTARRS1 (Bañados et al., 2016), and DESI Legacy Survey (Wang et al., 2019) commonly employ color cuts for their selection process due to its simplicity and high completeness. However, this method may lead to a higher contamination rate as all candidates that meet the cuts are selected without considering population density distributions or how candidate spectral energy distributions match QSO templates. For instance, the success rate for finding $z > 6.5$ QSOs is only 30% (Wang et al., 2019).

Multiple techniques have been developed to enhance color selection efficiency, particularly for identifying QSOs at high-z ($z > 6.5$), where they are scarce. Mortlock et al. (2012) introduced a Bayesian model comparison (BMC) algorithm, while Reed et al. (2017) utilized SED fitting for high-redshift QSO selection. Barnett et al. (2021) conducted a comprehensive study on various selection methods for $z > 6.5$ QSOs using VIKING survey data, highlighting BMC's effectiveness in identifying QSOs and rejecting contaminants. Wenzl et al. (2021) employed a random forest machine learning method for selecting $z > 5$ QSOs, while Nanni et al. (2022) proposed a probabilistic approach using Gaussian mixtures to model contaminant populations in color space.

Selecting high-z QSOs can be done using supervised machine learning, but with small training sets. The choice of algorithm in a survey must balance completeness and efficiency, as models relying on spectral energy distribution and contaminant popula-

tions may miss valuable objects with unique properties. For example, the discovery of J0100+2802, the most luminous QSO at $z > 5$, was initially considered a low priority due to its red color. Using less restrictive methods may lead to groundbreaking discoveries, as seen with the DESI survey, aiming to double the number of known QSOs at $z > 5$. Established selection methods include variability, astrometry, and X-ray detections, with color cuts often used for high-z candidates. Future surveys like 4MOST (Merloni et al., 2019) and e-ROSITA (Wolf et al., 2021) will further enhance our understanding of high-redshift QSOs.

2.1 The Growth of SMBHs

The mere existence of SMBH with M_{BH} as large as $10^9 M_\odot$ or more at EoR poses serious challenges to theoretical models designed to explain how these systems formed in less than 1 Gyr (e.g. Volonteri 2010; Johnson and Haardt 2016). In the standard growth scenario, the luminosity of an accreting BH can be expressed as:

$$L_{bol} = c^2 \frac{\eta}{1-\eta} \dot{M}_{BH} \tag{2.1}$$

where $\dot{M}_{BH}$ = (1 - η)$\dot{m}$, $\dot{M}_{BH}$ is the BH growth rate and $\dot{m}$ is the mass accretion rate. If we assume that the BH is shining at L_{Edd}, it grows in mass exponentially as:

$$M_{BH}(t) = M_{BH}(0) \times exp\left(\frac{1-\eta}{\eta} \frac{t}{t_{Edd}} \times t_{duty} \times \lambda_{Edd}\right) \tag{2.2}$$

where $M_{BH}(0)$ is the mass of the BH at the formation epoch z = 20 - 30, t_{Edd} = 0.45 Gyr is the Eddington time, $\eta \sim 0.1$ and t_{duty} is the duty cycle that refers to the fraction of the time that an AGN is actively accreting. When $\lambda_{Edd} = 1$, the Eddington limit is reached (see Chapter 1). This formula describes a simplified scenario but can be used to estimate the minimum mass of the first BHs, $M_{BH}(0)$, called "BH seeds", that existed in the very early universe (at the formation epoch, z_0 = 20 - 30 when the universe was $\sim$ 200 Myrs old) at a given time z_0 such that they grow into SMBHs of a given mass $M_{BH}(t)$ observed at the redshift corresponding to time t. Various hypotheses have been suggested to explain how BH seeds can form and grow to the masses observed at z = 6.

a) Pop III star remnants - The remnants of Population III stars, known as light seeds, are formed when these metal-free objects of mass hundreds of $M_{\odot}$ collapse at $z > 20$ (Abel et al., 2002). These light seeds have masses less than or equal to 300 $M_{\odot}$ (Volonteri, 2010). However, uncertainties exist regarding the final mass of these stars, and specific assumptions are needed to explain the presence of SMBH remnants. According to Equation 2.2, these primordial stellar mass BHs may only grow to $<$ 10^8 - 10^9 $M_{\odot}$ SMBH at $z \sim 6$ by accreting gas almost continuously at the Eddington limit. In order to grow the measured masses at $z > 6$, i.e. 10^9 - 10^{10} $M_{\odot}$, super-Eddington accretion must be invoked (Volonteri et al., 2021). These super-Eddington growth usually proceed via short and recurring episodes of accretion because of the lack of continuous gas supply through out the growth process. Hence, a fundamental requirement in these scenarios is the uninterrupted availability of approximately 10^9 $M_{\odot}$ cold gas supply throughout there growth history (Johnson and Bromm, 2007).

b) Runaway collisions in star clusters - Stellar collisions in compact star clusters could potentially result in the formation of "intermediate" mass seed BHs with masses ranging from approximately 10^3 - 10^4 $M_{\odot}$. In this case, Eddington-limited continuous accretion is needed to form SMBHs with 10^9 - 10^{10} $M_{\odot}$ at $z \sim 6$. Super-Eddington accretion may not be required here.

c) Direct collapse BH - In the early universe, the collapse of cooling halos exposed to intense Lyman-Werner flux (i.e. a radiation field with photons of energy, h$\nu \sim$ 11.2 - 13.6 eV) may cause the formation of a black hole through a relativistic instability. This occurs when the gas contracts without cooling and fragments into stars due to the absence of main coolants (metals and molecular hydrogen). The result is the formation of a "heavy " seed BH with a mass of around 10^5 – 10^6 $M_{\odot}$. This scenario can potentially allow the growth of 10^9 - 10^{10} $M_{\odot}$ with less sustained feeding, i.e , sub-Eddington growth.

Figure 2.2 shows the seed BH masses necessary to growh the observed $z \sim 6$ - 7.5 SMBHs powering luminous QSOs. The BH growth of different $z > 6$ QSOs is highlighted with continuous lines of different colors. The BH growth is modeled as $M_{BH} = M_{BH,seed} \times \exp[t/0.05\ Gyr]$, i.e, assuming Equation 2.2 and that the BHs accrete continuously

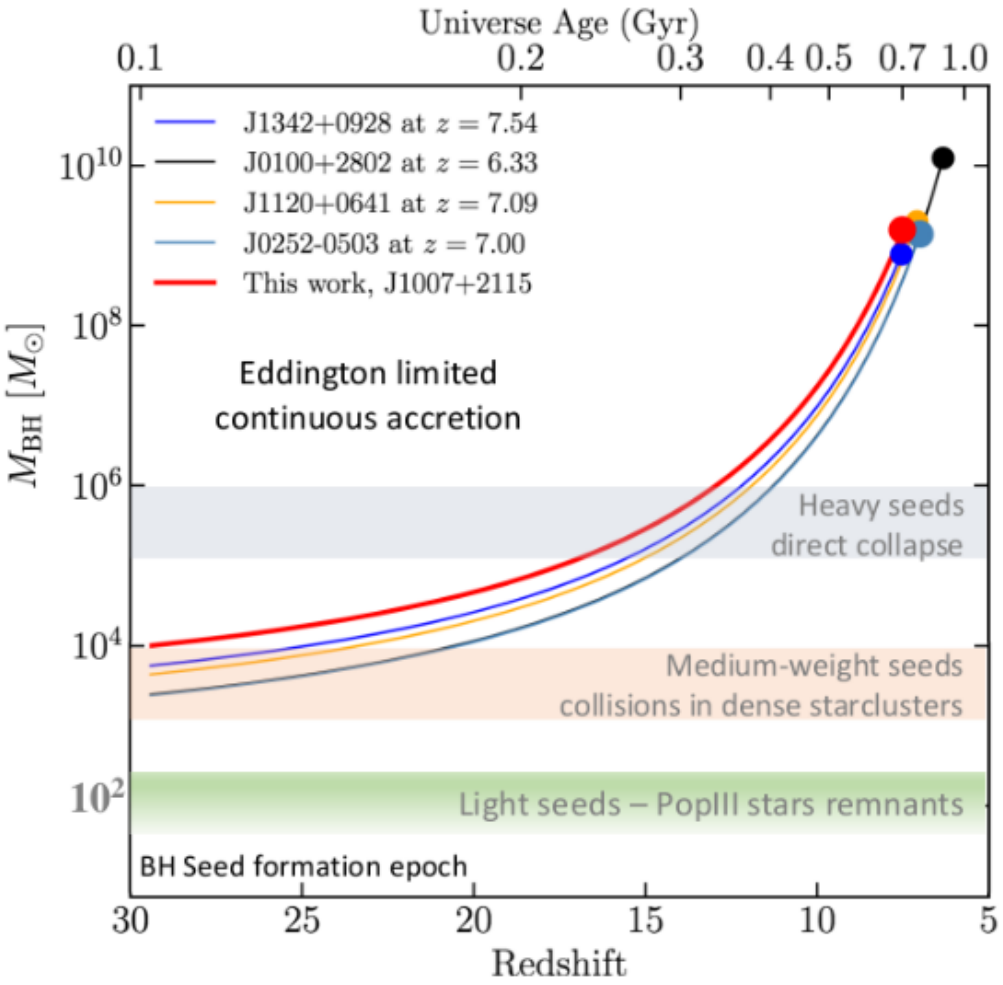

Figure 2.2: Seed mass required to grow, via a super Eddington continuous accretion given by Equation 2.2, the masses of the SMBH powering some of the most challenging QSOs. Mass intervals for different type of seed BHs (adapted from Yang et al. (2020)).

at the Eddington limit with $\eta = 0.1$ since seed formation ($z_0 = 30$). The shaded regions represent the mass ranges of the different BH seed scenarios.

2.2 Multiwavelength Properties of $z > 6$ QSO

A notable property of the highest-z QSOs is that they exhibit "normal" basic emission properties, i.e., very similar to those exhibited by similarly luminous highly accreting QSOs at $z < 6$. High-z galaxies have intrinsic blue SEDs that are dominated by young stellar populations. Metallicity, or chemical abundance, in their ISM has also been shown to be lower than in low-z galaxies (Stark, 2016). However, the overall SEDs and the chemical abundance in quasar BLRs do not evolve significantly with redshift, although quasar density decreases drastically at high redshift. The analysis of rest-frame UV composite spectra of an high-z QSO sample (Shen et al., 2019) is remarkably similar to lower-z QSOs (Berk et al., 2001) that are matched in luminosity. In particular the UV Fe II strength relative to the Mg II line is almost identical to that of lower-z QSOs (e.g. Yang et al. 2021, Figure 2.3) shows a lack of spectral evolution in QSO rest-frame UV spectra, especially in the emission line properties, suggests an already metal-rich BLR environment at the EoR. The broad emission lines of C IV λ1549, C III] λ1909, and Mg II λ2798 also show comparable profiles with respect to lower-z sources.

The relative intensities of these lines do not exhibit significant evolution out to $z \sim 7$ (e.g. De Rosa et al. 2014). Such comparisons have to account for the tendency of highly-accreting QSOs to show blue-shifted UV broad lines. Mazzucchelli et al. (2017) and Meyer et al. (2019) report a significantly higher average C IV blueshift than low-z SDSS QSOs matched in luminosity (with velocities upto 3000 km/s, i.e. a factor of ~ 2.5 times larger than at lower-z) suggesting the presence of strong wind/outflows components in the BLR of the highest-z QSOs. This evidence have been later downplayed by works analyzing larger QSO samples at $z > 6$ (Schindler et al. 2022, Yang et al. 2023).

Additionally, the analysis of broad emission lines indicates early nuclear chemical enrichment, up to super-solar metallicity (De Rosa et al. 2011, Mazzucchelli et al. 2017) comparable to similar luminosity low-z counterparts. Studies also show weak UV line emission for 10 - 20% of them; a factor of approximately 2 - 3 higher than reported at

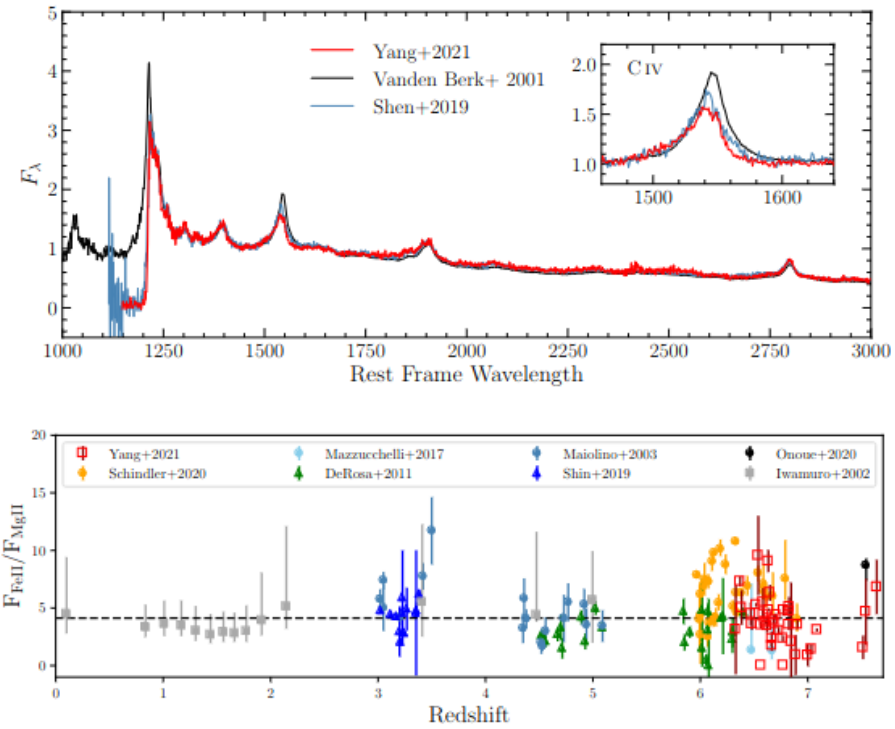

Figure 2.3: Upper panel: Quasar composite spectrum (red solid line) from (Yang et al., 2021) compared with the low-redshift ($z \leq 3$) composite from (Berk et al., 2001); black line) and the $z \sim 6$ quasar composite from (Shen et al., 2019); blue line). The average intrinsic spectrum of QSO does not exhibit significant redshift evolution. Lower panel: the evolution of the Fe/Mg emission line radio in QSOs as a function of redshift. The quasar BLR is highly enriched even at the highest redshift. Adapted from (Yang et al., 2021)

lower z (Bañados et al. 2016, Jiang et al. 2016). Recently Bischetti et al. (2022) reported a fraction of broad absorption line QSOs hosting fast nuclear winds to be $\sim$ 40 - 50% at$z > 6$. This is a factor > 2 larger than at lower$-z$ as reported by Bischetti et al. (2023). These findings imply that, on average, nuclear regions are more dynamically active and pervaded by QSO-driven winds at early times (Elvis 2000,Richards et al. 2006).

High-z QSOs are among the most luminous sources at (sub)millimeter wavelengths with a large amount ($\sim 10^7$ - 10^8 $M_\odot$) of warm dust as well as cold molecular gas ($\sim 10^9$ - 10^{10} $M_\odot$, Carilli and Walter 2013) in their host galaxy. [CII] line (158μm) observations reveal the presence of copious amounts of dust ($> 10^8 M_\odot$) and vigorous star formation rates (SFR, up to 1000 - 3000 $M_\odot$/yr), within the host galaxies (Maiolino et al. 2005, Wang et al. 2013, Venemans et al. 2020). This line is thought to be the dominant coolant of the ISM and is an important tool to understand the high-redshift universe as it is very luminous and connected to star formation.

The kinematics of [CII] and CO emission lines show organized motions in QSO hosts on a kiloparsec scale. Observations at $z \sim 4$ - 5 reveal massive star-forming galaxies within 50 kpc of the QSO hosts, suggesting mergers contribute to early supermassive black hole (SMBH) growth (Gallerani et al., 2012). ALMA observations provide detailed kinematic maps using the [CII] line (Wang et al. 2013, Tripodi et al. 2023). By analyzing the size and velocity width of the [CII] line, an estimate of the host galaxy's dynamical mass can be obtained. Comparison of SMBH and dynamical mass distributions at different redshifts indicates a deviation at $z \sim 6$, from the local relation (see Figure 2.4) showing lower mass host galaxies at the same M_{BH}. This suggests that the first generation of SMBH emerged through some sort of preferentially efficient BH fuelling mechanism. This hints at a unique efficient fueling mechanism for the first SMBH generation, although studies on $z > 5$ QSOs may be biased towards high M_{BH}/M_{dyn} ratios due to their luminosity (Izumi et al., 2019). M_{dyn} is the total ("dynamical") mass of the host galaxy estimated under the assumption of a rotating disk configuration with a given inclination angle and the size of the emitting region matching the observed atomic/molecular gas distribution.

X-rays give direct and instantaneous information about the innermost accreting

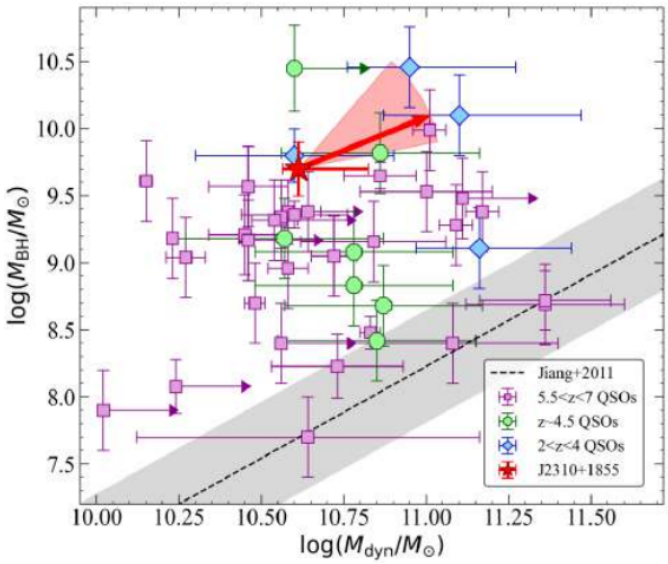

Figure 2.4: M_{BH} as a function of M_{dyn} for J2310=1855 (red), Bischetti et al. (2021) (blue) and luminous z $\sim$ 4 - 7 QSOs (green and violet) (Venemans et al. 2017; Trakhtenbrot et al. 2017; Feruglio et al. 2018; De Rosa et al. 2011; Kashikawa et al. 2014; Neeleman et al. 2021). the dashed line shows the local M_{BH} - M_{dyn} relation found by (Jiang et al., 2011). For J2310, the slope of the red arrow, with its uncertainty (shadowed red region), indicates how much the growth efficiency of the SMBH is slowing down with respect to the growth of the host galaxy (Tripodi et al., 2022).

regions of an AGN. Most $z > 6$ QSOs observed in X-rays have low-quality data leading to a poor knowledge of the QSO high energy nuclear properties. So most of our knowledge about these QSOs relies mainly on a combined joint spectral fit of high-z samples. Nanni et al. (2017) analyzed 29 quasars with average $z \sim 6.0$ with X-ray detection. They found a mean X-ray power-law photon index of $\Gamma \sim 1.9$, which is similar to that at low redshift. The optical-X-ray spectral slopes of the high-z also follow the relation established at low-z. Vito et al. (2019) carried out a similar analysis and found a slightly steeper X-ray power-law index, consistent with a generally higher Eddington ratio among SMBHs in these quasars at $z > 6$ (see Figure 2.5, top panel). Wang et al. (2021) extended the X-ray analysis to quasars at $z \sim 7$. They also found marginal evidence of a steepening of X-ray spectra with $\Gamma \sim 2.3$. Regarding the X-ray radiative output Vito et al. (2019) did not find evidence for a significant evolution of the relation between QSO UV and X-ray luminosity, as traced by the α_{OX} parameter. They found that the luminosities of $z > 6$ QSOs are consistent with α_{OX} vs $L_{2500\mathring{A}}$ relation, implying that the coronal emission becomes less important compared with disk emission at high

luminosity also at $z > 6$ (see Figure 2.5, bottom panel).

In particular the relative importance of the hot corona and the accretion disk radiative output is usually described with $\alpha_{OX} = 0.38 \times \log(L_{2keV}/L_{2500Å})$ which represents the slope of a nominal power-law connecting the rest frame UV and X-ray emission. This parameter is known to anti-correlate with the QSO UV luminosity (e.g. Just et al. 2007), i.e. the relative contribution of the X-ray corona emission to the L_{bol} represented by the optical-UV emission from the accretion disk decreases with increasing L_{bol}.

Wang et al. (2010) used CO emission to measure dynamical masses in 8 QSO hosts at $z \sim 6$ and found SMBHs that were 15 times more massive than expected from the local BH-bulge mass relation. This suggests BHs in high-z QSOs either had a head-start or grew faster than their host galaxies, indicating strong cosmic evolution (if the M - σ relation existed at $z \sim 6$). (Neeleman et al., 2021) conducted dynamic modeling of [C II] observations, finding a mean dynamical mass of $\sim 5 \times 10^{10}\ M_{\odot}$ for $z \sim 6$ QSOs with $\sim 10^{9}\ M_{\odot}$ BHs, one order of magnitude above the local relation (see Figure 2.6). This relationship could be strongly affected by potential biases from selection and by using gas tracer. Indeed, observations of low luminosity QSOs show a narrower [C II] line width (e.g.,Willott et al. 2017, Izumi et al. 2018), placing them close to the local relation.

2.3 The HYPERION Sample

The HYPERION sample of QSOs is defined by the selection of all the know $z > 6$ hyperluminous QSOs ($L_{bol} \geq 10^{47}$ erg s^{-1}) that required an initial seed BH of mass $>$ 1000 $M_{\odot}$ accreting via continuous exponential growth (see Equation 2.2) at the Eddington rate to form the measured SMBH mass. The selection was performed on the 46 unlensed radio-quiet hyperluminous $z > 6$ QSOs known with published SMBH masses at the end of 2020. Figure 2.7 shows the selection criterion of the HYPERION QSOs. The curves represent the BH time-dependent exponential mass growth – modeled as in Equation 2.2. With $t_{duty} = 1$, $\lambda = 1$ and $\eta = 0.1$ and assuming a seed formation redshift of 20 and where $M_{s,Edd}$ is $M_{BH}(0)$. These conditions give us the "titans" amongst QSOs which are powered by the SMBH that experienced the most extreme and fast

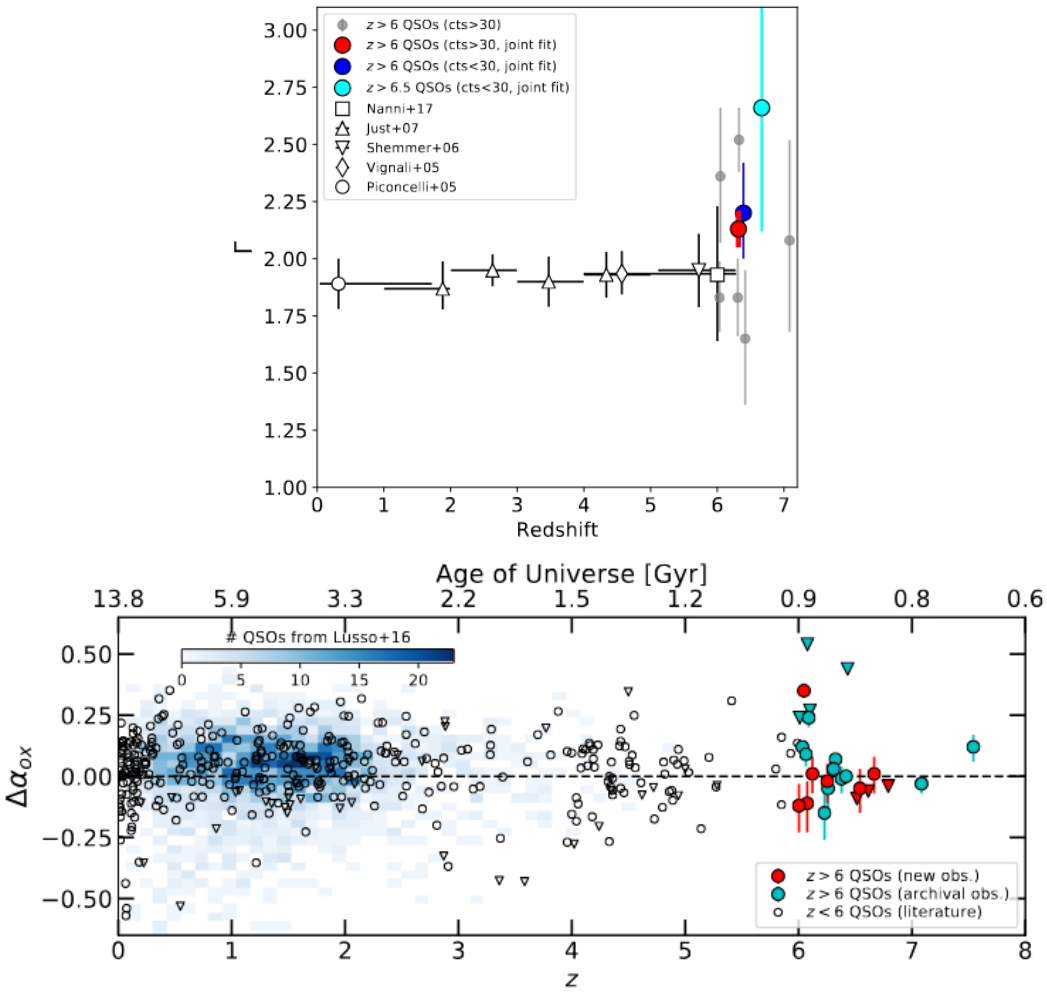

Figure 2.5: (Top) Photon index as function of redshift. Vito et al. (2019) reported the individual best-fitting values for sources with > 30 total net counts (gray symbols), the results derived from joint spectral analysis of QSOs with > 30, < 30 net counts, and of $z > 6.5$ QSOs (red, blue, and cyan circles, respectively, plotted at the median redshift of each subsample), and the average photon indices derived by Piconcelli et al. (2005), Vignali et al. (2005),Shemmer et al. (2006), Just et al. (2007), and Nanni et al. (2017) for optically selected luminous QSOs at different redshifts. Errors are at the 68% confidence level. (Bottom) $\Delta\alpha_{OX}$ vs. redshift for $z \geq 6$ QSOs. Vito et al. (2019) compared their results with a compilation of QSOs at lower redshifts (Shemmer et al. 2006, Just et al. 2007, Lusso and Risaliti 2016, Steffen et al. 2006). Downward-pointing triangles represent upper limits. The horizontal dashed line corresponds to $\Delta\alpha_{OX} = 0$.

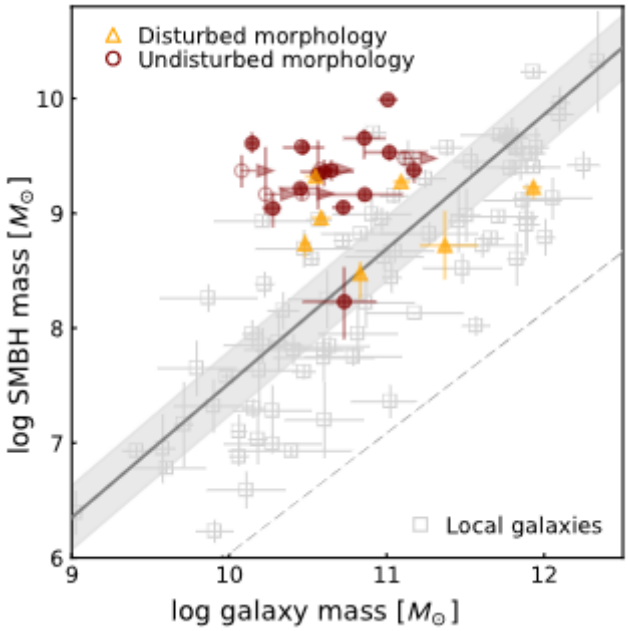

Figure 2.6: BH mass vs. host dynamical mass for $z \geq 6$ QSOs (figure from Neeleman et al. 2021). The gray points are local galaxies and the shaded region is the best-fit local relation (Kormendy and Ho, 2013). The $z \geq 6$ sample is divided by their [C II] morphology and it is generally above the local relation.

growth rate history over the first giga-year of the universe (Zappacosta et al., 2023). This selection identifies 18 of these sources through a reference curve, starting at $M_{s,Edd}$ = $1000 M_\odot$ at z_0 =20 , for the continuous Eddington-limited mass growth (see Figure 2.7, left panel). Under this assumption, the $M_{s,Edd}$ required by each SMBH to grow its mass has to be considered as the only proxy for the mass growth rate experienced by each SMBH and not necessarily as a physically meaningful quantity.

These QSOs were discovered through optical to mid IR selection and have extensive high quality spectroscopy and photometric data from rest frame UV to submm or mm bands. The HYPERION QSOs have redshift in the range $z \sim 6$ - 7.5 with a mean of z $\sim$ 6.7. Their average $\log(L_{bol}/\mathrm{erg\ s^{-1}}) \sim 47.3$ and mass range is 10^9 - 10^{10} $M_\odot$ leading to λ_{Edd} = 0.3 - 2.6 (see Figure 2.7, right panel).

The Mg II based single epoch virial mass and bolometric luminosity from 3000$\mathring{A}$ bolometric correction (Shen et al. 2019, Reed et al. 2019) were derived from near-infrared (UV rest-frame) observations carried out at Very Large Telescope (VLT), Magellan, Gemini, or Keck. The photometric data in the NIR and submm/mm bands were similarly available in different levels of quality (Tripodi et al. 2023, Feruglio et al.

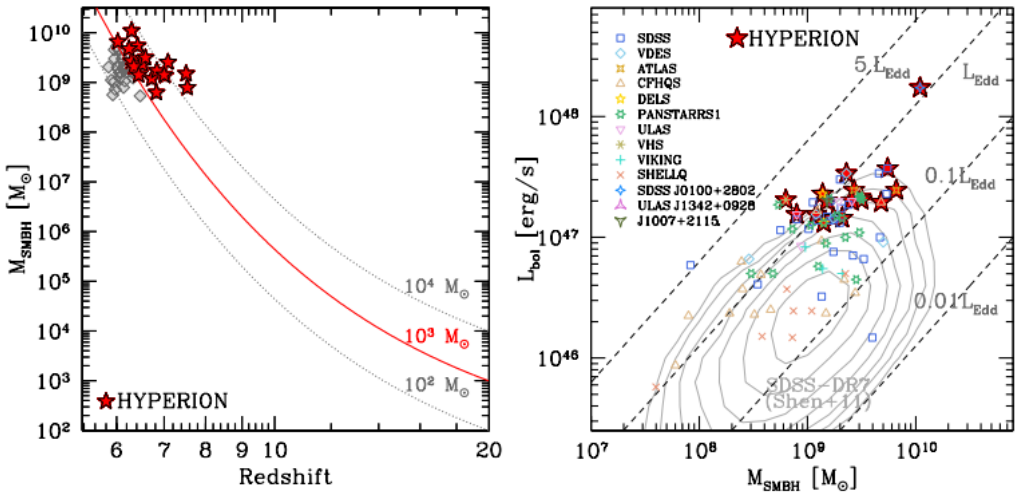

Figure 2.7: Selection and properties of the HYPERION sample. Left: SMBH mass as a function of redshift. All the HYPERION sample (diamonds and stars) are the sub-sample of 46 hyperluminous ($L_{bol} > 10^{47}$ erg s^1) QSOs with measured SMBH masses reported by the end of 2020. The final selected 18 sources are reported as red stars and constitute the HYPERION sample. The curves represent the exponential growth of seed BHs of different masses (labeled) formed at $z = 20$, assuming continuous accretion ($f_{duty} = 1$) at the Eddington rate ($\lambda_{Edd} = 1$). The red curve, corresponding to a growing seed of 1000 $M_\odot$, was used to select the HYPERION sample. Right: distribution of the HYPERION sample (red stars) in the M_{BH} vs. L_{bol} plane (red stars) along with the distribution of the 83 $z > 6$ QSOs with available M_{BH}. All M_{BH} are based on single-epoch MgII virial estimator and L_{bol} is from bolometric correction from the literature as of 2020. M_{BH} and L_{bol} were consistently recomputed for all sources assuming the same ΛCDM cosmology and adopting the mass calibration from Vestergaard and Osmer 2009 and a bolometric correction of 5.15 to the 3000$\mathring{A}$ luminosity from Richards et al. 2006. Dashed lines report the location of sources emitting a fixed fraction of L_{Edd}. The contours report the location of the lower redshift ($z = 0.7$ - 1.9) SDSS-DR7 QSOs from with Mg II derived masses (Shen et al., 2011).

2023). The mass of these BHs were estimated by using the Mg II virial mass estimator by Vestergaard and Osmer (2009). This method employs the FWHM of the Mg II lines and the 3000$\mathring{A}$ continuum luminosity. This choice of mass estimation was conservative and therefore robust because this method by Vestergaard and Osmer (2009) tends to give the lowest SMBH mass estimation among the Mg II based estimators and hence the lowest $M_{s,Edd}$. The average E (B - V) estimated through a spectral energy distribution (SED) analysis for the HYPERION QSOs is < 0.01 (Saccheo et al., submitted) and therefore spectral reddening does not effect the mass estimates. Despite all this, the uncertainties on virial mass estimates are dominated by the systematic reaching 0.3 – 0.5 dex (e.g., Shen and Liu 2012).

Table 2.1 lists the 18 QSOs in the HYPERION sample along with their their celestial coordinates, MgII based redshifts, L_{bol}, M_{BH}, Eddington ratio (λ_{Edd}), and $M_{s,Edd}$. From here on, we refer to the single QSOs with abbreviated names. Table 2.2 show the observation ID, start and end date and time along with the exposure in seconds for the HYPERION sources. For two QSOs (J0224 and J0100), good quality archive X-ray data from *XMM-Newton* were already available and their spectral analysis was presented by Pons et al. (2019) and Ai et al. (2017). Figure 2.8 shows the redhsift distribution of the HYPERION sample. Aside from the novel QSO selection criterion, the novelty of the HYPERION sample is that it builds on the highest quality X-ray data available up to date on $z > 6$ QSOs, allowing for the first time on a large sample of QSOs at EoR, to perform reliable X-ray spectroscopy and a sensitive investigation of the nuclear X-ray properties of these sources. Details on these X-ray data and results from their initial exploitation are reported in Section 3.3.

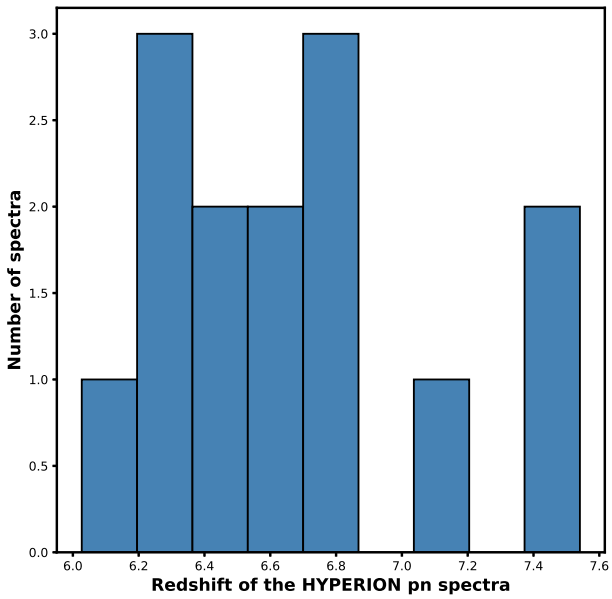

Figure 2.8: Distribution of redshift of the 18 HYPERION spectra.

Name	RA	DEC	z^a	$logL^b_{bol}$ $erg\ \ s^{-1}$	$logM^c_{BH}$ $M_\odot$	λ_{Edd}	$M_{s,Edd}$ $M_\odot$
ULAS J1342+0928	13:42:08.10	+09:28:38.6	7.541	47.19	8.90	1.55	19120
J1007+2115	10:07:58.26	+21:15:29.2	7.494	47.30	9.18	1.05	32460
ULAS J1120+0641	11:20:01.48	+06:41:24.3	7.087	47.30	9.41	0.62	18230
DELS J0038-1527	00:38:36.10	-15:27:23.6	7.021	47.36	9.14	1.32	7983
DES J0252-0503	02:52:16.64	-05:03:31.8	6.99	47.12	9.15	0.74	7679
VDES J0020-3653	00:20:31.47	-36:53:41.8	6.834	47.16	9.24	0.66	5753
VHS J0411-0907	04:11:28.62	-09:07:49.7	6.824	47.31	8.80	2.57	2019
VDES J0244-5008	02:44:01.02	-50:08:53.7	6.724	47.19	9.08	1.02	2814
PSO J231.6-20.8	15:26:37.84	-20:50:00.7	6.587	47.31	9.50	0.51	4708
PSO J036.5+03.0	02:26:01.88	+03:02:59.4	6.533	47.33	9.49	0.55	3776
VDES J0224-4711	02:24:26.54	-47:11:29.4	6.526	47.53	9.36	1.18	2730
PSO J011+09	00:45:33.57	+09:01:56.9	6.444	47.12	9.15	0.74	1279
SDSS J1148+5251	11:48:16.64	+52:51:50.2	6.422	47.57	9.74	0.54	4627
PSO J083.8+11.8	05:35:20.90	+11:50:53.6	6.346	47.16	9.32	0.55	1324
SDSS J0100+2802	01:00:13.02	+28:02:25.8	6.300	48.24	10.04	1.26	5799
ATLAS J025-33	01:42:43.70	-33:27:45.7	6.294	47.39	9.57	0.72	1392
CFHQS J0050+3445	00:50:06.67	+34:45:22.6	6.246	47.29	9.68	0.32	2072
ATLAS J029-36	01:59:57.97	-36:33:56.6	6.027	47.39	9.82	0.30	1220

Table 2.1: The Hyperion QSO sample, ordered by decreasing redshift, and its general properties. See Zappacosta et al. (2023) and reference therein. ^{a}: measured from the MgII emission line; ^{b}: estimated from luminosity 3000$\mathring{A}$ ($L_{3000\mathring{A}}$,from Vestergaard and Osmer (2009)); ^{c}: measured from single epoch virial mass estimator employing the FWHM of the MgII line and $L_{3000\mathring{A}}$ from Vestergaard and Osmer (2009).

Observation ID	Target	Observation start date	Observation end date	Exposure (s)
884992901	ATLASJ029-36	2022-01-03 17:05:23.000	2022-01-04 18:10:23.000	90300
884992601	CFHQSJ0050+3445	2021-06-26 18:27:30.000	2021-06-27 07:14:10.000	46000
886221401	VST-ATLAS J025.6821-	2023-07-19 18:13:20.000	2023-07-20 20:34:10.000	94850
0790180701	SDSSJ010013.13+28022 *	2016-06-29 17:53:42	2016-06-30 12:03:42	65400
884992401	PSOJ083.8+11.8	2022-03-14 00:46:23.000	2022-03-15 01:13:03.000	88000
886220301	SDSSJ1148+5251	2022-11-08 10:18:38.000	2022-11-09 10:23:38.000	86700
884992101	PSOJ011+09	2021-07-15 18:14:32.000	2021-07-16 18:07:52.000	86000
886220201	PSOJ011+09	2023-01-13 05:43:34.000	2023-01-14 06:10:14.000	88000
0824400301	VDESJ0224-4711*	2018-05-25 01:37:09	2018-05-25 11:35:29	35900
884992001	PSOJ036.5+03.0	2021-07-19 18:11:14.000	2021-07-20 18:37:54.000	88000
884994101	PSOJ036.5+03.0	2024-01-09 05:14:38.000	2024-01-10 04:17:58.000	83000
886210901	PSOJ231.6-20.8	2023-07-31 17:48:47.000	2023-08-01 17:47:07.000	86300
886210801	PSOJ231.6-20.8	2022-08-14 16:33:14.000	2022-08-15 21:09:54.000	103000
884991701	PSOJ231.6-20.8	2021-07-29 17:30:46.000	2021-07-31 01:50:46.000	116400
884991501	VDESJ0244-5008	2021-08-04 17:03:07.000	2021-08-05 18:09:47.000	90400
886210301	VHSJ0411-0907	2022-07-31 17:38:19.000	2022-08-01 20:02:29.000	95050
884991101	VDESJ0020-3653	2022-01-01 05:50:36.000	2022-01-02 06:33:56.000	89000
886210201	VDESJ0020-3653	2022-11-16 20:22:25.000	2022-11-17 20:35:45.000	87200
886200901	DESJ0252-0503	2023-07-29 17:36:59.000	2023-07-30 16:40:19.000	83000
886201001	DESJ0252-0503	2023-07-25 17:51:20.000	2023-07-26 18:43:00.000	89500
886200701	DELSJ0038-1527	2022-07-03 18:57:25.000	2022-07-04 18:00:45.000	83000
884990701	DELSJ0038-1527	2023-12-10 04:30:34.000	2023-12-11 06:58:54.000	95300
884990401	ULASJ1120+0641	2021-06-27 18:30:48.000	2021-06-28 15:17:28.000	74800
886201201	J1007+2115	2022-05-28 20:52:09.000	2022-05-29 20:02:09.000	83400
884993801	ULASJ1342+0928	2021-12-24 12:49:15.000	2021-12-25 18:52:35.000	108200
884990101	ULASJ1342+0928	2021-07-05 18:18:38.000	2021-07-07 00:46:58.000	109700

Table 2.2: Journal of the observations of the HYPERION targets from the XMM-HYPERION and archive data (marked with *)

Chapter 3

The XMM-Newton X-ray Observatory and The XMM Heritage Program on HYPERION

3.1 Basics principles of X-ray astronomy

The typical rate of arrival of X-ray photons from a celestial source is quite low and for distant AGN they can be as low as a photon every 10^3 - 10^4 seconds. This means that in X-ray astronomy, unlike in the UV/optical/infrared bands, we can literally counts every incoming photon. Solid-state detectors (like CCDs) are used therefore in normal conditions in a photon counting regime and for each photon we can basically collect time of arrival, position and its energy. In this case each detected photon can be reported as a "count" or "event" in the detector. This means that from a single X-ray observation we can generate several observable: light curves (number of photons as a function of time), images (distribution of photons across the detector area), spectra (number of photons collected per unit of energy). Every observable can be generated for each particular choice of the different information recorded during the observation and is limited by the characteristics of the detectors in resolution of time, point spread function and energy resolution. For spectral analysis, which is the main focus of this thesis, we can select, in principle, all the photons per unit of energy recorded in a particular detector position (i.e. the position of an X-ray emitting source) and for a certain interval of time

during the observation. Since what we are recording in a CCD is not only the charge from photons from celestial sources, but also the charge from photons from the diffuse cosmic X-ray background (a mixture of diffuse foreground plasma emission from our Galaxy and distant background from unresolved AGN emission), the charge from the instrumental noise of the detectors and the charge from the interaction of surrounding particles interacting with the detectors and the satellite structure, we need to account and remove for this additional background in our spectrum. We can do so by first removing the time intervals of the observation we are badly affected by the surrounding particle background which generally increase the number of counts (events) detected across the entire detector, lowering the signal-to-noise ratio of the entire observation (Figure 3.1). Furthermore we can extract a spectrum from a region of the detector nearby the source we are interested in and subtracting it (appropriately normalized for the extraction area) to the source spectrum. It is important to highlight the fact that the spectrum we obtain from a X-ray observation is not the the spectrum F(E) of the source but it is a convolution of it with the instrumental response function of the detector. In particular for the analysis of a spectrum, it is necessary to consider 2 additional files: The spectral response matrix (RMF) and the Auxiliary Response File (ARF). RMF (R(J,E)) gives the probability that a photon of energy E falls inside a certain energy channel (J) of the detector. So essentially the convolution of the source spectrum F(E) with the spectral response matrix R(J, E) generates the spectrum in energy channels C(J).

The product of the spectral observations on the detector, C(J), is given as:

$$C(J) = t_{exp} \times R(J, E)F(E)A(E) \tag{3.1}$$

where t_{exp} is the exposure time is in seconds. A(E) is the ARF which includes information on the effective area, filter transmission, and any additional energy-dependent efficiencies (see Figure 3.6). The combination of RMF and ARF produces the input spectrum weighted by telescope area and detector efficiencies vs. energy.

In principle, one could determine F(E) by inverting the matrix F(E)=C(J)R_{-1}(J,E). Practically this inversion is impossible because the matrix is extremely complicated and the inversion results are unstable and non-unique. This causes uncertainties in the

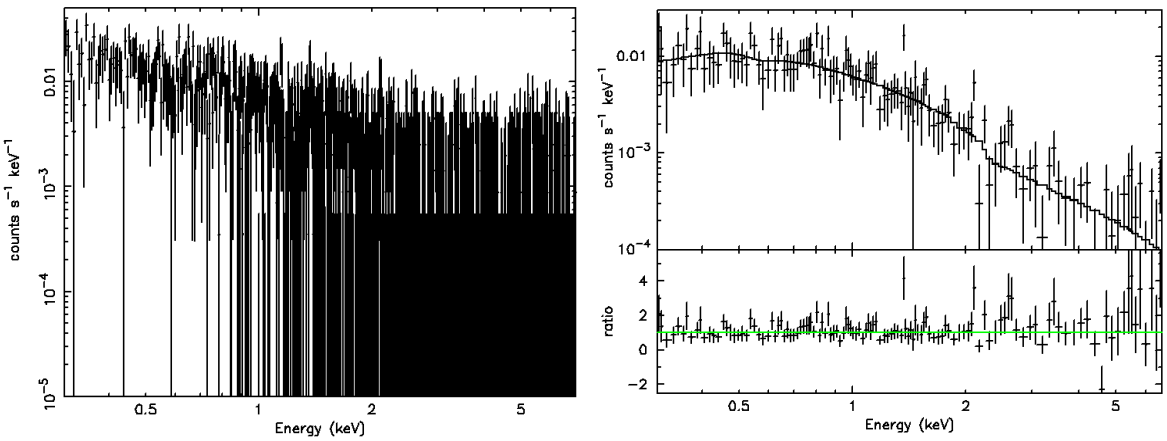

Figure 3.1: Simulated unbinned spectra using (left). The same spectra that has been binned with 10 counts per bin (right) along with a best fit model.

estimation of background counts (Poissonian counts), effective area, detector efficiency and other parameters. In practice, we choose a spectral model that is simple and without too many parameters, convolve it for the response matrix and compare it using the χ^2 test with the observed spectrum. This is called forward fitting. This is given as

$$\chi^2 = \frac{(C(J)_{observed} - C(J)_{expected})^2}{\sigma_J^2} \tag{3.2}$$

where σ_J is the error on the J$^{\text{th}}$ channel.

The parameters are varied until the χ^2 statistic is minimized and can better approximate the observed spectrum. This is called the best-fit model. It is possible to exclude a model by assuming a certain level of confidence, but it is never possible to conclude that that is the only acceptable one.

To use the χ^2 it is necessary to rebin the counts into multiple groups so that the distribution of the counts of each bin approximates a Gaussian distribution. For this, we need at least 20 counts in each bin of a spectrum. Otherwise, we use Cash statistics (Poisson distribution) (Cash, 1979). Figure 3.1 shows an unbinned spectra and another spectra that has been binned with 10 counts per bin almong with a best fit model.

Once the best-fit values of the parameters are obtained, we also have to determine the confidence interval of the parameters within which one can be relatively confident that the true parameter falls. For this purpose, we utilize confidence intervals of the total probability distribution, typically selecting curves with constant values of χ^2.

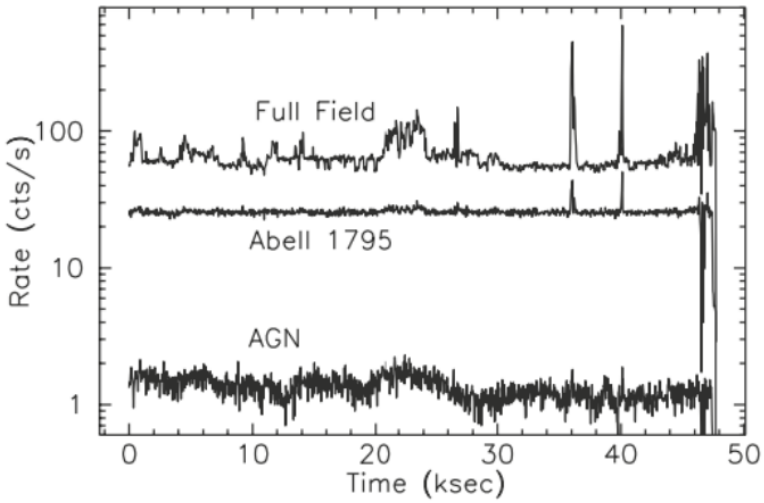

Figure 3.2: Count rates from *XMM-Newton* observations containing a cluster (A1795) and an AGN. Short flares can be seen as well as a longer period of enhanced background in the middle of the observations.

These are tabulated according to the confidence level at which the interval is desired and the number of parameters of interest in determining it. This is also valid for Cash statistics. The models are normally made up of individual components that are added or multiplied together.

It should be noted that rebinning the X-ray data to increase the number of counts per bin can lead to a loss of information. Emission lines or absorption edges that are important features in a spectrum can be lost during binning. But if the spectrum is of low quality, implying that it has only a handful of counts and no sharp features are expected, then rebinning provides a convenient way to perform spectral analysis.

X-ray observations in *XMM-Newton* images are affected by various types of noise and background. The noise includes the Cosmic X-ray Background (CXB) due to Galactic diffuse X-ray emission and the combination of many not resolved extra-galactic sources (AGNs and SN remnants), internal background from high energy particles interacting with the detector, intrinsic detector noise from dark currents in the electronics, and soft protons. Soft protons (E $\geq$ 100 keV) are a specific background that occurs during XMM observations when the detector interacts with high energy particles in the Earth's magnetosphere during its orbit around the Earth. These are seen as bright and highly variable flares during the observation (see Figure 3.2). These backgrounds can

be identified and eliminated due to their very high energy.

X-ray spectra of astrophysical, distant ($z >> 2$) sources are often characterised by relatively low numbers of counts per spectral bin. If we binned the data with least at 20 counts per bin, we can fit with χ^2. For χ^2 statistics, the goodness of fit is given by as:

$$\chi^2 = \sum_{i=1}^{N} \frac{(N_i - s_i)^2}{\sigma_i^2} \tag{3.3}$$

where the summation over i is over all N bins of the spectrum, N_i is the observed number of counts, s_i is the expected number of counts for the tested model, and $\sigma_i^2 = s_i$ for Poissonian statistics. For χ^2 statistics both the model s_i and the observed spectrum N_i should include the source plus background counts to properly use Poissonian statistics. Also, minimisation of χ^2 to obtain the best-fit parameters of the model is easier when σ_i^2 is approximated by N_i, which is a reasonable approximation when N_i is large and the Poissonian distribution approaches a normal distribution (typically at $>$ 20 counts per bin), but it fails for small N_i, which can be easily seen by putting $\sigma_i = 0$ in Equation 3.3. Also, in case of small N_i, rebinning has the risk of washing out spectral details. Cash statistic given as,

$$\tilde{C} = 2 \sum_{i=1}^{N} s_i - N_i ln(s_i) \tag{3.4}$$

is a much better statistic and can be applied to bins with a small number of counts without any bias in the derived parameters. Also, this statistic can be used to derive uncertainty ranges on the parameters of the model. A modification of the original Cash statistic is implemented in current fitting packages such as XSPEC (Arnaud, 1996). This modified Cash statistic, designated here as cstat, is defined as,

$$\tilde{C} = 2 \sum_{i=1}^{N} s_i - N_i + N_i ln(N_i/s_i) \tag{3.5}$$

This has similar properties as the original Cash statistic, but in addition it can be used to assign a goodness-of-fit measure to the fit. For a spectrum with many counts

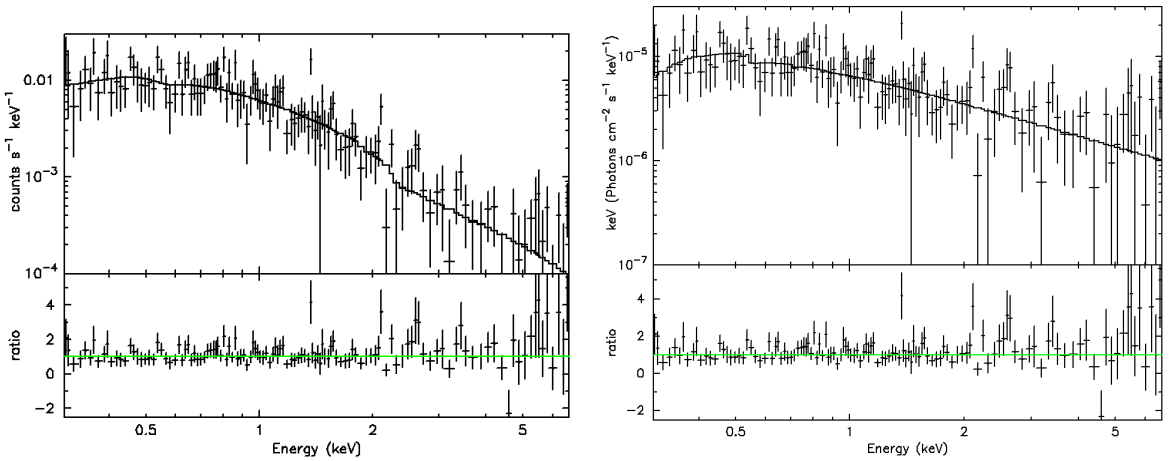

Figure 3.3: (Left) show a binned folded spectrum along with a best fit model. (Right) we see the same spectra represented as unfolded spectrum and model.

per bin Cash statistic $\rightarrow \chi^2$, but where the predicted number of counts per bin is small, the expected value for Cash statistic can be substantially smaller than the number of bins n. However, unlike χ^2, the Cash statistic may be used regardless of the number of counts in each bin. The magnitude of the Cash statistic depends upon the number of bins included in the fit and the values of the data themselves. Hence one cannot analytically assign a goodness-of-fit measure to a given value of the Cash statistic.

For the X-ray analysis, we typically use a spectral fitting software, and here we utilize XSPEC, which enables us to perform forward-fitting spectral analysis. XSPEC allows us to apply models combining both additive components (e.g., power-laws, Gaussians) and multiplicative components (e.g., tbabs for absorption). Although we generally work with models folded by the instrument response function—meaning we account for how the instrument distorts the observed spectrum—once we find the best-fit model, we can unfold the spectrum. This allows us to visualize how the actual source spectrum would appear if the adopted model is correct, effectively removing the instrument's influence. Figure 3.3 shows a comparison between folded and unfolded spectrum.

The unfolded spectrum is the original source spectrum prior to detection and is free from instrumental effects of the detector. The data points for the unfolded spectra are plotted by calculating $D \times \frac{unfolded \quad model}{folded \quad model}$ where D is the observed data, unfolded model is the theoretical model integrated over the plot bin, and folded model is the model times the response as seen in the standard plot data. *eufspec* plots the unfolded

spectrum and model in terms of Ef(E). The E used in the multiplicative factor is taken to be the geometric mean of the lower and upper energies of the plot bin.

3.2 The Observatory

In 1999 the European Space Agency (ESA) launched the *X-ray Multi-Mirror Mission (XMM-Newton)* which is ESA's second cornerstone of the Horizon 2000 Science Program. It carries 3 high throughput X-ray telescopes with an unprecedented effective area, and an optical monitor, the first flown on a X-ray observatory. The large collecting area and ability to make long uninterrupted exposures provide highly sensitive observations.

Since Earth's atmosphere blocks out all X-rays from reaching the ground, only a telescope in space can detect and study celestial X-ray sources. The *XMM-Newton* mission is helping scientists to solve a number of cosmic mysteries, ranging from the enigmatic BHs to the origins of the Universe itself. Observing time on *XMM-Newton* is being made available to the scientific community, applying for observational periods on a competitive basis.

The *XMM-Newton* satellite is configured modularly and is composed of four main elements as shown in Figure 3.4:

- The Focal Plane Assembly (FPA) that consits of the Focal Plane Platform (FPP) carrying the focal-plane instruments: two Reflection Grating Spectrometer (RGS) readout cameras, an EPIC-pn and two EPIC-MOS imaging detectors, and the data handling and power distribution units for the cameras. The EPIC and RGS instruments are fitted with radiators, which cool the CCD detectors via cold fingers.

- The Telescope Tube (a long carbon fibre tube) that maintains the relative position between the FPA and the MSP. Due to its length of 6.80 m, the Telescope Tube is physically composed of two halves: the upper and lower tubes. The upper tube includes two reversible venting and outgassing doors (VOD), and supports the outgassing baffle (OGB).

- Figure 3.4 shows the Mirror Support Platform (MSP) that consists of the platform itself and carrying the three mirrors assemblies (Mirror Modules + entrance and exit baffles + doors + two RGS grating boxes), the Optical Monitor (OM) and the two star-trackers.

- The Service Module (SVM), which carries the spacecraft subsystems and associated units providing the necessary resources to the satellite. Also attached to the SVM are the two solar-array wings, the Telescope Sun Shield (TSS) and the two S-band antennas mounted on their booms.

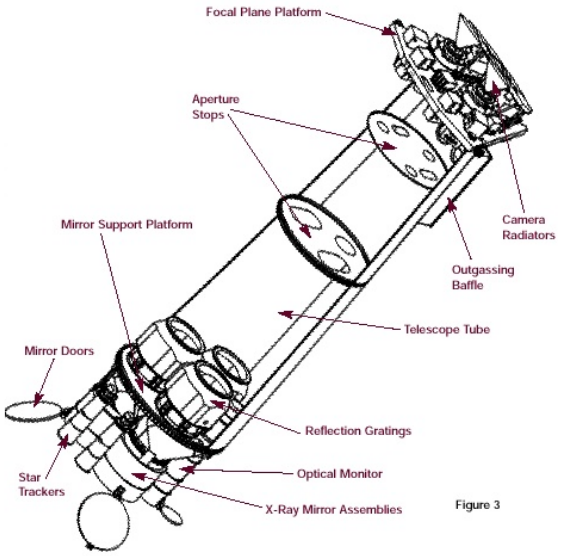

Figure 3.4: The *XMM-Newton* satellite is configured modularly and is composed of four main elements:The Focal Plane Assembly (FPA),The Telescope Tube, The Mirror Support Platform (MSP) and The Service Module (SVM).

Figure 3.4 shows each of the *XMM-Newton* telescopes consists of:

- the mirror assembly door, which protected the optics during integration, launch and early orbit phase,

- the entrance baffle, which provides visible straylight suppression at angles larger than 47°,

- the X-ray baffle,

- the Mirror Module,

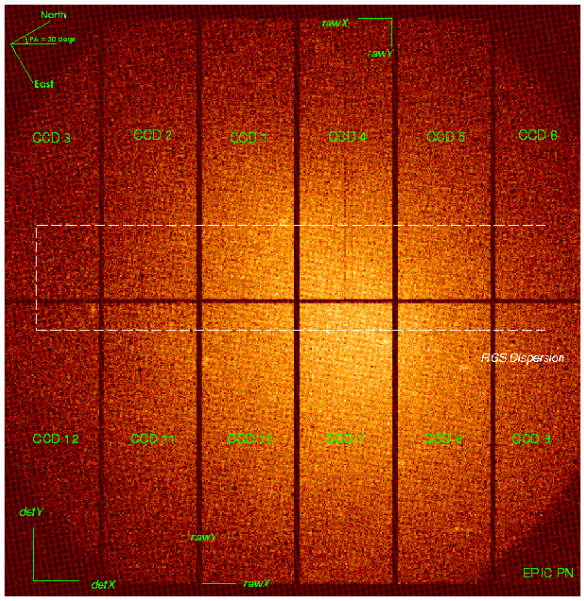

Figure 3.5: The layout of the EPIC-pn camera as presented in SAS. The orientation of the RAWX/RAWY (CCD specific) and of the DETX/DETY axes are shown, to highlight that the RGS dispersion axes are parallel within spacecraft physical coordinates. The readout CAMEX of each CCD is located at RAWY = 0, i.e. at the top (for CCDs 1 - 6) or bottom (for CCDs 7 - 12) of the displayed array. In the upper left corner, the orientation of the celestial North and East axes is displayed for an assumed position angle (PA) of 30°.

- an electron deflector, which produces a circumferential magnetic field which prevents low energy electrons reflected by the mirrors reaching the focal plane detectors, in two of the telescopes, the Reflection Grating Array, and

- the exit baffle, which provides an appropriate thermal environment.

3.2.1 The European Photon Imaging Camera (EPIC)

The EPIC system aboard *XMM-Newton* consists of three European Photon Imaging Cameras. It includes two Metal Oxide Semi-conductor (MOS)-CCD cameras and a single pn-CCD camera. The EPIC pn camera is made of 12 rectangular back-illuminated CCDs, each with a FOV of 13.6 .4 arcmin^2, for a total sensitive area of 6 $\times$ 6 cm^2 (see figure 3.5). A radiator cools the camera to $-90°C(-130°F)$. This system was made by the Astronomisches Institut Tübingen, the Max Planck Institute for Extraterrestrial Physics, and PNSensor (Strüder et al., 2001).

Each MOS-CCD is a squared array of 600 pixel covering a field of view (FOV) of 10.9 $\times$ 10.9 arcmin^2 bringing the total imaging area to 2.5 $\times$ 2.5 cm^2 and a FOV with 30 arcmin in diameter (see figure 3.6). Each camera has a large adjacent radiator which cools the instrument to an operating temperature of $-120°C(-184°F)$. They were developed and built by the University of Leicester Space Research Centre and English Electric Valve Ltd (Turner et al., 2001).

The EPIC detectors are sensitive to X-ray photons and also to IR, visible and UV light. So the cameras include aluminised optical blocking filters to reduce the contamination of the X-ray signal by those photons. Each EPIC camera has four filters: thin, medium, and thick. Two are thin filters made of 1600$\mathring{A}$ of polyimide film with 400$\mathring{A}$ of aluminium evaporated on to one side; one is the medium filter made of the same material but with 800$\mathring{A}$ of aluminium deposited on it; and one is the thick filter. This is made of 3300$\mathring{A}$ thick Polypropylene with 1100$\mathring{A}$ of aluminium and 450$\mathring{A}$ of tin evaporated on the film. The filters are self-supporting and 76 mm in diameter. The remaining two positions on the filter wheel are occupied by the closed (1.05 mm of aluminium) and open positions, respectively. The former is used to protect the CCDs from soft protons in orbit, while the open position could in principle be used for observations where the light flux is very low, and no filter is needed.

Both EPIC-MOS and EPIC-pn detect photons in the same energy band, about 0.3 - 10 keV. In terms of the effective area, the EPIC pn is the most sensitive detector on board, especially at E $<$ 2 keV. The effective are of MOS and pn are shown in Figures 3.6a and 3.6b.

All three detectors can be used simultaneously to create images of a target as well as take spectra. The CCDs can also give a precise time when a given X-ray photon hits them. The main difference between the EPIC-MOS detectors and the EPIC-pn detector, in fact, is in the time resolution. The EPIC-MOS can distinguish between two X-ray photons falling on it in an interval of 1.5 milliseconds, while the EPIC-pn has a much better time resolution of 0.03 milliseconds, or 30 microseconds. As a trade-off, the EPIC-MOS detectors have slightly higher spatial resolution: they can distinguish objects about a quarter the size that the EPIC-pn detector can.

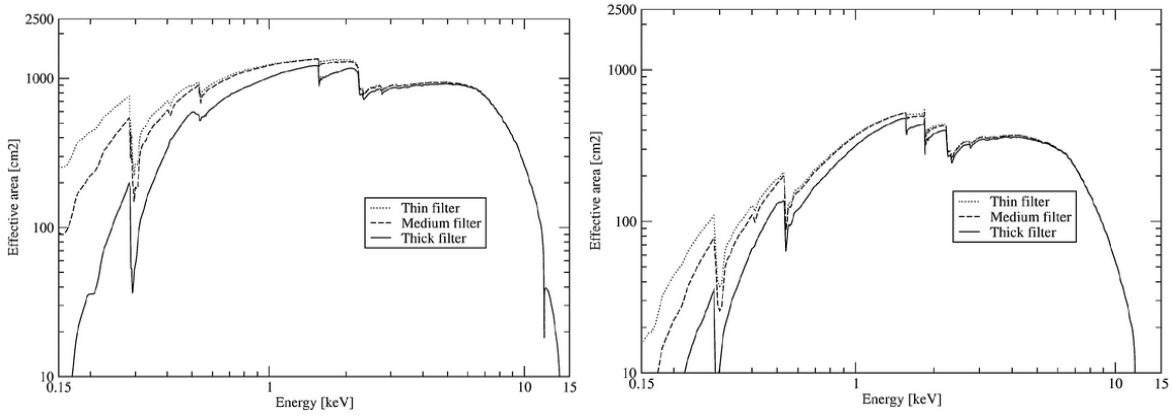

(a) EPIC-MOS (b) EPIC-pn

Figure 3.6: Effective area for each of the optical blocking filters and without a filter

3.2.2 Reflection Grating Spectrometers (RGS)

The Reflection Grating Spectrometers (RGS) consist of two Focal Plane Cameras and Reflection Grating Arrays(RGAs). This system is used to create X-ray spectral data and can determine the elements present in the target, as well as the temperature, quantity and other characteristics of those elements. Operating in the 2.5 to 0.35 keV (5 to 35$\AA$) range, the RGS can detect carbon, nitrogen, oxygen, neon, magnesium, silicon, and iron (Den Herder et al., 2001).

The Focal Plane Cameras have nine EPIC-MOS-CCD devices arranged in a Rowland circle, with each device containing 384 × 1024 pixels. The CCD arrays are surrounded by a protective wall, cooled to - 110 °C, and were built collaboratively by SRON, Paul Scherrer Institute, MSSL, EEV Ltd, and Contraves Space. The Reflection Grating Arrays are attached to two telescopes, allowing approximately 50% of the incoming X-rays to pass unperturbed to the EPIC system, while redirecting the other 50% onto the Focal Plane Cameras. The RGAs were built by Columbia University (Den Herder et al., 2001).

3.2.3 The Optical Monitor (OM)

The Optical Monitor (OM) is a 30 cm (12 in) Ritchey–Chrétien optical/ultraviolet telescope designed to provide simultaneous observations alongside the spacecraft's X-ray instruments. The telescope is based on the principle of grazing incidence. As

X-ray photons have very high energies, they would pass through the reflecting surface unless the angle is nearly 90°. The incoming X-ray is first reflected by a parabolic surface towards a second hyperbolic surface, which deviates the ray to the primary focal plane. In *XMM-Newton*, each mirror module is a grazing-incidence Wolter I telescope consisting of 58 gold-coated nested mirrors. Each mirror shell consists of a paraboloid and an associated hyperboloid which were replicated together in one piece to facilitate alignment and integration. These configurations not only allow us to obtain efficient reflection of the X-ray photons but improve also the collecting area. One telescope has a light path as shown in Figure 3.7 where the EPIC pn is mounted at the primary focus. The other two have grating assemblies in their light paths, diffracting part of the incoming radiation onto a secondary focus. In particular 44% of the incoming light focused by the mirrors is directed onto the camera at the primary focus (where the MOS is mounted), while 40% is dispersed by the grating array onto a linear strip of CCDs (RGS).

It is sensitive between 170 and 650 nanometres in a 17 × 17 arcminute square field of view co-aligned with the centre of the X-ray telescope's field of view. It has a focal length of 3.8 m (12 ft) and a focal ratio of f/12.7 (Mason et al., 2001). The CCD is 384 × 288 pixels in size, of which 256 × 256 pixels are used for observations; each pixel is further subsampled into 8 × 8 pixels, resulting in a final product that is 2048 × 2048 in size. The Optical Monitor was built by the Mullard Space Science Laboratory with contributions from organisations in the United States and Belgium (Mason et al., 2001).

3.3 The XMM Heritage Program on HYPERION

For 16 high$-z$ QSO, (Zappacosta et al., 2023) have a 2.4 Ms *XMM-Newton* Multii-Year Heritage program (PI L. Zappacosta; Proposal ID 088499) approved in December 2020 with a three-year time span designed to collect unprecedented high-quality X-ray data for such a large sample of QSOs at EoR. Specifically, the HYPERION *XMM-*

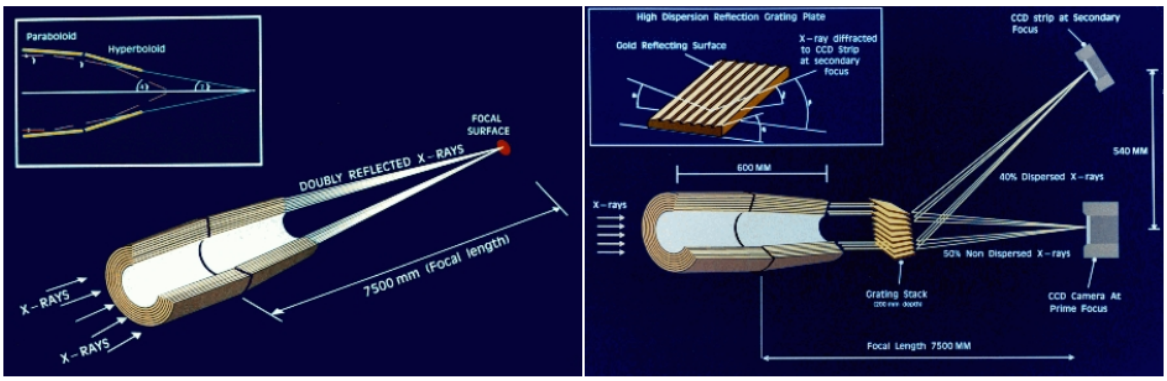

Figure 3.7: Light path in the *XMM-Newton* telescope with only an EPIC camera in its primary focus (left), and in the two telescopes in which a RGA is mounted into the optical path (right)

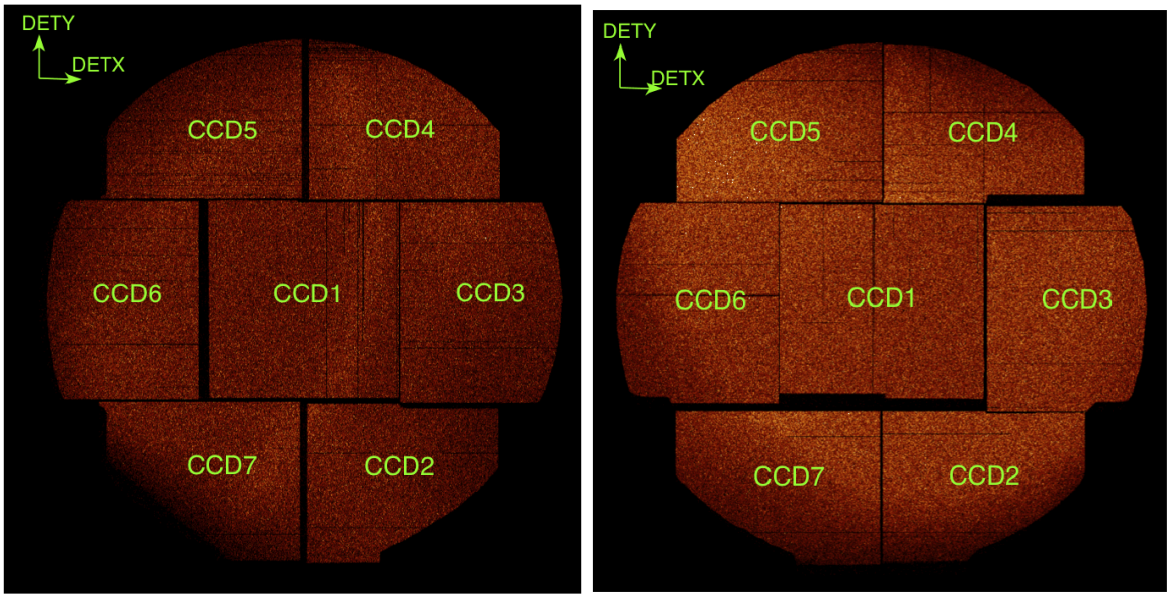

(a) EPIC-MOS 1 (b) EPIC-MOS 2

Figure 3.8: The layout of the EPIC-MOS cameras is presented in this figure for EPIC-MOS1 and EPIC-MOS2. The images (in detector coordinates [DETX,DETY]) are extracted from an exposure taken with the calibration (CAL_CLOSED) filter in Rev.#80 (Obs.#0124700101). The number of the CCD where each photon has fallen is included in the CCDNR column of the calibrated event list files. The EPIC-MOS cameras are orthogonally oriented. Hence, the RGS dispersion direction is aligned with the DETY direction in the EPIC-MOS1 camera, while it is aligned along the DETX direction in the EPIC-MOS2 camera.

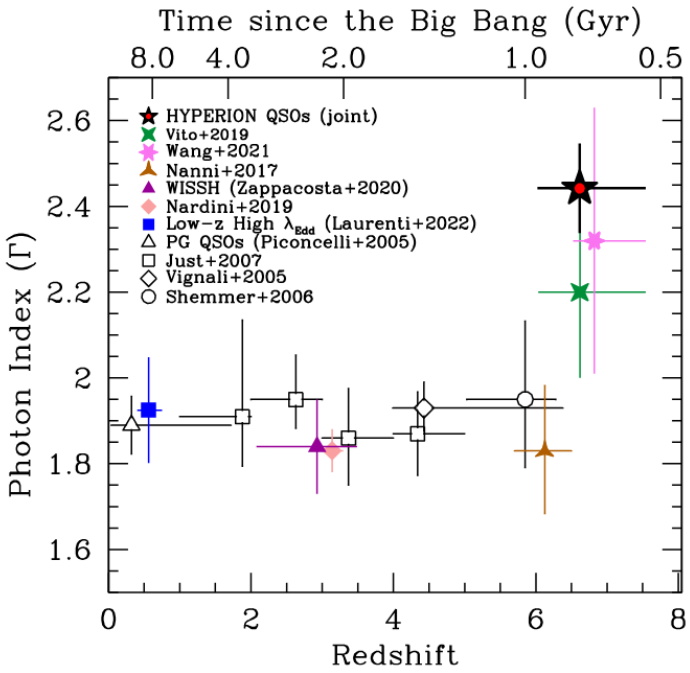

Figure 3.9: Distribution of the average Γ as a function of redshift. The black star shows the joint analysis Γ value compared with the results of other, independent joint analyses of $z \geq 6$ QSOs. See Zappacosta et al. (2023) and references therein.

Newton Multi-Year Heritage program (hereafter XMM-HYPERION) is collecting, for the first time, X-ray data for seven sources and is improving the data quality for nine previously observed sources for which the X-ray data available are of limited quality (i.e., poor detection or non-detection; e.g., Vito et al. 2019; Pons et al. 2019; Connor et al. 2020). The aim of XMM-HYPERION is to achieve the high-quality data standard obtained for the unlensed QSOs J0224 and J0100 (i.e., at least 100 net counts from pn+MOS1+MOS2 data in the 0.5 - 10 keV band) for all QSOs in the sample. This would ensure a $\sim 10\%$ accuracy level (1σ) characterization of X-ray spectral properties, namely the photon index of the power-law and the unabsorbed 2 - 10 keV luminosity ($L_{2\text{-}10}$) on these sources.

Zappacosta et al. (2023) reported data from the first year of observation of the XMM-HYPERION program. They presented $\sim$ 0.94 Ms of new data on 10 sources, which increased to $\sim$1.04 Ms with the addition of the two archived data. Table 2.2 shows the details of the XMM-HYPERION observations. They found that X-ray spectral analysis on individual sources using simple power-law models on spectra with 50 – 140 net counts (pn+MOS) in the 0.3 - 7.0 keV range revealed a wide range of spectral

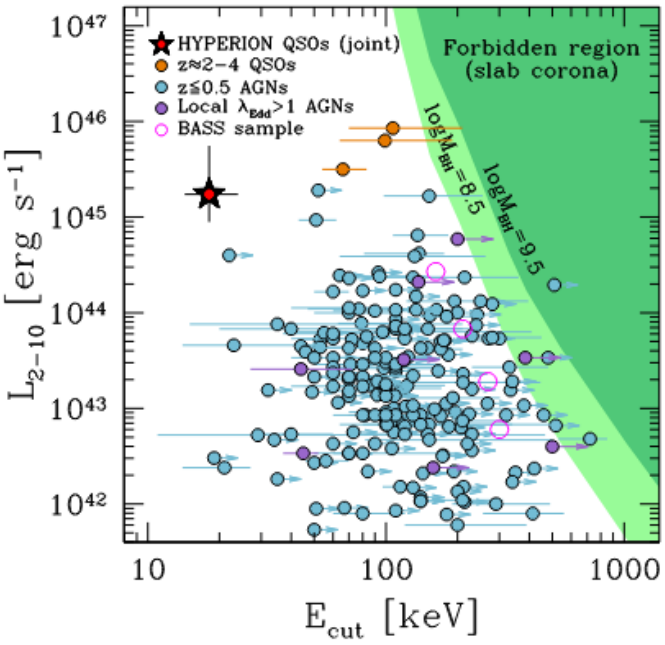

Figure 3.10: Distribution of E_{cut} as a function of $L_{2\text{-}10}$. Light blue and orange filled circles are estimates from a compilation of local AGN (Bertola et al. 2022, and references therein) and z ≈ 2 - 4 QSOs (Lanzuisi et al. 2019; Bertola et al. 2022). Purple circles are from local super Eddington accreting AGN from Tortosa et al. (2023). The HYPERION average E_{cut} measurement (assuming $\Gamma = 1.9$) from the joint analysis by Zappacosta et al. (2023) is marked in black. Green regions are the forbidden regions (for a slab corona model) due to runaway electron-positron pair production (see Svensson 1984) for $\log(M_{BH}/M_\odot) = 8.5$ and $\log(M_{BH}/M_\odot) = 9.5$.

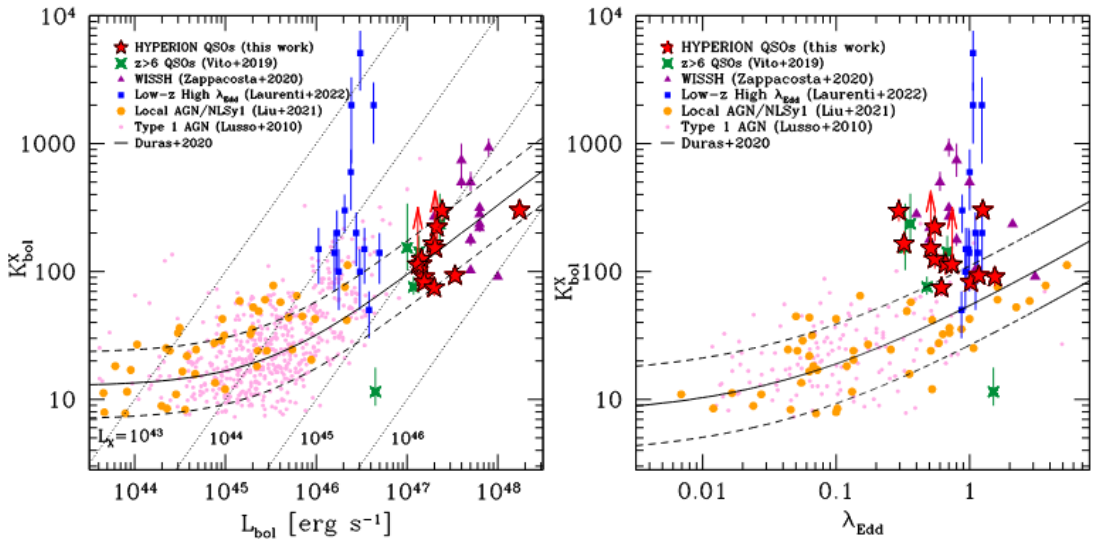

Figure 3.11: The red stars represent the HYPERION sample from Zappacosta et al. (2023).(Left) K^X_{bol} vs. L_{bol} for a compilation of broad-line mostly high$-z$ QSOs and local AGN. (Bottom) K^X_{bol} vs. λ_{Edd} for the same sources with SMBH measurements available.

indices (Γ) between approximately 1.9 to 3, with 80% of sources having a steep $\Gamma > 2.1$. A joint analysis of the 10 detected sources resulted in an average Γ of about 2.4 (see Figure 3.9), ruling out a canonical $\Gamma = 2$ at $\sim 4\sigma$ level and the average Γ reported in $z < 6$ QSOs of similar luminosity or λ_{Edd}. This implies that the steepness of the X-ray spectrum in HYPERION QSOs is an evolutionary signature of the HYPERION QSOs regardless of the QSO radiative output or SMBH accretion rate. Given the high rest-frame energies probed in these sources, the steep spectral slopes can be explained as the onset in the observed energy band of the redshifted power-law (high-energy) cutoff E_c.

Under this hypothesis, and assuming a canonical $\Gamma = 1.9$, they found a low-energy $E_c \sim 20$ keV. This low E_c is almost unreported in the literature for both the bulk of the AGN and luminous QSO populations and at all redshift as can be seen in Figure 3.10. This low cutoff was previously unreported at such high luminosities and redshifts. They also found that the X-ray bolometric correction aligns with high-z AGN trends, but the optical-to-X-ray spectral index is slightly higher than the relations reported for large AGN samples (see Figure 3.11). This is due to the steep X-ray slopes in HYPERION QSOs. From their analysis they concluded that these sources are in a new regime for their X-ray properties similarly to the local highly accreting NLSy1 galaxies. The steep

spectral slope indicates a low temperature corona, due to highly accreting disk emission whose strong UV radiative output reprocessed by the corona favour the coronal cooling.

Chapter 4

The Average Spectrum of Quasars at $z > 6$

4.1 Analysis Methods of Limited Quality X-ray Spectra

The X-ray emission of very high$-z$ ($z > 6$) luminous QSOs, is characterized by faint fluxes (given their distances) and therefore is mainly limited by the background giving limited data quality and leading to poorly constrained parameter estimation. The HYPERION QSO sample, considering only pn spectra (as these will be the data we will focus on in this work), has sources with net-counts as low as 19 (J0252) in the 0.3 - 7.0 keV energy range. Other than J0100 and J1148 which has 225 and 107 net-counts in the pn spectra, the average net-counts is $\sim$ 80 and the pn spectra net-counts considering all 18 QSOs is $\sim$ 1250. In case of spectra with such low number of net-counts, estimation of spectral parameters have large errors associated with them. As an example, in case of a power-law model, if we have a best fit Γ estimated as 2.5 ± 0.5, then the fractional accuracy ≈ 0.2, implying a 20% error on Γ. A possible solution to improve the constrains for the average value of a sample or population is to perform a joint analysis (Zappacosta et al., 2023) or to combine all the spectra together, through a spectral stacking procedure, a possibility we discuss in this work. Joint analysis can, in principle, give a good constrain on the determination of the average spectral prop-

erties of a population of sources allowing at the same time to have good control of the possible source variability or detector inter-calibration systematic uncertainties. But joint analysis can be challenging and computationally intensive when a lot of data sets are present. For the HYPERION QSO sample, we have 18 sources and each source has 3 spectra from pn, MOS1 and MOS2. So in principle we have 54 (18×3) spectra. This is without considering the fact that several sources have multiple observations. If we use a simple power-law model to parameterize the average X-ray coronal emission, modified at low energies by photoelectric absorption from the Galactic interstellar medium, accounting also for possible detector intercalibration systematics we have a model with 270 parameters to control. This data analysis methodology has been exploited on a limited HYPERION Heritage Program dataset by Zappacosta et al. (2023). This procedure, therefore, is complex and time consuming. Combining the spectrum via spectral stacking, has the advantage of requiring a faster and less complex analysis. Further more we can evaluate through residuals the presence of continuum component that might be different from the our baseline power-law continuum model, i.e., presence of high energy cutoff, or reflection component or low energy absorption. We can also study the presence of lines in absorption or emission which would be expected. We might also see the presence of unexpected components. Spectral stacking consists of appropriately combining all the spectra together, through an averaging process, in one single spectrum which increases signal to noise ratio. The disadvantage of this procedure is that we cannot property account for spectral variability of the single spectra in each source (but QSOs typically varies in flux over many years timescales). Another disadvantage is that we have limited control on the cross-calibration systematics among different detectors, but with the data quality of our spectra this term is dominated by the large statistical uncertainties in our spectra.

4.2 Combining the X-ray Spectra

We choose to average the spectra according to the prescription given by Corral et al. (2008). This method makes use of medium-to-low quality spectra without needing to fit complex models to individual spectra and computes a mean spectrum for the whole

sample. Given that we have low quality data, we apply this method to our HYPERION QSO sample for the pn spectra only without going through the complication of adding even lower quality data from the different MOS detectors. Using both pn and MOS would require an extensive set of simulations to validate this approach. Hence we test the averaging method using simulations for the pn data only.

For the purpose of all our analysis, we used XSPEC v 12.13.1, a X-ray spectral analysis software. For each source, we unfold the spectrum from the instrumental response to recover the original source spectra. The unfolded spectrum is the original source spectrum prior to detection and is free from instrumental effects of the detector. For each individual spectra, we first perform a de-absorption. To do this we first group the spectra and fit the grouped spectra with a single power law model corrected by photoelectric absorption due to the interstellar medium of our Galaxy. Hence the column density is fixed at the Galactic value for each source position. This model is expressed in XSPEC by the expression `tbabs*zpow` where `zpow` is the power-law model parameterizing the coronal emission and `tbabs`[1] is the photoelectric absorption term which modifies the low energy (typically $\leq$ 2 keV rest-frame) part of the coronal spectrum.

The aim of this first step, was not to find best fit parameters but to use a model suitable to unfold the spectrum without severe bias. We fit each grouped spectra between 0.3 - 7 keV (in the observed frame) which corresponds to rest frame energies $\sim$ 2 to $\sim$ 50 keV, leaving power-law slope and normalization as free parameters. Below 0.3 the instrument is not very sensitive and not well calibrated. Above 7 keV the spectra are severely background-dominated and therefore the uncertainties are high (see Zappacosta et al. 2023). We apply this best fit model to the un-grouped spectrum and keep Γ fixed at the value obtained in the previous step. For each source, we save the model values for the `tbabs*zpow` model once by keeping the Galactic absorption fixed to the nominal value at the position of the source and then again by fixing it to 0, i.e, effectively removing the absorption term. We subtract these model values and convert the counts using the following formula:

[1]https://heasarc.gsfc.nasa.gov/xanadu/xspec/manual/node275.html

$$\Delta C = (M_{abs} - M_{unabs}) \times t_{exp} \times \Delta E \tag{4.1}$$

where ΔC is the difference in counts in the absorbed and deabsorbed spectrum, M_{abs} is the counts of the absorbed spectrum, M_{unabs} is the counts of the deabsorbed spectrum , ΔE is the width of the energy bin and t_{exp} is the cleaned exposure time of observation after removing high background flaring periods. We added the ΔC to the counts in the real spectra file to create a de-absorbed spectra.

We correct the de-absorbed spectrum for redshift, shift the spectrum to the rest frame energies and then unfold the spectrum using the *eufspec* command in XSPEC. The *eufspec* command plots the unfolded spectrum and model in terms of Ef(E) (the energy flux at a given energy) and we plot the spectrum from folded counts to unfolded energy of photon. We now have spectrum in physical units (keV cm^{-2} s^{-1} keV^{-1}) which is free from instrumental effects.

We rescale the unfolded spectra to allow each spectrum to contribute equally to the final averaged spectrum. The simplest way to do is is by normalizing all the spectra to a certain value within a given energy band so that every rescaled spectra has the same flux value within the range where it is rescaled. While selecting the range of energies for rescaling we exclude the region around the Fe Kα line and also the higher energies where the spectrum has low signal to noise ratio due to the decline of the effective area. For this study we have used observed energy range of 1 - 2 keV that roughly corresponds to 7 - 15 keV rest frame energies for the redshift range of our sources. This energy range was selected because the pn detector is most sensitive at the 1 - 2 keV range and we have most counts in that energy range. We calculate the mean flux over the 7 - 15 keV range for each spectra and divided the spectra by this value. The resulting rescaled spectra have roughly the same flux in that energy range.

Each of these individual spectra here has been expressed on a different energy grid because of the different channel sizes at different energies and shifting to rest-frame. To get some uniformity in the errors of the average spectrum across the whole energy band and to have a common energy grid to sum the counts of all the spectra bin by bin, we create a new energy grid for the final averaged rest-frame spectrum. To create the new bins, we first need individual de-absorbed source spectra in counts. These

spectra are only de-absorbed and not rescaled. We correct the spectra for redshift and rebinned the counts to create new energy bins of equal width. We then distributed each rescaled, flux density values for each individual spectrum into the new energy bins in the following way:

$$S'_j = \sum_{i \in j} \frac{S_i \Delta\epsilon_i f_{ij}}{\Delta' \epsilon_j} \tag{4.2}$$

where

$$f_{ij} = \frac{min(\epsilon_{imax}, \epsilon'_{jmax}) - max(\epsilon_{imin}, \epsilon'_{jmin})}{\Delta\epsilon_i} \tag{4.3}$$

where S'_j, $\Delta' \epsilon_j$ and S_i, $\Delta\epsilon_j$ are the flux density values in keV cm^{-2} s^{-1} keV^{-1} and widths in keV of the new and old bins, respectively and f_{ij} represents the fraction of the old bin i that covers the new bin j. Now that we have the rest frame, rescaled and rebinned spectra, we combine them simply using un-weighted standard mean to get the average flux in each new bin ($S_{j,avg}$).

Now we have to calculate the errors corresponding to the fluxes in the new energy bins for each spectrum. For this, we first used the power-law model (`zpow`) on the de-absorbed spectra and saved the model values of the folded and unfolded spectra. We redistributed these model flux values the same way we redistributed the spectra according to Equation 4.2 and 4.3. For each spectrum we calculated the ratio of unfolded model to folded model for each new bin. We then calculated the error in each new bin in counts according to the following formula:

$$\Delta Err_{counts,j} = S'_j \times \frac{M_{unfl,j}}{M_{fl,j}} \times t_{exp} \times \Delta\epsilon_j \tag{4.4}$$

Where $\Delta Err_{counts,j}$ is the error in counts, $M_{unfl,j}$ and $M_{fl,j}$ are the unfolded and folded model flux values and $\Delta\ \epsilon_j$ is the energy width of the new energy grids.

We then use this error in counts to calculate the 1σ Poissonian error bars for the data using the formula (Gehrels, 1986):

$$Error_j = 1 + \sqrt{n + \frac{3}{4}} \tag{4.5}$$

where n = $\Delta Err_{counts,j}$ as calculated before. This error in counts has to be converted into error in terms of flux by using the formula:

$$\Delta Err_{flux,j} = \frac{Error_j}{\frac{M_{unfl,j}}{M_{fl,j}} \times t_{exp} \times \Delta\epsilon_j} \tag{4.6}$$

Where, $\Delta Err_{flux,j}$ is the error of the redistributed flux. Since each spectra has been normalized by dividing them by the flux between 7 - 15 keV range, we have to divide the errors in each spectrum by this value as well. Once we have the rest frame rescaled and rebinned spectra we simply average them using an un-weighted standard mean with the final errors on the averaged spectrum being computed in the following way:

$$Error_{j,avg} = \frac{\sqrt{\Sigma_j^N (\Delta Err_{flux,j})^2}}{N} \tag{4.7}$$

where N is the number of spectra that is being averaged.

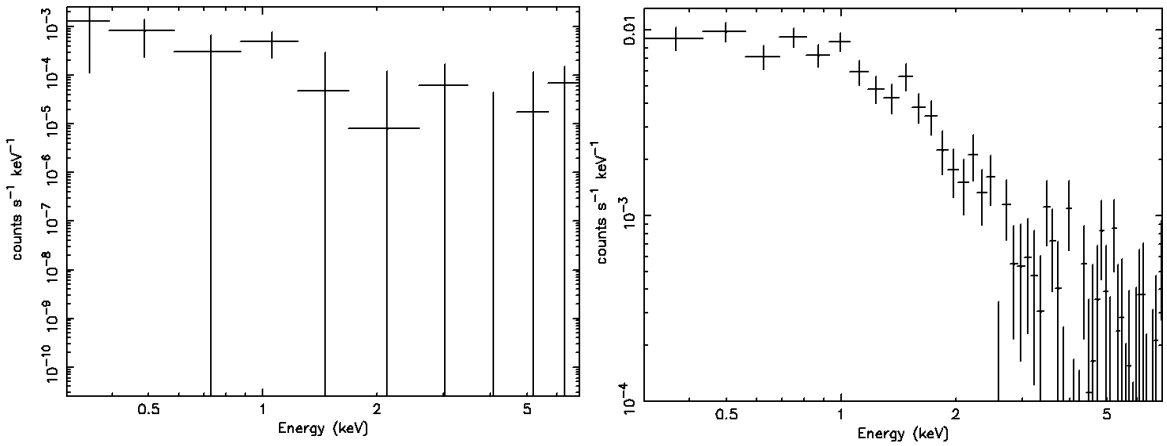

Figure 4.1: (Left) Simulated spectra for $\Gamma = 1.9$ for low counts case in the 0.3 - 7.0 keV range. This simulated spectra has 77 counts in the same energy range and has $z = 7.0$. (Right) Simulated spectra for $\Gamma = 1.9$ for the high counts case in the 0.3 - 7.0 keV range. This simulated spectra has 1007 counts in the same energy range and has $z = 7.0$.

4.3 Testing the Spectral Combination Procedure

To test our averaging method and to distinguish between real spectral features and artifacts from the averaging process, we carried out extensive tests using simulated spectra. The canonical value of Γ obtained for typical local AGN (Piconcelli et al. 2005, Dadina 2008) is 1.8 - 2.0. Here we use the mean value of $\Gamma = 1.9$. Additionally, Zappacosta et al. (2023) obtained $\Gamma \sim 2.4$ for the HYPERION QSOs. So for our simulations we use $\Gamma = 1.9$ and 2.4. We use only `tbabs*zpow` model without intrinsic absorption because these are Type 1 QSOs, so we don't expect them to show significant absorption. Furthermore at high redshift we probe > 2 keV rest-frame energies which are well above the energies for which we could expect some absorption from low column densities ($< 10^{21}$ cm^{-2} expected from Type 1 sources). In our simulations, we refer to cases with ≈ 80 net-counts as **low counts cases** and those with ≈ 1000 net-counts as **high counts cases**. We use the `tbabs*zpow` model and simulate spectra in both high and low counts for the following cases:

- $\Gamma = 1.9$ fixed for the `zpow` model
- $\Gamma = 2.4$ fixed for the `zpow` model
- Γ fixed for the `zpow` model at a random value drawn from a Gaussian distribution

with mean = 1.9 and $\sigma = 0.2$

- Γ fixed for the `zpow` model at a random value drawn from a Gaussian distribution with mean = 2.4 and $\sigma = 0.2$.

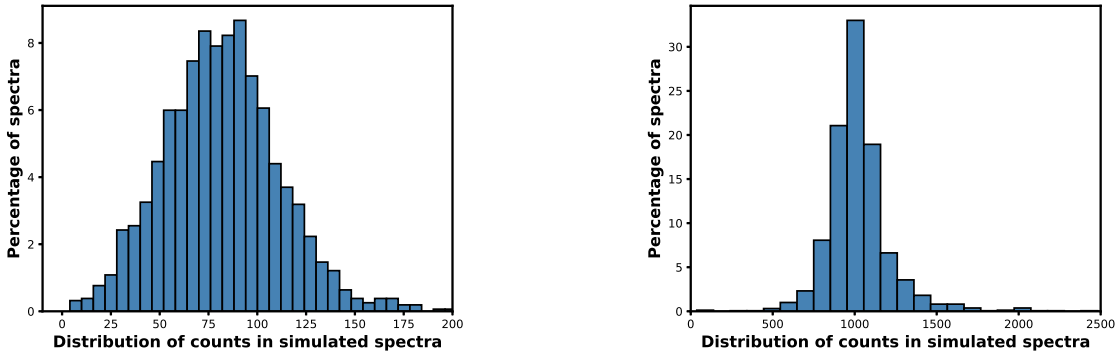

(a) Case of low counts (b) Case of high counts

Figure 4.2: Distribution of counts of the simulated spectra for Γ fixed at 1.9 $\pm$ 0.2

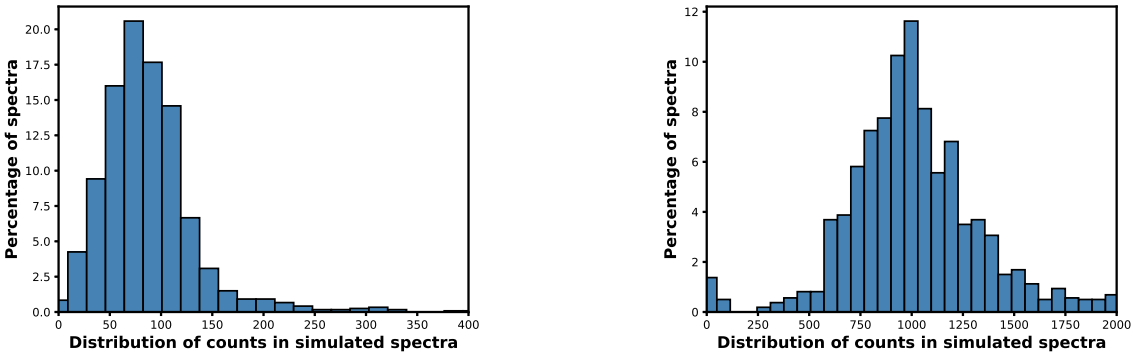

(a) Case of low counts (b) Case of high counts

Figure 4.3: Distribution of counts of the simulated spectra for Γ fixed a 2.4 $\pm$ 0.2

We simulated the case of high counts in the 0.3 - 7.0 keV energy range because we want to check at high confidence that the procedure to combine spectra can recover the correct input values. We simulate low count cases to understand if the procedure works with limited quality spectral data as $\approx$ 80 is the approximate number of 0.3 - 7 keV net-counts reported in each final spectrum of QSOs in the HYPERION sample.

For these simulations we kept the exposure time at 80 ks and Galactic absorption was fixed at $5 \times 10^{20}\mathrm{cm}^{-2}$. We simulated each individual source and background spectrum

using the XSPEC command *fakeit*. The *fakeit* command uses an input, rmf, arf and background files from a real observation. Since we are simulating spectra for the pn detector, we have used the appropriate pn files for the simulations.

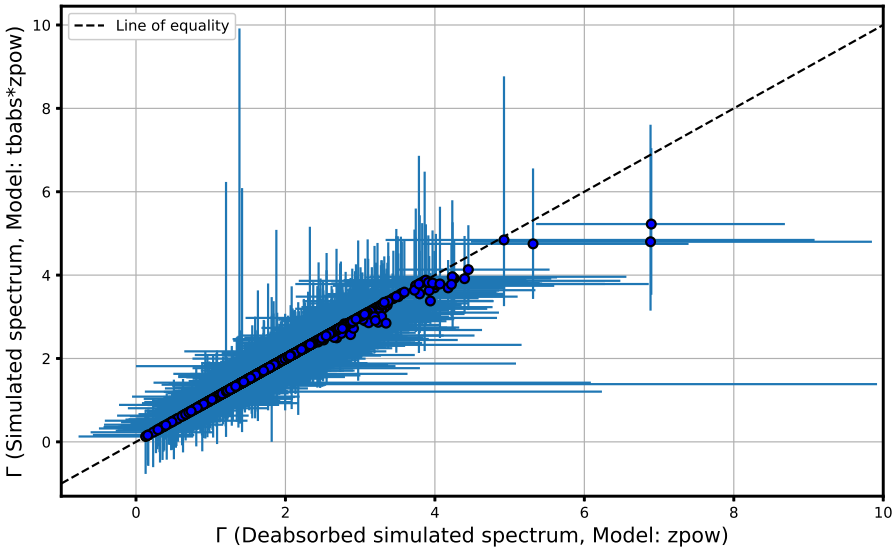

Figure 4.4: Comparison of best fit gamma values for the case of $\Gamma = 1.9 \pm 0.2$ and low counts before and after de-absorption. The x-axis shows the best fit gamma values of the de-absorbed spectrum using power-law model (`zpow`) while the y-axis shows the best fit gamma values of the spectrum before deabsorption using `tbabs*zpow` model.

For each case listed above we generated 100 sets of fake spectra. For each set we simulate 16 source spectra each with its own redshift which we chose to have uniformly distributed between 6 and 7.5 in steps of 0.1. Therefore we simulate 16 spectra, similar to the number of HYPERION sources implying that for each case we have 1600 spectra. Figure 4.1 shows examples of 2 such simulated spectra. Even though we aim at simulating spectra with low and high counts, because of small number statistics (especially for 80 counts cases) and the background subtraction, the resulting number of counts are not exactly 80 or 1000 counts but vary somewhat. Figures 4.2 and 4.3 show the distribution of counts in the 0.3 - 7 keV energy range of simulated spectra for Γ fixed at a value drawn from a Gaussian distribution of mean = 1.9 and 2.4 with standard deviation of 0.2. For the cases with low counts in the 0.3 - 7 keV energy range, we binned the data with a minimum of 5 counts per bin while for the case of high counts, we binned it with a minimum of 10 counts per bin. We then apply the exact same

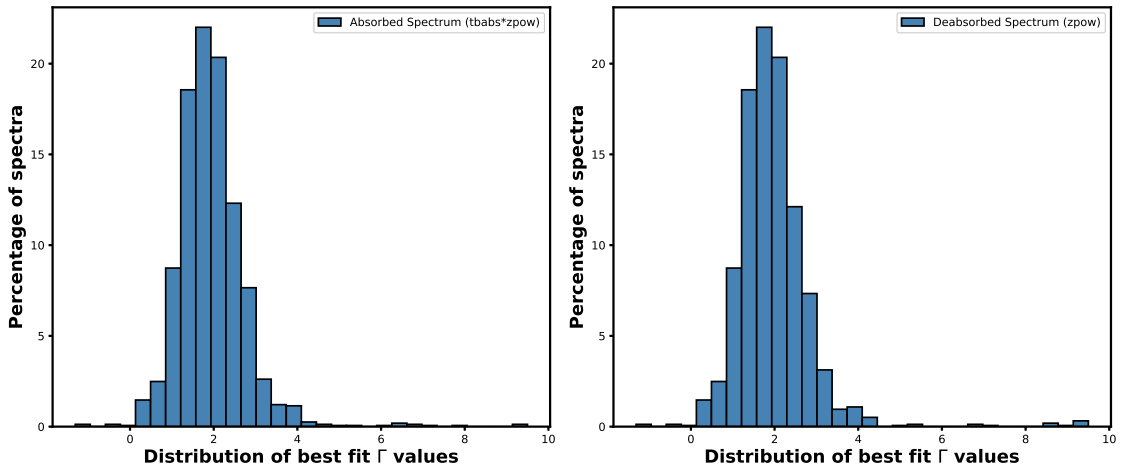

Figure 4.5: Histogram of best fit Γ values of absorbed and deabsorbed spectrum for for the case of Γ fixed at 1.9 ± 0.2.

averaging process as the real spectra.

To check the effects of de-absorbing the spectra we compare the best fit Γ for the absorbed and de-absorbed spectra. Figure 4.4 show a comparison between the best fit gamma values and 1 σ errors of the simulated spectra before and after de-absorption. The y-axis shows the best fit gamma values of the spectrum before de-absorption using `tbabs*zpow` model while the x-axis shows the best fit gamma values of the de-absorbed spectrum using power-law model (`zpow`) for the case of Γ fixed at 1.9 ± 0.2. Figure 4.5 shows the same comparison as histograms. We see here that de-absorption of the spectrum doesn't cause any change in Γ, i.e, the slope of the power-law spectrum.

Examples of the unfolded, de-absorbed, redshift corrected spectra are shown in Figure 4.7. To show the effect of normalization, we show in Figure 4.6 one simulation set from the the case where we considered $\Gamma = 1.9 \pm 0.2$ with low net counts. We have shown the 16 deabsorbed spectrum which has been binned for visualization and also the corresponding normalized, unfolded spectra. For this set of simulation the average value of simulated $\Gamma = 1.83$ and the best fit Γ of the average spectrum was $\Gamma = 1.99^{+0.28}_{-0.25}$.

At all stages of the averaging process, except for the spectral fitting of the average spectrum, we use Cash statistic (Cash, 1979) with direct background subtraction (W-stat in XSPEC; Wachter et al. 1979). For the spectral fitting of the final average spectrum we use χ^2 statistics.

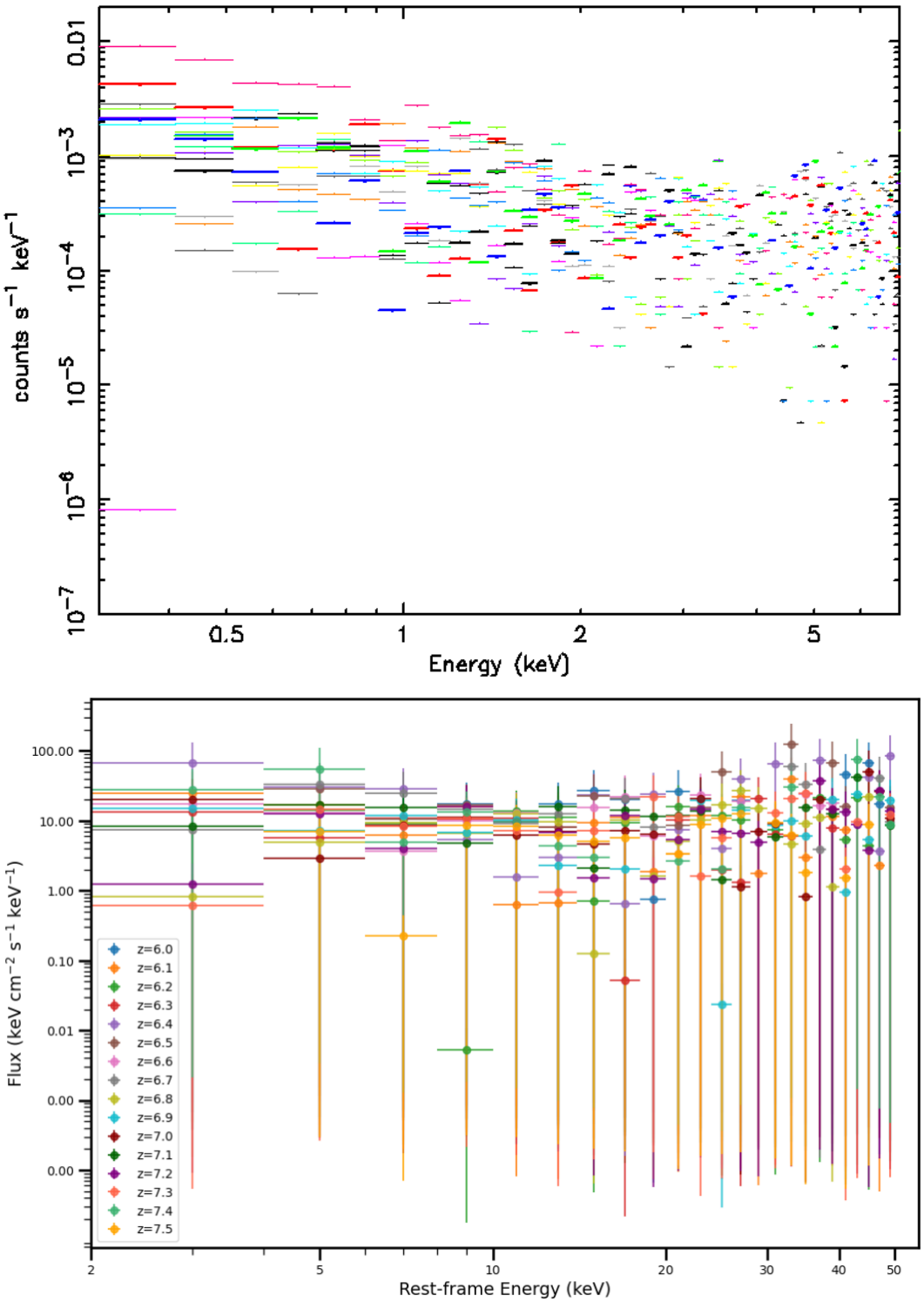

Figure 4.6: One simulation set from the the case where we considered $\Gamma = 1.9 \pm 0.2$ with low net counts. We have shown the 16 deabsorbed spectrum which has been binned for visualization (top) and also the corresponding normalized, unfolded spectra (bottom). For the plot at the top we did not plot the y error bars because these values go down to zero and also make the plot difficult to visualize.

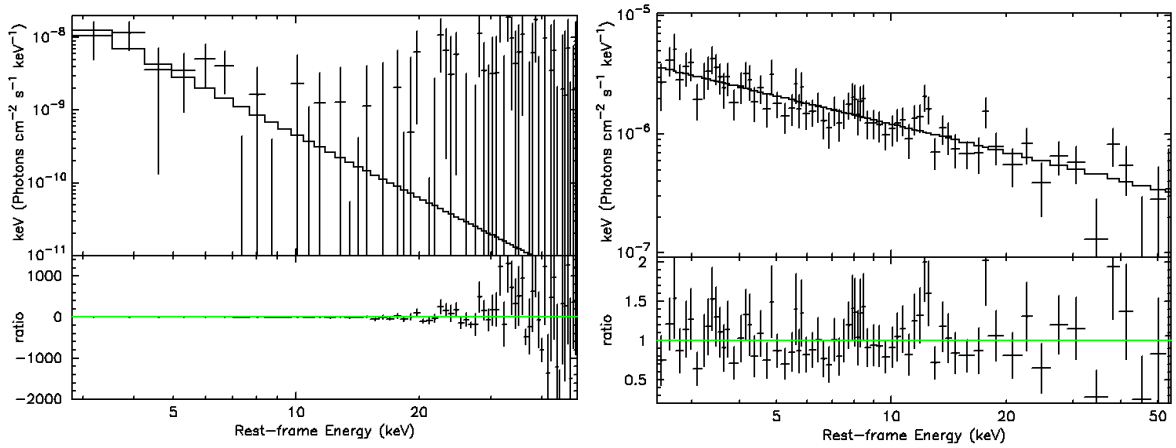

Figure 4.7: (Left) Unfolded, de-absorbed, redshift corrected spectra for simulation considering $\Gamma = 1.9$ and low counts in the 0.3 - 7.0 keV range. This simulated spectra has 77 counts in the same energy range and has $z = 7.0$. (Right) Unfolded, de-absorbed, redshift corrected spectra for simulation considering $\Gamma = 1.9$ and high counts in the 0.3 - 7.0 keV range. This simulated spectra has 1007 counts in the same energy range and has $z = 7.0$.

In Figure 4.8 we show examples from one simulation set from the the case where we considered $\Gamma = 1.9 \pm 0.2$ with low net counts. We show a single spectrum of $z = 6.8$ and the average spectrum from that set. For this set of simulation the best fit Γ value from the average spectrum is $\Gamma = 1.99^{+0.28}_{-0.25}$ with $\chi^2/\mathrm{dof} = 17.25/22$. The difference in the quality of data between the single spectrum and the average spectrum can be seen quite well.

For the case of power-law, we know that, number of photons or counts of a given energy E, N(E) $\propto$ E$^{-\Gamma}$ and in the unfolded spectrum we are plotting E*N(E), i.e., E*E$^{-\Gamma}$ = E$^{1-\Gamma}$ = E$^{\Gamma u}$. So $\Gamma = \Gamma_u + 1$. Figure 4.9 shows the histogram of the best fit Γ values of the average spectrum of simulated sets of low counts for the different different cases of simulation conditions while Figure 4.10 shows the same for the high counts cases. We see that we recover the input Γ value quite well after the spectra had been averaged. Since for the case of $\Gamma = 1.9/2.4 \pm 0.2$ we simulate spectra with a range of Γ values, it is useful to show a comparison of the average Γ value of each set and the best fit Γ value obtained from a simple power-law model fit on the average spectrum of each set. We show one such example in Figure 4.11.

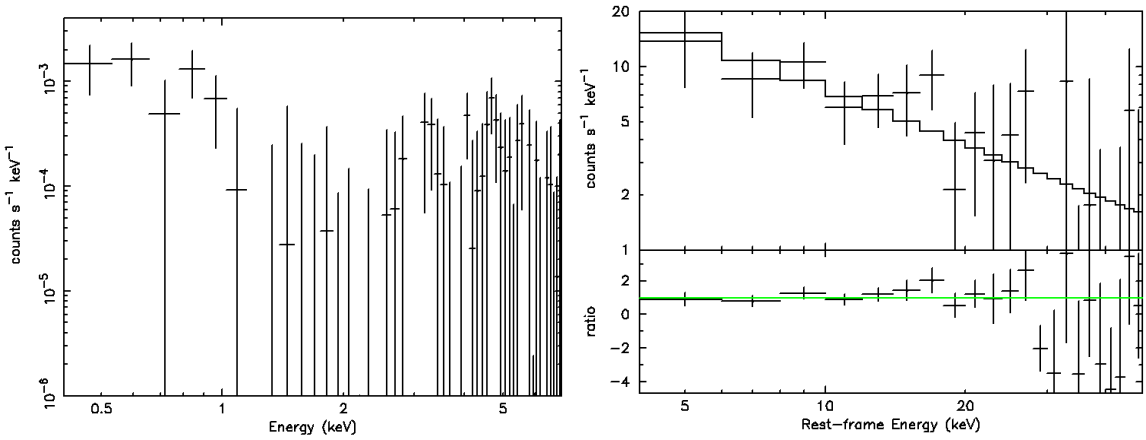

Figure 4.8: These show the comparison between a single spectra (left) and an average spectrum created from 16 such spectra (right). We can see that the single spectrum is of lower quality with larger error bars while the average spectrum has lower error bars and is of better quality.

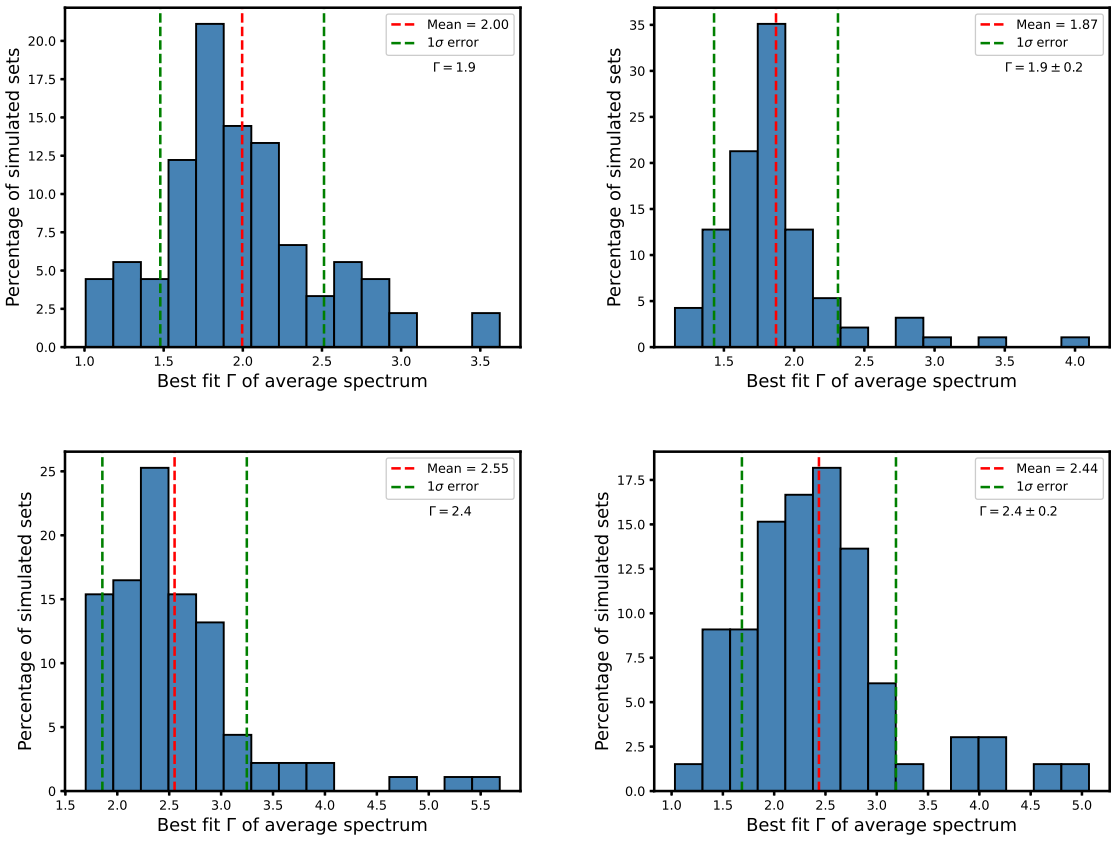

Figure 4.9: Histogram of best fit Γ values of average spectrum of simulations with low counts in the 0.3 - 7.0 keV range in individual spectrum. $\Gamma = 1.9$ and $\Gamma = 1.9 \pm 0.2$ (top left and right), $\Gamma = 2.4$ and $\Gamma = 2.4 \pm 0.2$ (bottom left and right). These Γ values have been reported after adding 1 to them, i.e., the reported values are Γ and not Γ_u.

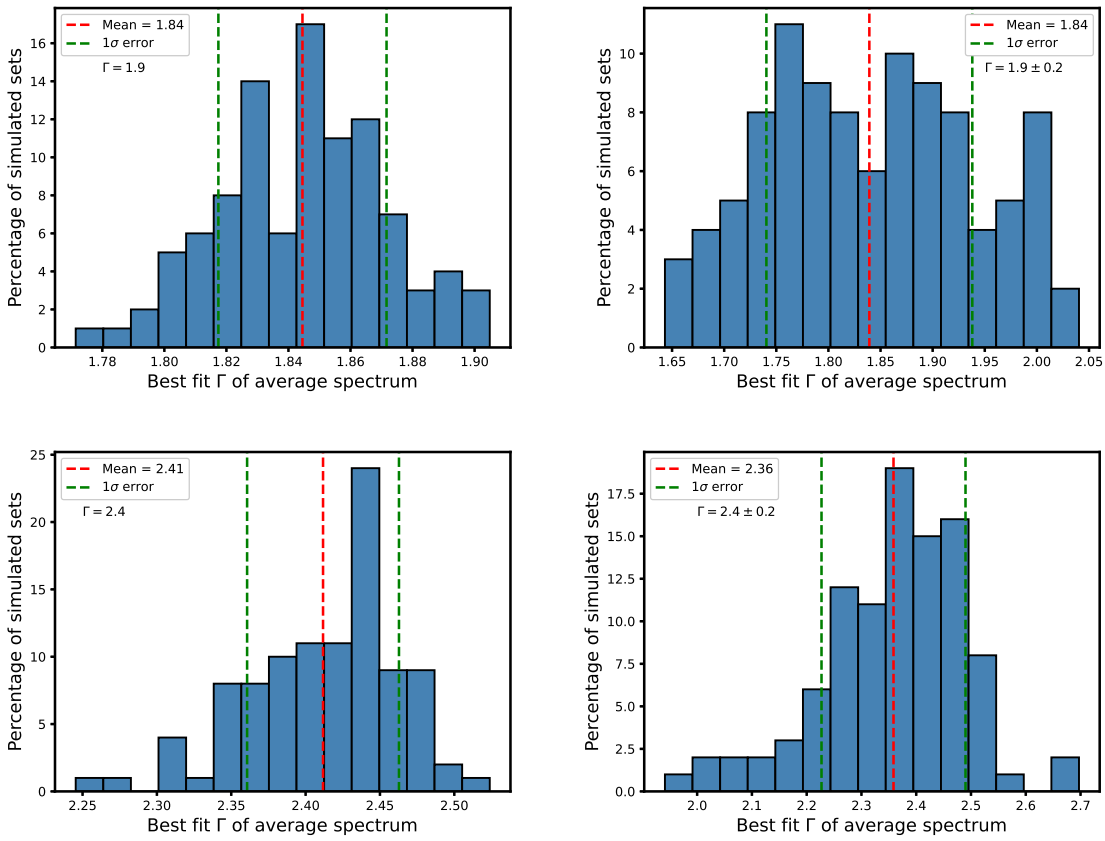

Figure 4.10: Histogram of best fit Γ values of average spectrum of simulations with high counts in the 0.3 - 7.0 keV range in individual spectrum. $\Gamma = 1.9$ and $\Gamma = 1.9 \pm 0.2$ (top left and right), $\Gamma = 2.4$ and $\Gamma = 2.4 \pm 0.2$ (bottom left and right.) These Γ values have been reported after adding 1 to them, i.e., the reported values are Γ and not Γ_u.

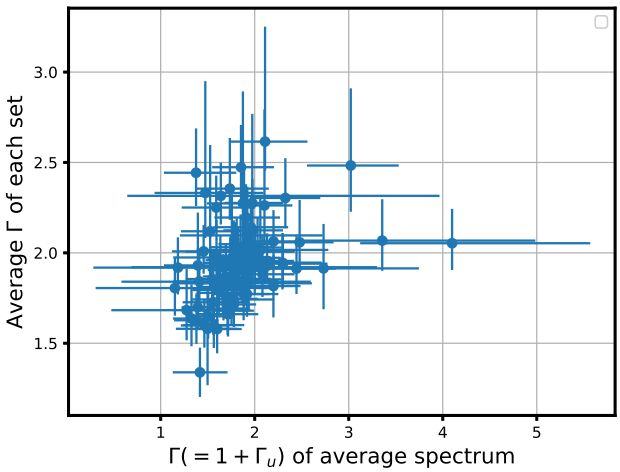

Figure 4.11: Comparison of the average Γ value of each set and the best fit Γ value obtained from a simple power-law model fit on the average spectrum of each set for the case of $\Gamma = 1.9 \pm 0.2$ with low net counts.

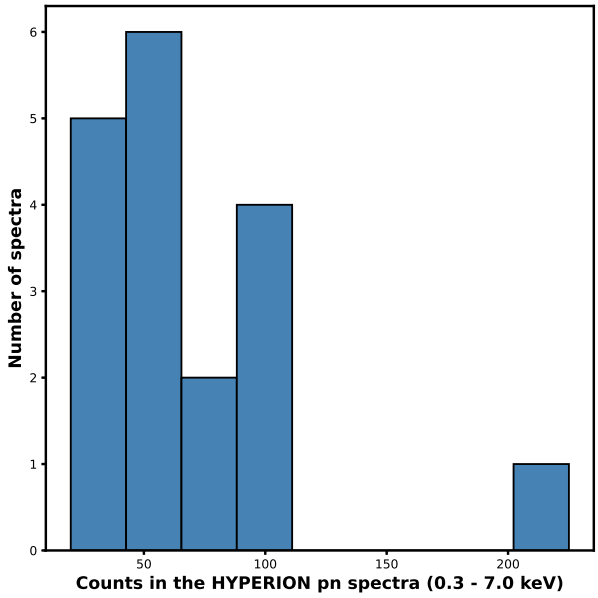

Figure 4.12: Distribution of counts of the 18 pn HYPERION spectra.

4.4 Averaging the HYPERION pn Spectra

The HYPERION Heritage program, XMM-HYPERION consist of 16 HYPERION target QSOs while the HYPERION sample consist of 18 QSOs. Two X-ray observations of HYPERION targets are from the *XMM-Newton* archive and are not part of the XMM-HYPERION. The observations within XMM-HYPERION are 26 because few targets (6) have more than one observation (see Table 4.1). We combine them using the *addascaspec* script This script can be used to combine two or more spectral files for the same source, taken with the same detector at different time periods. We combine multiple observations of the same source because we want to start from a single summed spectral file for each source. Table 4.1 shows the Galactic absorption for each source, the observation IDs and the net counts in the 0.3 - 7.0 keV energy range and the cleaned exposure time. The net count implies the background subtracted counts, i.e, (source-background) count and cleaned exposure time refers to the total time of high-quality data available for analysis after removing high background flaring periods.

We bin the pn spectra with minimum 3 counts per bin and fit using `tbabs*pow` model. Table 4.2 show the best fit parameters of the 18 HYPERION QSO spectra and

Figure 4.12 shows the distribution of counts of the HYPERION sample. Figures 4.15 shows their 0.3 - 7.0 keV spectra and best fit model. Figures 4.16 shows the 0.3 - 7.0 keV deabsorbed, de-redshifted spectra and best fit model. All spectra has been further binned for visualization and reported in their rest-frame energy. The comparison of best fit gamma values of the absorbed and deabsorbed spectra can be seen in Figure 4.13. We see here that there is a systematic shift. The process of deabsorbing the spectrum, in this case, tends to create spectra with lower Γ. The dashed line shows the line of equality while the red line is the best fit line on the data with slope equal to the slope of the dashed line. The intercept of the red line on the y-axis show the systematic shift in the Γ value of the deabsorbed spectrum. Here we see this shift to be = 0.28. We will take into consideration this systematic value to estimate the best fit Γ values of the average spectrum. Figure 4.17 shows the unfolded pn spectra. We performed the averaging method exactly as mentioned in Section 4.1. Using all the 18 HYPERION QSOs, resulted in lower quality spectrum than expected. Figure 4.14 shows the average 0.3 - 7.0 keV spectrum created with all the 18 HYPERION QSOs and we can see that below 10 keV rest-frame energy which corresponds $\sim$ 1.5 keV observed energy range we see no flux.

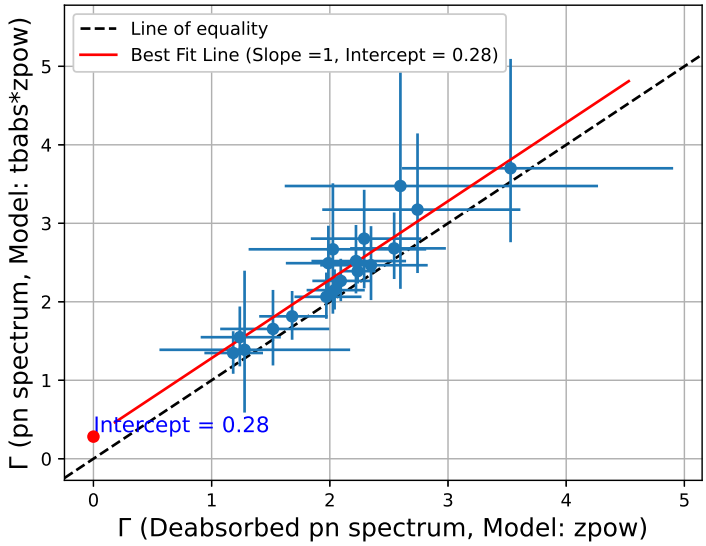

Figure 4.13: Comparison of best fit Γ values of absorbed and de-absorbed spectrum of the HYPERION sample

This is unexpected because the pn detector on *XMM-Newton* is most sensitive between 1.0 - 2.0 keV energy range. The source J0252 has very low net-counts $\sim$ 19 and it is possible that due to very low-net counts we obtained bad quality average spectrum. The same applies in low net-counts spectra of other sources. Hence, we chose to not include sources with net-counts < 40 while creating the average spectrum. We also removed spectrum with too many counts, i.e, J0100 which has 225 counts which can significantly impact the final average spectrum. This resulted in us using 13 sources to create the average spectrum while discarding J0050, J011, J0252 and J0083 and J0100.

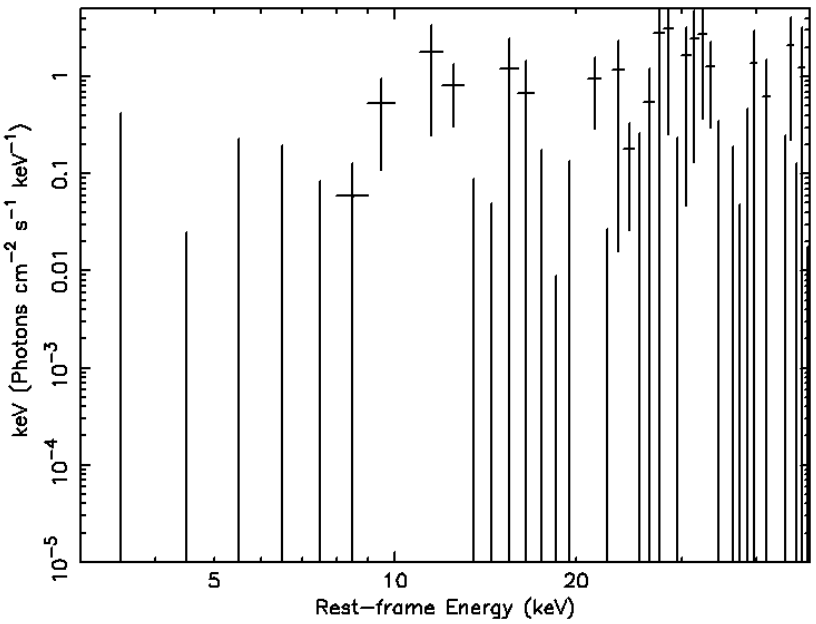

Figure 4.14: Average spectrum created using all 18 HYPERION QSOs

Source	N_H (cm^{-2})	Obs ID	Net counts (s) (0.3 - 7keV)	Cleaned exposure time (s)
J029	1.38×10^{20}	0884992901	52	55220
J0050	5.59×10^{20}	0884992601	36	26210
J025	2.45×10^{20}	0886221401	80	43540
J0100	6.21×10^{20}	0790180701	225	41080
J083	6.93×10^{20}	0884992401	47	51900
J1148	1.62×10^{20}	0886220301	107	55940
J011	6.7×10^{20}	0884992101	20	46230
		0886220201	15	49110
J0224	1.61×10^{20}	0824400301	70	14920
J036	6.26×10^{20}	0884992001	15	47130
		0884994101	55	62580
J231	1.14×10^{21}	0884991701	5	68810
		0886210801	38	51480
		0886210901	17	31260
J0244	2.41×10^{20}	0884991501	92	67410
J0411	4.62×10^{20}	0886210301	88	48560
J0020	1.18×10^{20}	0884991101	27	37410
		0886210201	15	36630
J0252	4.06×10^{20}	0886200901	9	67720
		0886201001	11	351140
J0038	1.7×10^{20}	0884990701	12	57670
		0886200701	25	48070
J1120	4.45×10^{20}	0884990401	50	36590
J1007	2.21×10^{20}	0886201201	46	54960
J1342	1.82×10^{20}	0884990101	47	60340
		0884993801	48	46360

Table 4.1: HYPERION QSO sample and properties of the pn spectrum. This table shows the shortened names of the sources, along with the galactic absorption of X-ray along line of sight, the observation ID, net counts in the 0.3 - 7.0 keV energy range and the cleaned exposure time of each observation.

Source	W-stat/dof	Net counts (0.3-7.0 keV)	Γ (0.3-7.0 keV)	$F_{2-10keV}$ 10^{-16}erg s^{-1} cm^{-2}	$L_{2-10keV}$ 10^{45}erg s^{-1}	Exposure (s)
J029	87.53/66	52	$1.39^{+1.01}_{-0.80}$	$13.98^{+5.95}_{-27.20}$	< 0.34	55220
J0050	36.08/36	36	$3.47^{+2.03}_{-1.31}$	<2.03	$1.06^{+0.29}_{-0.74}$	26210
J025	72.46/69	80	$1.81^{+0.33}_{-0.30}$	$39.83^{+9.28}_{-20.88}$	$1.13^{+0.10}_{-0.48}$	43540
J0100	80.43/101	225	$2.39^{+0.16}_{-0.16}$	$52.91^{+11.89}_{-12.65}$	$3.47^{+0.10}_{-0.68}$	41080
J083	79.64/64	47	$1.55^{+0.39}_{-0.37}$	< 37.36	$6.10^{+0.19}_{-0.13}$	51900
J1148	87.67/91	107	$2.15^{+0.26}_{-0.25}$	$24.80^{+5.22}_{-13.55}$	$1.48^{+0.10}_{-0.43}$	55940
J011	126.28/101	31	$2.67^{+0.84}_{-0.82}$	<2.81	$1.61^{+0.06}_{-0.08}$	95330
J0224	44.55/39	70	$2.06^{+0.31}_{-0.28}$	$62.88^{+16.13}_{-38.50}$	$3.31^{+0.15}_{-1.51}$	14920
J036	112.08/112	65	$2.49^{+0.48}_{-0.43}$	$6.24^{+1.88}_{-4.68}$	$5.19^{+0.23}_{-2.83}$	110700
J231	168.79/191	60	$2.80^{+0.62}_{-0.63}$	<3.79	< 0.24	14990
J0244	62.81/61	92	$2.27^{+0.28}_{-0.26}$	$16.75^{+3.98}_{-7.84}$	$1.32^{+0.03}_{-0.4}$	67410
J0411	64.12/82	88	$1.35^{+0.28}_{-0.26}$	$77.91^{+11.09}_{-54.53}$	$10.67^{+0.19}_{-0.19}$	48560
J0020	37.39/44	42	$2.46^{+0.50}_{-0.44}$	< 5.15	$0.69^{+0.09}_{-0.64}$	74040
J0252	109.55/88	19	$3.17^{+0.97}_{-0.81}$	<0.77	< 0.37	102800
J0038	117.90/111	39	$3.70^{+1.40}_{-0.94}$	<0.36	< 0.59	105700
J1120	38.29/49	50	$2.52^{+0.46}_{-0.41}$	$11.65^{+2.38}_{-10.67}$	$1.50^{+0.05}_{-0.72}$	36590
J1007	59.08/59	46	$1.65^{+0.49}_{-0.46}$	<21.20	< 0.61	54960
J1342	133.51/149	92	$2.68^{+0.46}_{-0.39}$	$5.18^{+1.29}_{-3.90}$	$1.36^{+0.06}_{-0.93}$	106700

Table 4.2: Best-fit parameters from the X-ray spectral analysis of the pn data. Spectra of sources that have multiple observations were combined using *addascaspec* script that can be used to add spectra of the same source taken at different times but with the same detector. We have in this table, source name, best-fit statistics and degree of freedom, net counts in each source, best fit Γ, flux and luminosity of the sources in 2 - 10 keV and the exposure of the observations in seconds.

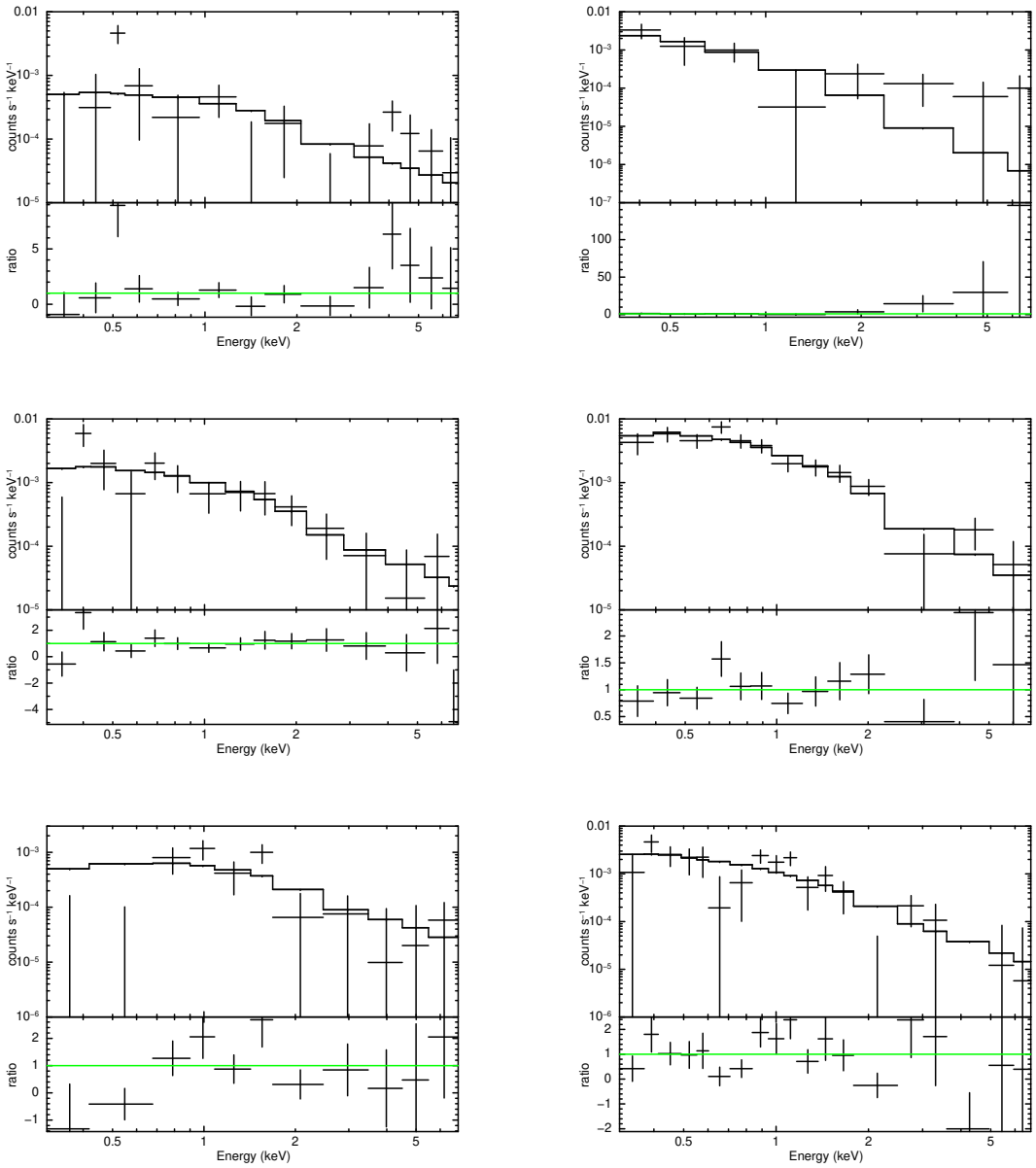

Figure 4.15: Spectra and best-fit model of ATLAS J029-36, CFHQS J0050+3445 (top left and right), ATLAS J025-33, SDSS J0100+2802 (middle left and right), PSO J083.8+11.8 and SDSS J1148+5251 (bottom left and right). Sources are ordered by increasing redshifts. The ratio on the bottom panel is the data divided by the folded model.

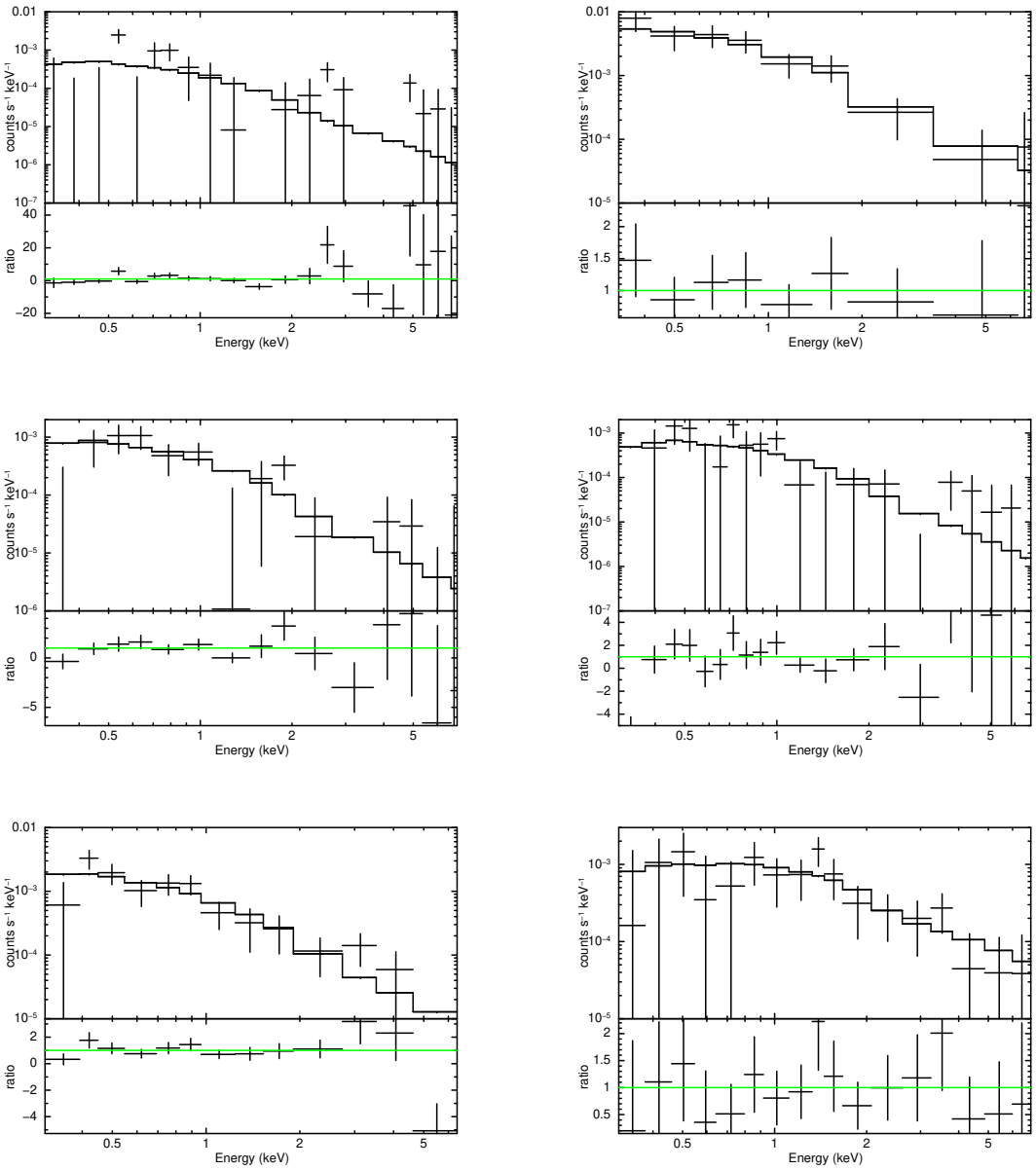

Figure 4.15: Spectra and best-fit model of PSO J011+09, VDES J0224-4711 (top left and right), PSO J036.5+03.0, PSO J231.6-20.8 (middle left and right), VDES J0244-5008 and VHS J0411-0907 (bottom left and right). Sources are ordered by increasing redshifts. The ratio on the bottom panel is the data divided by the folded model.

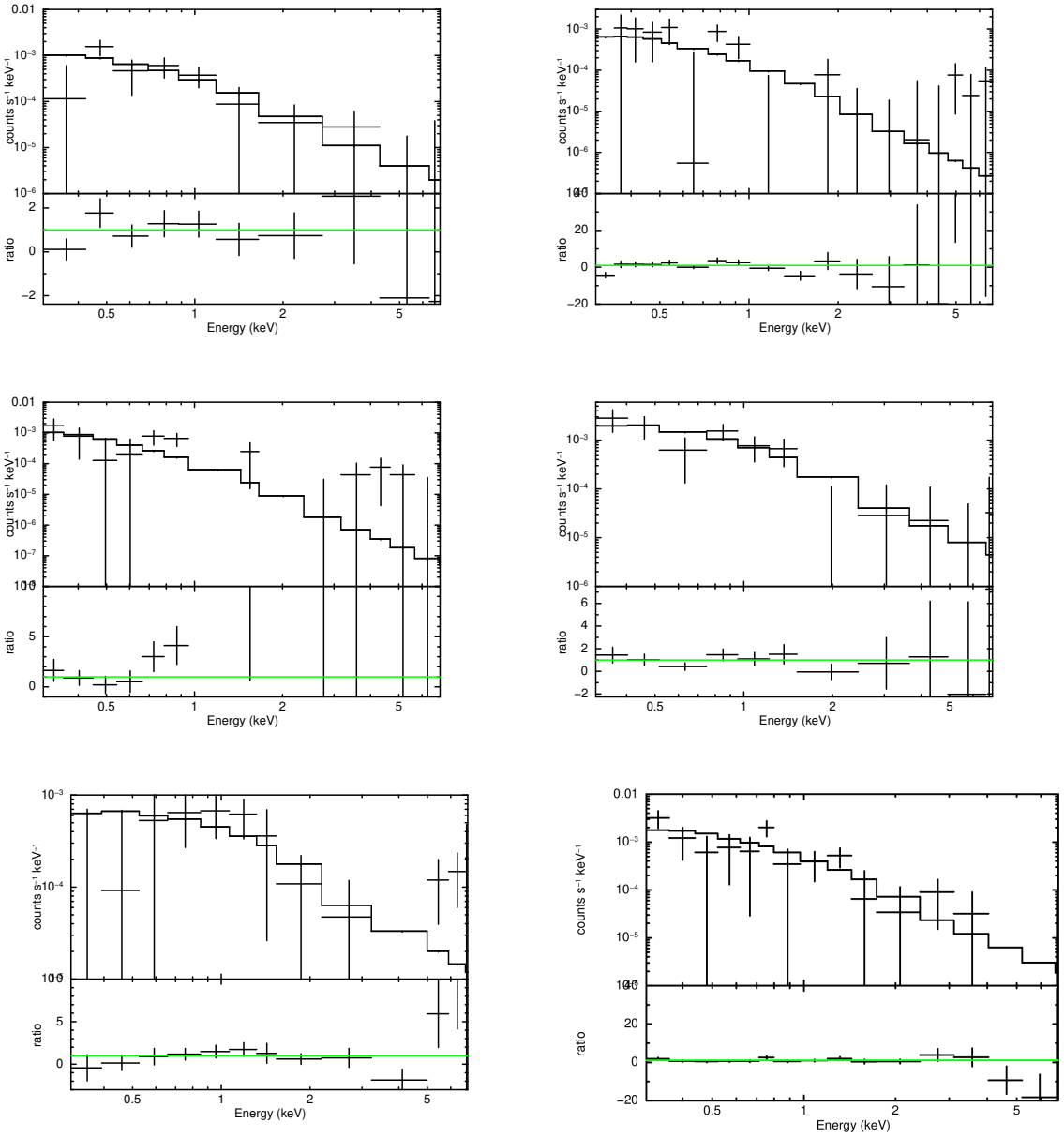

Figure 4.15: Spectra and best-fit model of VDES J0020-3653, DES J0252-0503 (top left and right), DELS J0038-1527, ULAS J1120+0641 (middle left and right), J1007+2115 and ULAS J1342+0928 (bottom left and right). Sources are ordered by increasing redshifts. The ratio on the bottom panel is the data divided by the folded model.

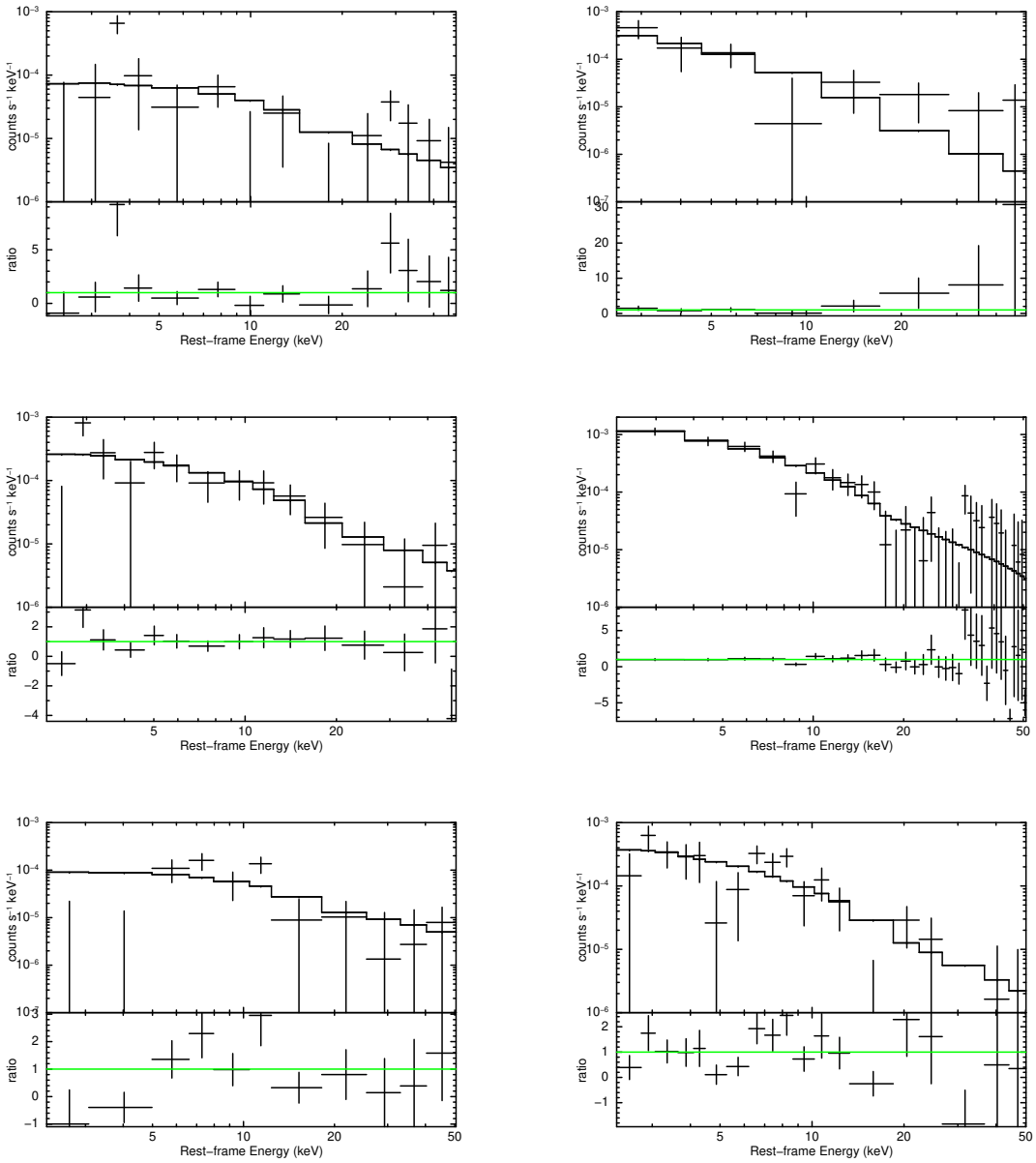

Figure 4.16: Deabsorbed and de-redshifted spectra and best-fit model of ATLAS J029-36, CFHQS J0050+3445 (top left and right), ATLAS J025-33, SDSS J0100+2802 (middle left and right), PSO J083.8+11.8 and SDSS J1148+5251 (bottom left and right). Sources are ordered by increasing redshifts. The ratio on the bottom panel is the data divided by the folded model.

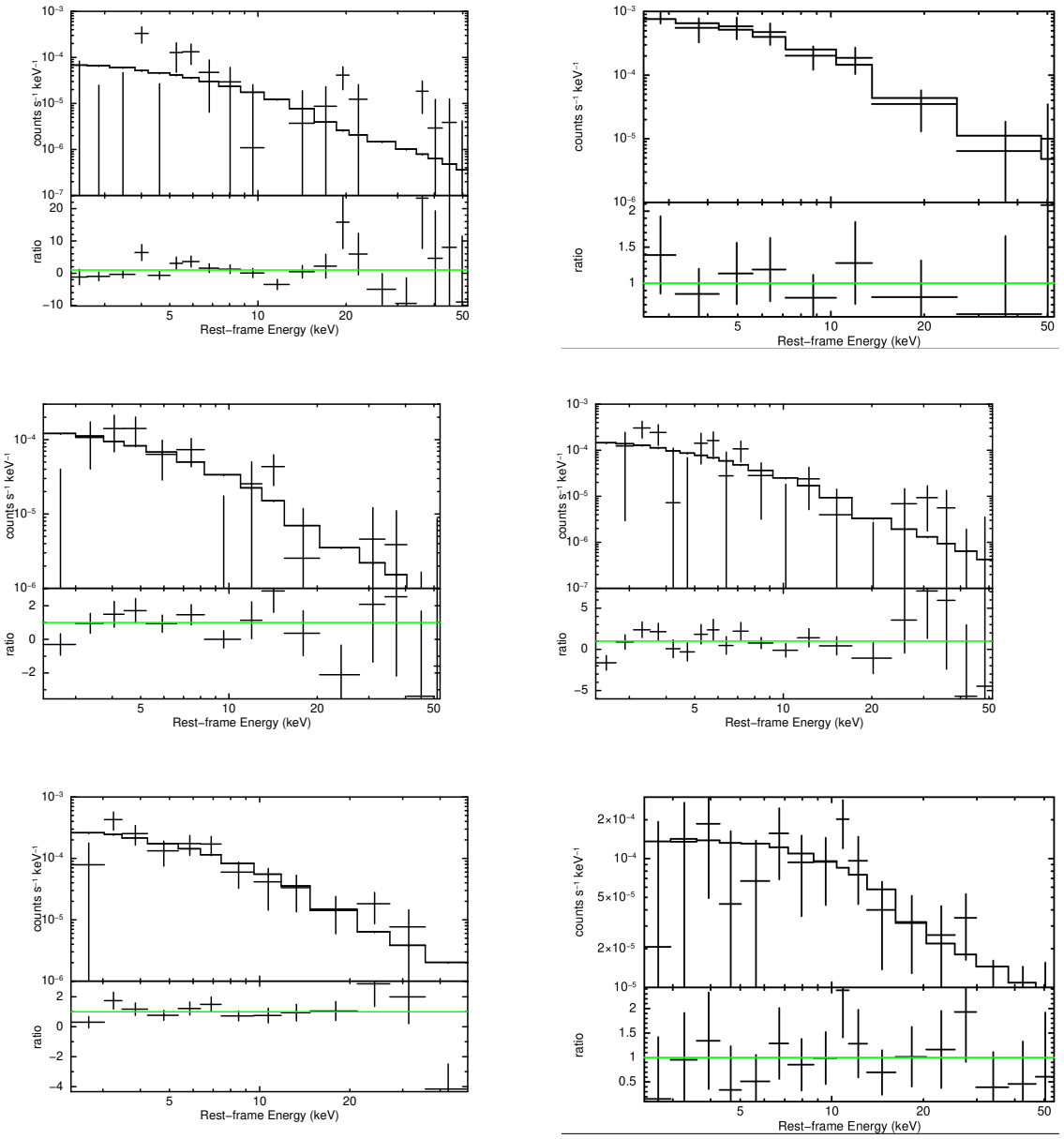

Figure 4.16: Deabsorbed and de-redshifted spectra and best-fit model of PSO J011+09, VDES J0224-4711 (top left and right), PSO J036.5+03.0, PSO J231.6-20.8 (middle left and right), VDES J0244-5008 and VHS J0411-0907 (bottom left and right). Sources are ordered by increasing redshifts. The ratio on the bottom panel is the data divided by the folded model.

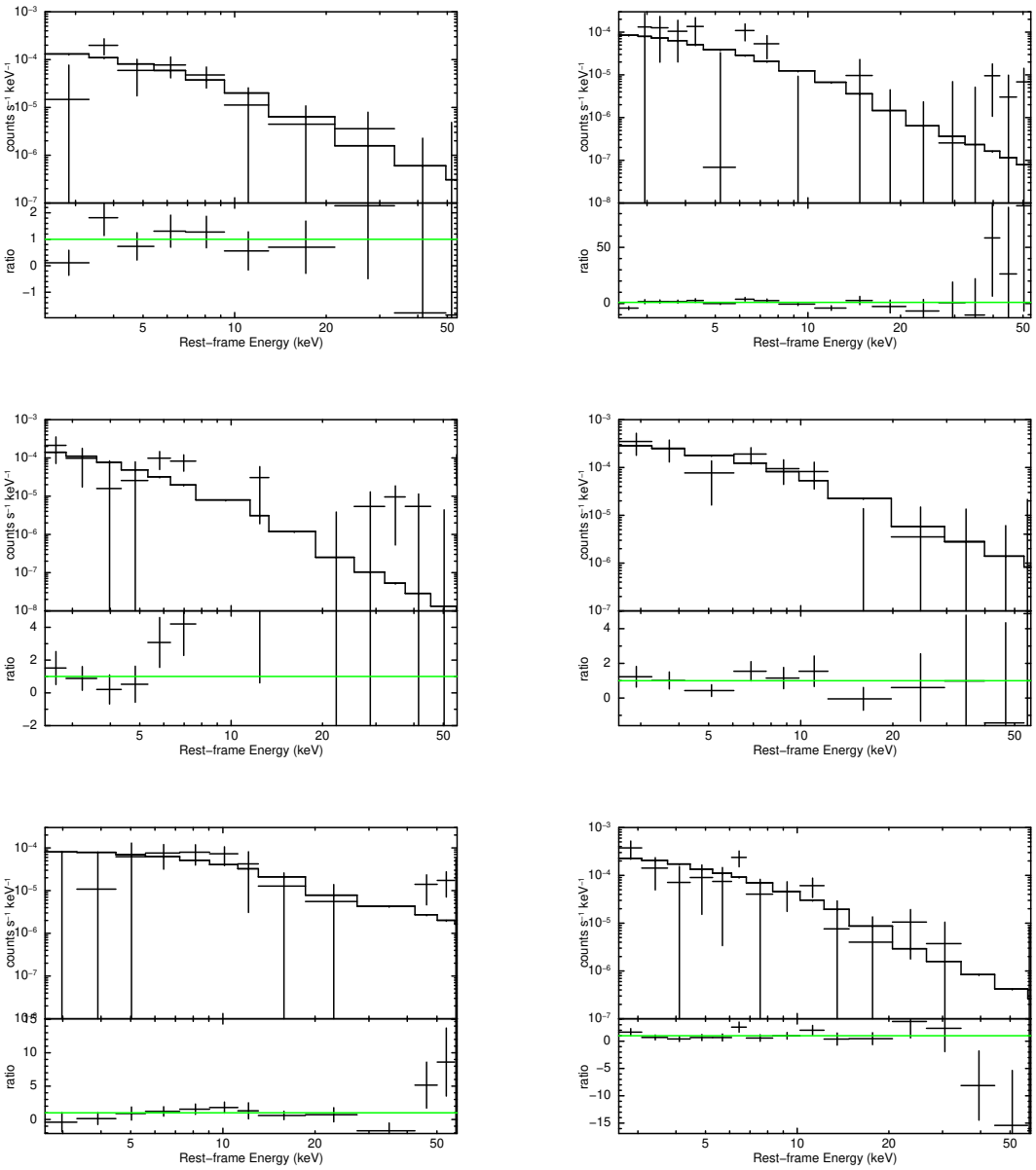

Figure 4.16: Deabsorbed and de-redshifted spectra and best-fit model of VDES J0020-3653, DES J0252-0503 (top left and right), DELS J0038-1527, ULAS J1120+0641 (middle left and right), J1007+2115 and ULAS J1342+0928 (bottom left and right). Sources are ordered by increasing redshifts. The ratio on the bottom panel is the data divided by the folded model.

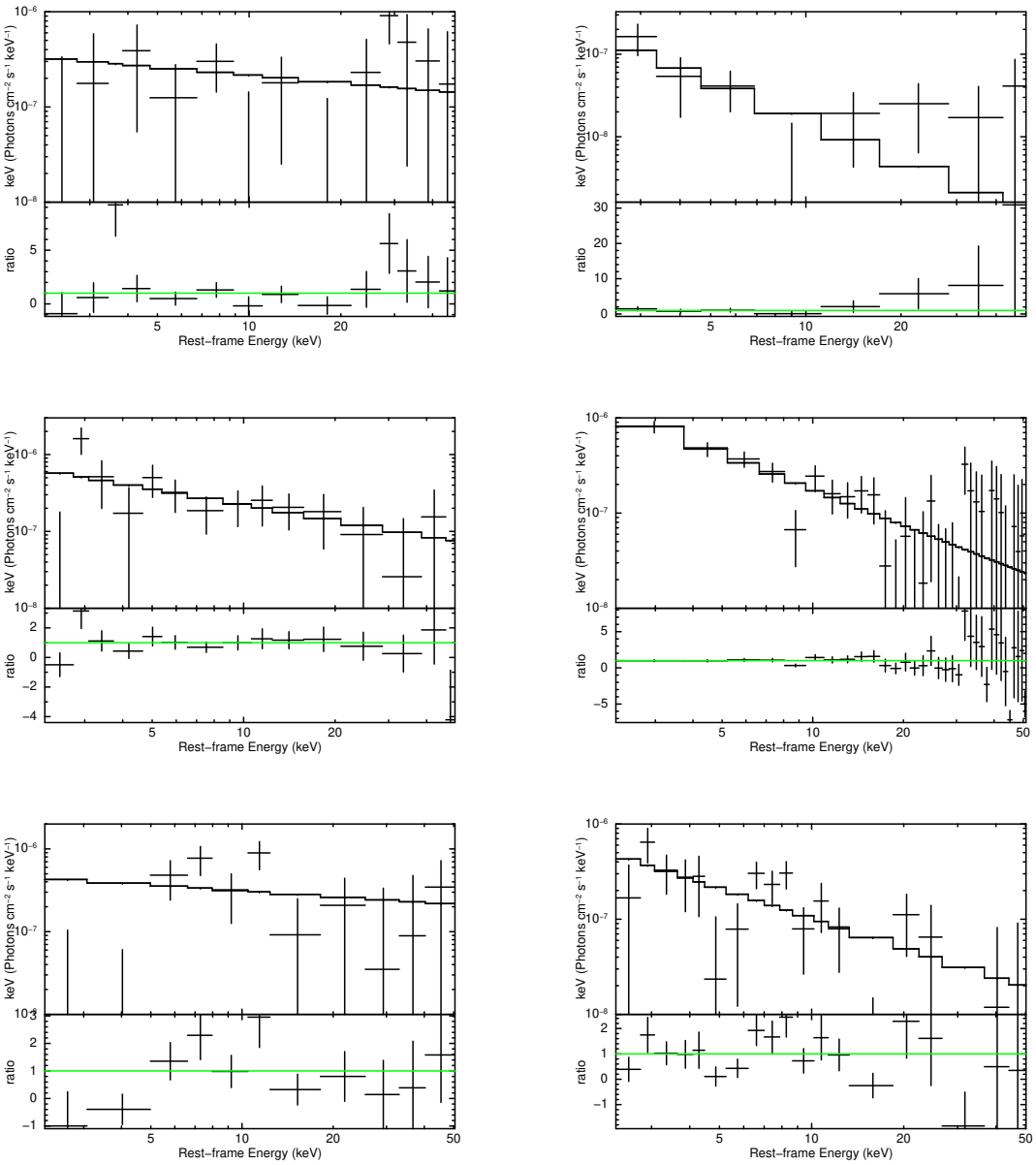

Figure 4.17: Unfolded, deabsorbed and de-redshifted spectra and model of ATLAS J029-36, CFHQS J0050+3445 (top left and right), ATLAS J025-33, SDSS J0100+2802 (middle left and right), PSO J083.8+11.8 and SDSS J1148+5251 (bottom left and right). Sources are ordered by increasing redshifts. The ratio on the bottom panel is the data divided by the folded model.

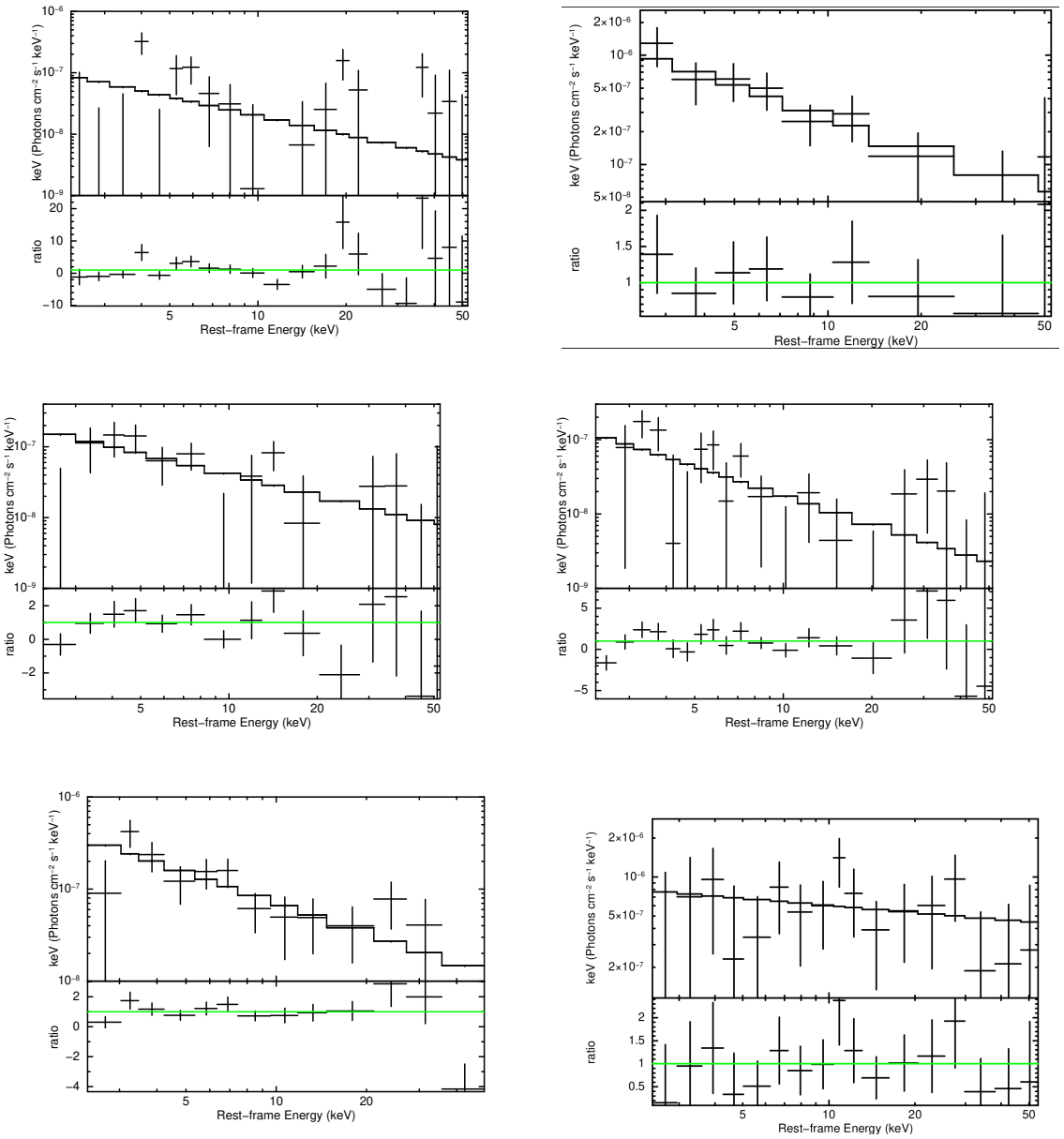

Figure 4.17: Unfolded, deabsorbed and de-redshifted spectra and model of PSO J011+09, VDES J0224-4711 (top left and right), PSO J036.5+03.0, PSO J231.6-20.8 (middle left and right), VDES J0244-5008 and VHS J0411-0907 (bottom left and right). Sources are ordered by increasing redshifts. The ratio on the bottom panel is the data divided by the folded model.

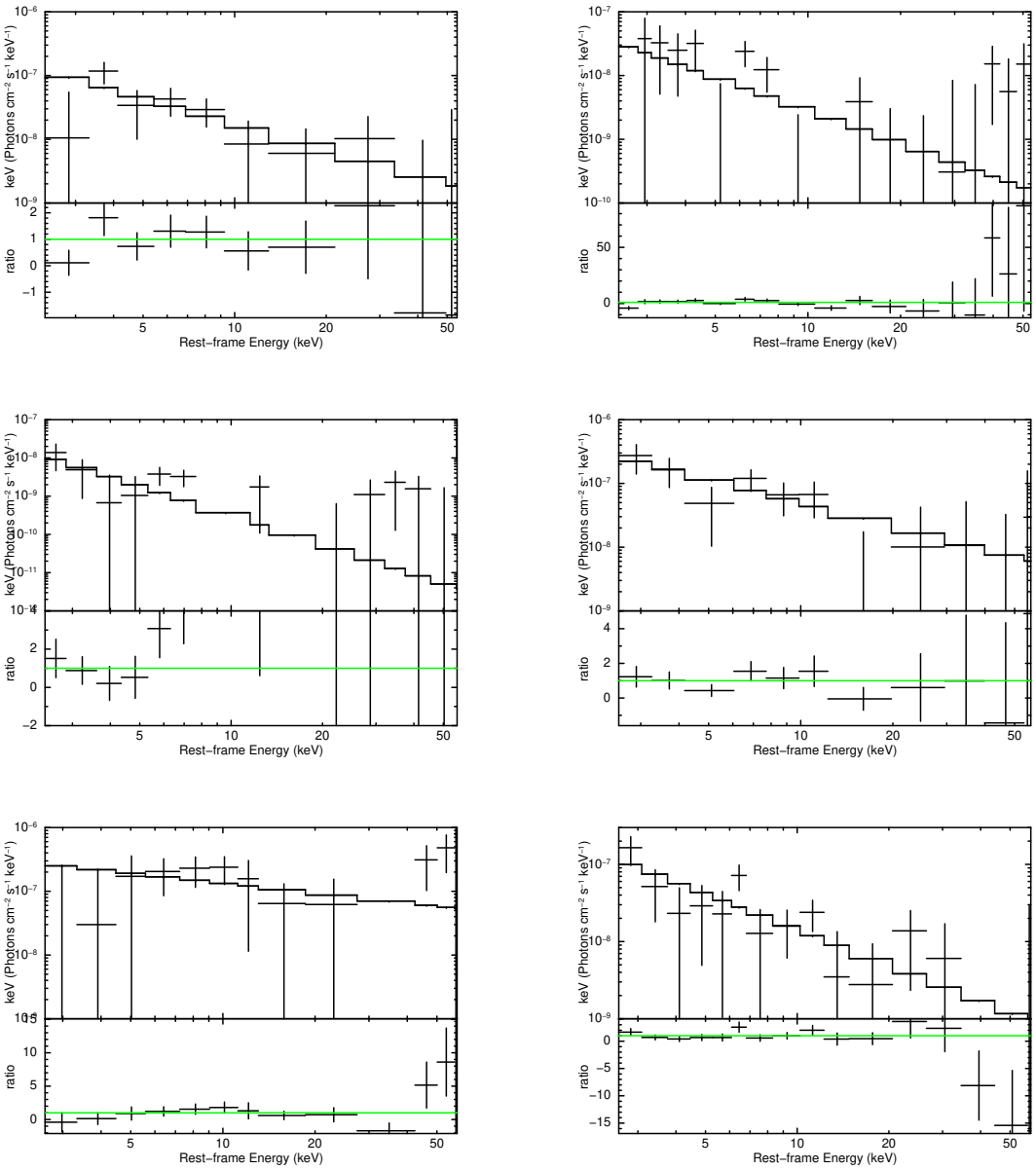

Figure 4.17: Unfolded, deabsorbed and de-redshifted spectra and model of VDES J0020-3653, DES J0252-0503 (top left and right), DELS J0038-1527, ULAS J1120+0641 (middle left and right), J1007+2115 and ULAS J1342+0928 (bottom left and right). Sources are ordered by increasing redshifts. The ratio on the bottom panel is the data divided by the folded model.

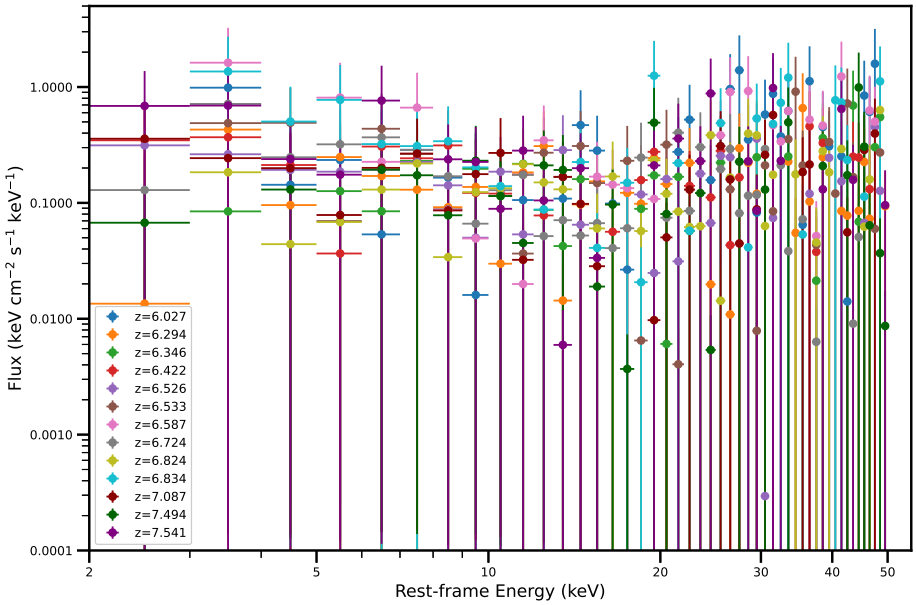

Figure 4.18: Normalized spectra of the 13 HYPERION pn sources with 2 keV energy bins. The sources are represented by their redshifts.

To visualize the normalization of the spectra, we show in Figure 4.18, the binned normalized spectra with 2 keV energy bins. These spectra are deabsorbed, redshift corrected and normalized. Energy bins where we have only upper limits have been removed from the plot. The fluxes are plotted at the mid-point of the energy bin. The normalization is over the energy range of 7 - 15 keV. So as we approach bin sizes of 8 keV, the flux in energy bins that lie in between 8 - 15 keV approaches the same value $\sim$ 0.1 keV cm^{-2} s^{-1} keV^{-1}. We created the average spectrum with 2 keV, 1 keV, 500 eV and 250 eV energy bins and fitted it with a simple power law (pow) model. Table 4.3 show the best fit Γ and normalization along with their 1 σ errors and Figure 4.19 shows the best fit 0.3 - 7.0 keV spectrum but it is presented in the rest frame energies. Since we notice a systematic shift indicating that the debasorbed spectrum has lower Γ than the absorbed spectrum we add to the best-fit Γ value obtained from the average spectrum the systematic shift of 0.28 and we add 1 to it.

Energy Bin	χ^2/dof	Γ	Normalization
2 keV	19.82/22	$2.66^{+0.26}_{-0.24}$	$2.43^{+1.90}_{-1.12}$
1 keV	43.88/46	$2.54^{+0.20}_{-0.20}$	$1.87^{+1.00}_{-0.68}$
500 eV	87.55/93	$2.67^{+0.18}_{-0.18}$	$2.37^{+1.06}_{-0.75}$
250 eV	178.68/187	$2.62^{+0.16}_{-0.16}$	$2.05^{+0.77}_{-0.57}$

Table 4.3: Best-fit parameters from the X-ray spectral analysis of the average pn spectrum using different energy grids using only power-law model. The reported Γ values are the unfolded Γ values along with the added systematic shift.

Energy Bin	χ^2/dof	Cut-off Energy (keV)	Normalization
2 keV	20.06/22	$20.32^{+22.70}_{-7.69}$	$1.39^{+0.51}_{-0.39}$
1 keV	43.30/46	$25.64^{+30.79}_{-9.86}$	$1.297-0.28^{+0.35}$
500 eV	85.94/93	$18.18^{+10.93}_{-5.48}$	$1.43^{+0.33}_{-0.27}$
250 eV	174.96/187	$17.90^{+9.00}_{-4.93}$	$1.35^{+0.26}_{-0.22}$

Table 4.4: Best-fit parameters from the X-ray spectral analysis of the average pn spectrum using different energy grids using only cutoff power-law model.

We also modelled the average spectra with a cut-off power-law model with Γ fixed at 1.9. The best fit parameters are show in Table 4.4 and the best fit model and spectrum is shown in Figure 4.20.

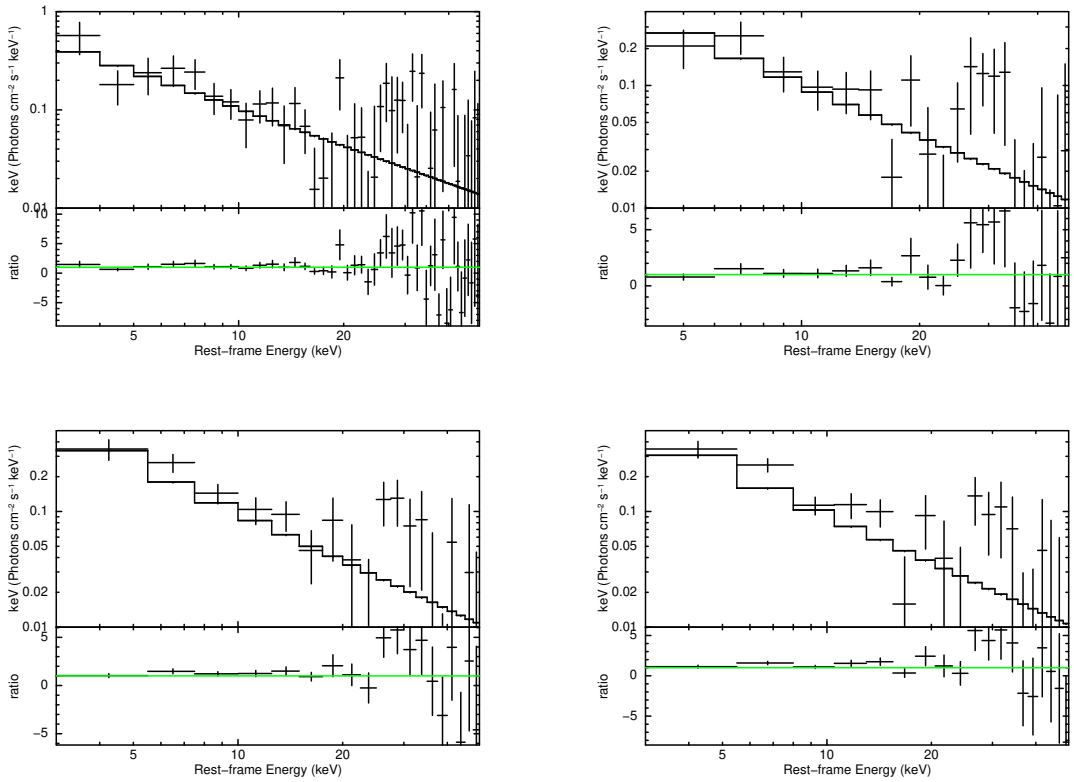

Figure 4.19: Best fit average spectrum using power-law model on the 0.3 - 7.0 keV energy range, presented in terms of rest frame energies. These spectra has been rebinned further for visualization and shown in the rest frame. Energy bins used for the final average spectrum 2 keV (top left), 1 keV (top right), 500 eV (bottom left) and 250 eV (bottom right).

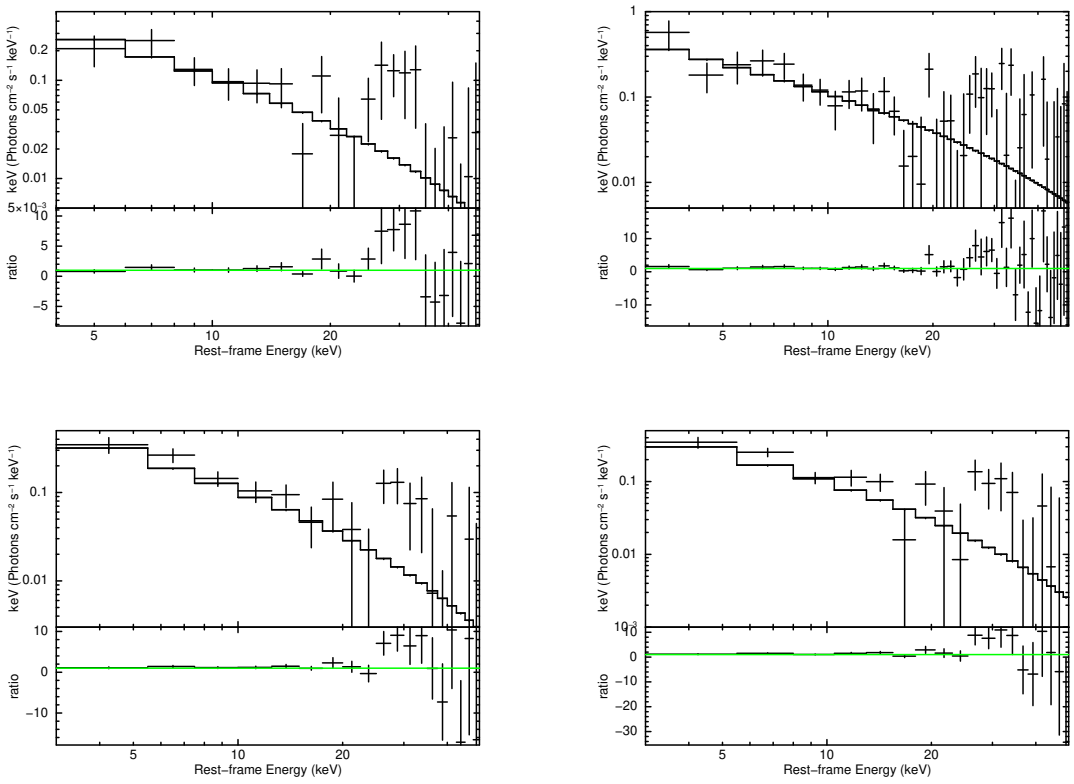

Figure 4.20: Best fit average spectrum using cutoff power-law model on the 0.3 - 7.0 keV energy range, presented in terms of rest frame energies. These spectra has been rebinned further for visualization and shown in the rest frame. Energy bins used for the final average spectrum 2 keV (top left), 1 keV (top right), 500 eV (bottom left) and 250 eV (bottom right).

Energy Bin	χ^2/dof	Γ	Normalization
2 keV	47.51/46	$2.21^{+0.25}_{-0.24}$	$1.67^{+1.27}_{-0.76}$
1 keV	15.28/22	$2.40^{+0.22}_{-0.23}$	$2.16^{+1.29}_{-0.84}$

Table 4.5: Best-fit parameters from the X-ray spectral analysis of the combined pn spectrum created using median using different energy grids using only power-law model. The reported Γ values are the unfolded Γ values along with the added systematic shift.

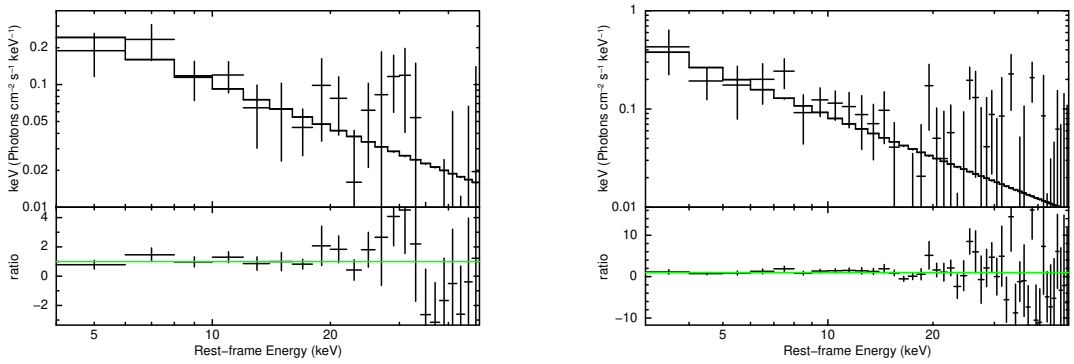

Figure 4.21: Best fit model and spectrum combined using median. These spectra has been rebinned further for visualization and shown in the rest frame. Energy bins used for the final combined spectrum 2 keV (left) and 1 keV (right).

We combined the spectrum using unweighted mean but we combined combining the spectrum using median instead of mean. For the case of 1 keV energy bin the best fit Γ for a simple power-law fit gives $\Gamma = 2.40^{+0.22}_{-0.23}$. Figure 4.21 shows the best fit model and spectrum for the 1keV and 2 keV energy bins while Table 4.5 shows the best fit values. These values are similar to the best fit Γ values obtained from the average spectrum created using mean.

We also simulated spectra using the pn source, background and response files of the HYPERION sources. We did 3 sets of simulations and for each simulation we used the best fit model and exposure of the corresponding sources as quoted in Table 4.2 and 4.1. Then for each set, we created an average spectrum with those spectra that had greater than 40 counts. Here we compared the best fit Γ values of the absorbed and deabsorbed spectrum. Since we used spectra which had > 40 counts, we had 16, 14 and 10 spectra for simulation 1, 2 and 3 respectively. Despite our simulations in Section 4.2, we see that for these simulations there is a systematic shift where deabsorbing the spectrum

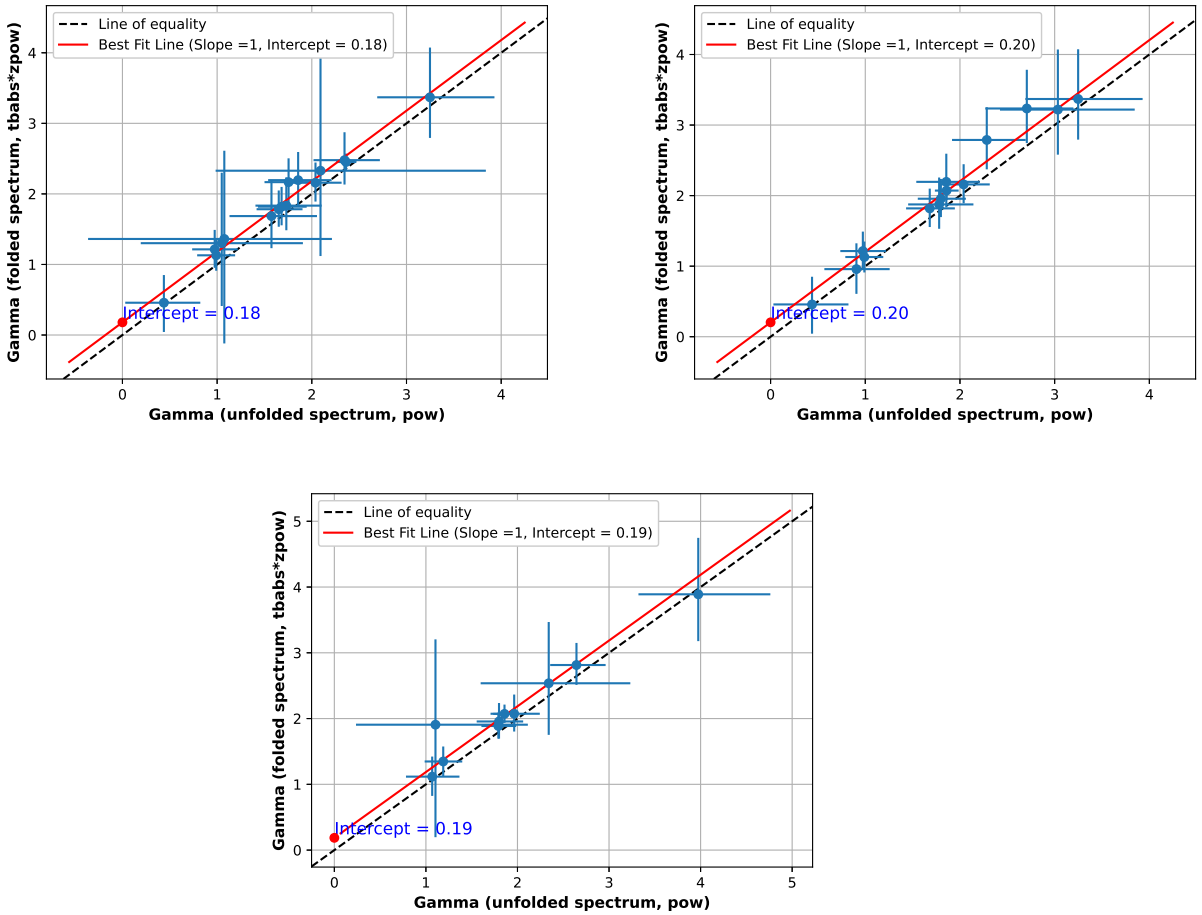

Figure 4.22: Comparison of best fit Γ values of absorbed and deabsorbed spectrum of the pn simulations; simulation 1 (top left), simulation 2 (top right) and simulation 3(bottom).

tends to create a spectra with lower Γ (See Figure 4.22). For the case of the simulations we see that the shift is 0.18, 0.20 and 0.19 for simulations 1, 2 and 3 respectively. This value is slightly lower than that obtained from the HYPERION QSO.

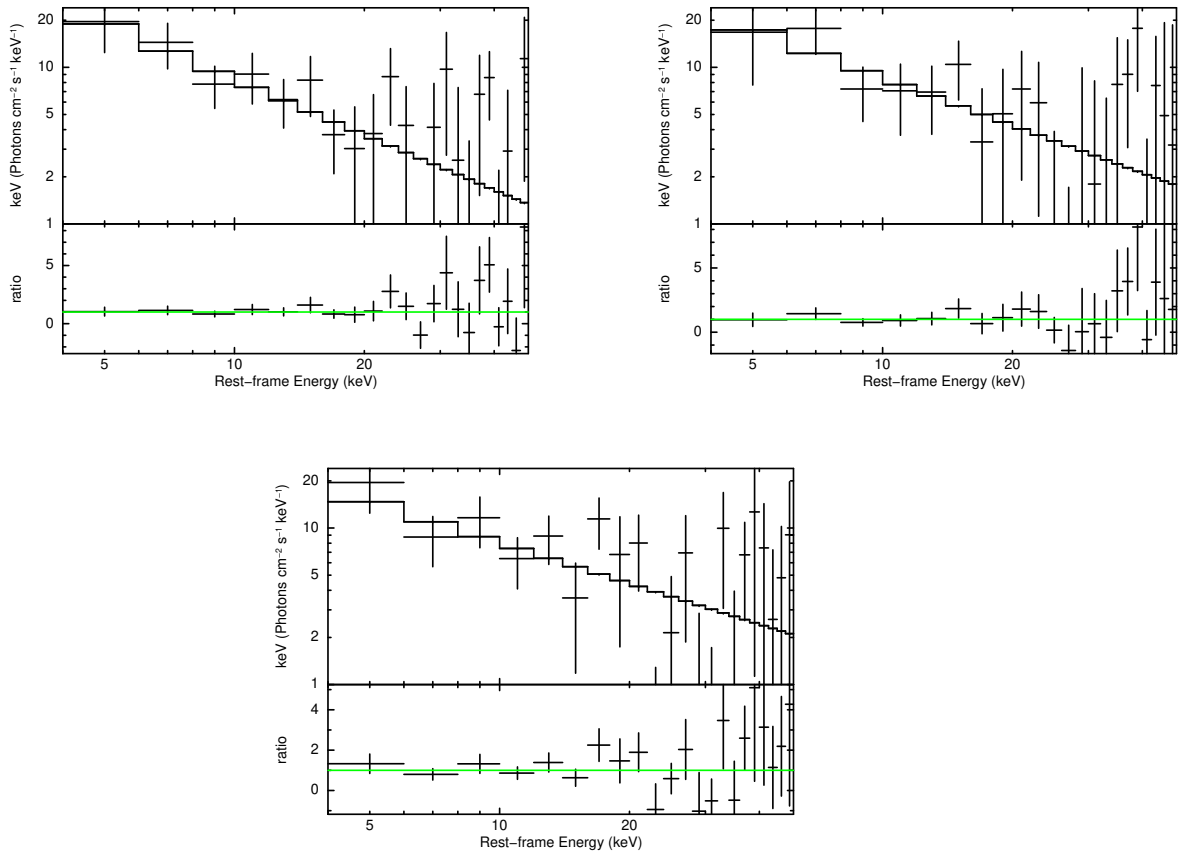

Figure 4.23: Best fit model and spectrum of simulation set 1 (top left), 2 (top right) and 3(bottom) using pn source, background and response files along with their best fit Γ, N_H, exposure time and counts.

Figure 4.23 shows the best fit model and spectra for the average spectrum of the 3 simulations. The best fit Γ for Simulation 1 = $2.34^{+0.28}_{-0.27}$ with χ^2/dof = 15.81/22, for Simulation 2 best fit $\Gamma = 2.20^{+0.40}_{-0.37}$ with χ^2/dof = 11.20/22 and for simulation 3 best fit $\Gamma = 2.05^{+0.30}_{-0.28}$ with χ^2/dof = 17.33/22. In all these cases we take into account the systematic shift show in Figure 4.22 for each spectrum.

Chapter 5

Results and Discussion

In this study we present the HYPERION sample of QSOs at the EoR selected for their fast SMBH growth history (Zappacosta et al., 2023). HYPERION QSOs are selected to be powered by SMBHs that would descend from seeds of $M_{s,Edd} > 10^3\ M_\odot$ at $z = 20$ if accreting continuously at the Eddington rate. This implies a challenging growth history for current models: Either they grew from heavy seed if accreting a sub-Eddington rate or they grew at super-Eddington rates starting from light seeds BH. The HYPERION sample consists of 18 QSOs at redshifts $z \approx 6$ - 7.5 (mean $z \sim 6.7$) with an average luminosity of $L_{bol} \approx 10^{47.3}$ erg s^{-1} and $M_{BH} \approx 10^9$ - $10^{10} M_\odot$.

5.1 Single QSOs X-ray Properties

We analyzed the best-quality X-ray data available to date for such large number (18) of $z > 6$ AGN deriving mainly from 2.4 Ms *XMM-Newton* from a dedicated multi-year Heritage Program aiming at the X-ray characterization of their nuclear properties. In this thesis we performed the X-ray analysis of the HYPERION QSOs exploiting data from only EPIC-pn, the most sensitive *XMM-Newton* detector. We first performed the X-ray spectral analysis of all 18 sources using the `zpow*tbabs` model on XSPEC. We obtain values of Γ between 1.4 and 2.5 although with large 1σ uncertainties which on average are 0.72. Despite this we find the average $\Gamma \sim 2.36 \pm 0.16$. Zappacosta et al. (2023) studied 12 of the HYPERION samples performing the X-ray analysis for the 10 sources detected in their dataset. They adopted the same model but employed

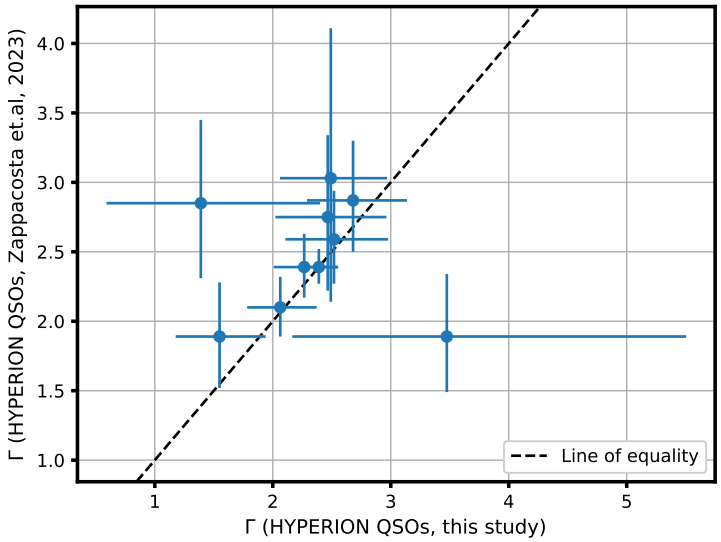

Figure 5.1: Comparison of best fit Γ values of HYPERION QSOs in this study and Zappacosta et al. (2023).

the full data set including spectra from both the pn and MOS1/MOS2 detectors. A comparison of the best fit Γ values of the sources that are in common between this study and Zappacosta et al. (2023) is reported in Figure 5.1. Our derived best fit values are in agreement, within large uncertainties, with those reported by Zappacosta et al. (2023).

Figure 5.2 shows the distribution of Γ as a function of $\lambda_{\rm Edd}$ for our HYPERION QSOs and other AGN and QSOs. Other $z > 6$ QSOs that are not included in the HYPERION sample because they did not meet the HYPERION selection criteria but have good quality data with $>$ 30 net counts (Vito et al., 2019) show, on average, flatter Γ values probably indicating a dependence in $\rm M_{s,Edd}$ and hence on the growth rate histories of these sources. Other λ_{Edd} - analog QSO samples at lower redshift, that is, the hyperluminous WISSH z = 2 - 3 QSOs from Zappacosta et al. (2020) and the high-λ_{Edd} nearby ($z < 1$) QSOs from Laurenti et al. (2022), have noticeably flatter Γ, in agreement with the canonical Γ = 1.8 - 2 values.

We also compared the behavior of the X-ray coronal luminosity of the HYPERION QSOs to the bolometric radiative output. The bolometric correction $\rm K^{X}_{bol} = L_{bol}/L_{2\text{-}10}$ has a somewhat flat trend at Seyfert-like luminosities progressively increasing toward higher luminosity sources. Figure 5.3 shows the bolometric correction as a function of $\rm L_{bol}$. The HYPERION QSOs seem to follow a trend similar to other data except for the

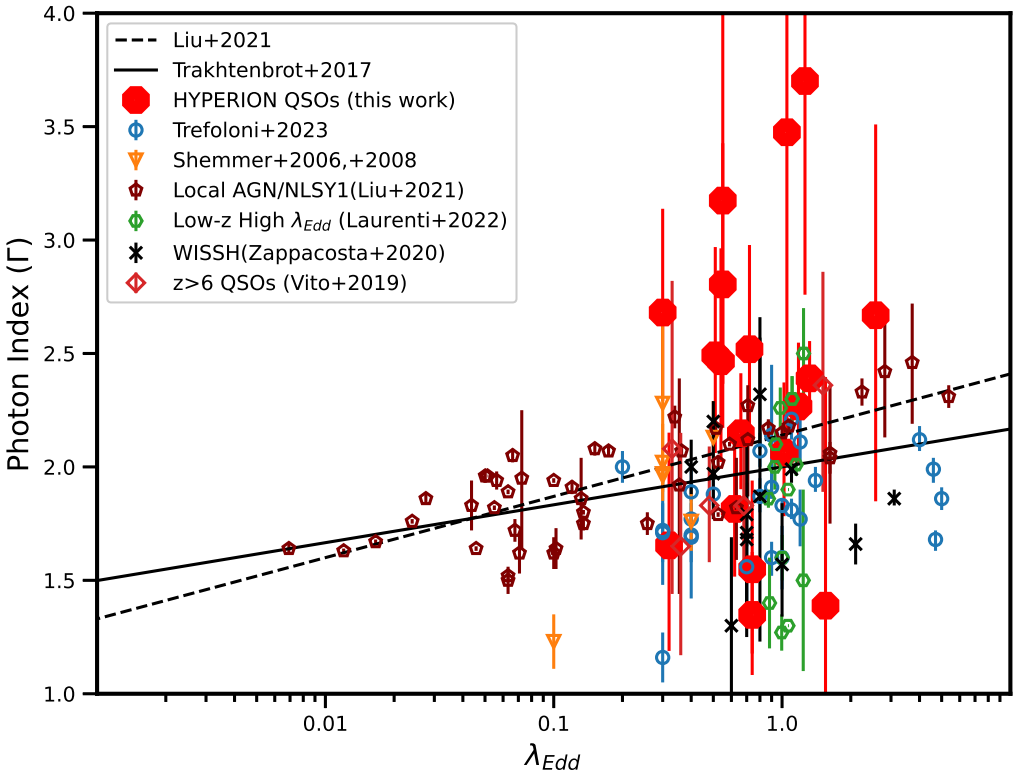

Figure 5.2: Γ vs. λ_{Edd} for a compilation of local or high-λ_{Edd} AGN and high-redshift luminous QSOs. Red octagons points are the HYPERION QSOs presented in this work. Red diamonds are other z > 6 QSOs detected with ≥ 30 net counts from the X-ray spectral analysis performed by Vito et al. (2019) and not included in the HYPERION sample. QSOs at Cosmic Noon (z = 2 - 4) are reported as black asterisks (the WISSH QSOs from Zappacosta et al. 2020), empty orange arrow (Shemmer et al. 2008), and blue circle (Trefoloni et al. 2023). Local high-λ_{Edd} QSOs (Laurenti et al., 2022) and local AGN including Narrow Line Seyfert 1 (NLSy1s) galaxies (Liu et al., 2021) are shown as green hexagon and brown pentagons, respectively. The uncertainties on λ_{Edd} from QSOs with M_{BH} estimated using a single-epoch virial mass estimator are dominated by systematic uncertainties and can be as high as 0.5 dex. The statistical uncertainty on λ_{Edd} for the local AGN (Liu et al., 2021) whose masses are estimated via reverberation mapping is 0.1 dex and 0.2 dex for the sub-Eddington and super-Eddington sources, respectively.

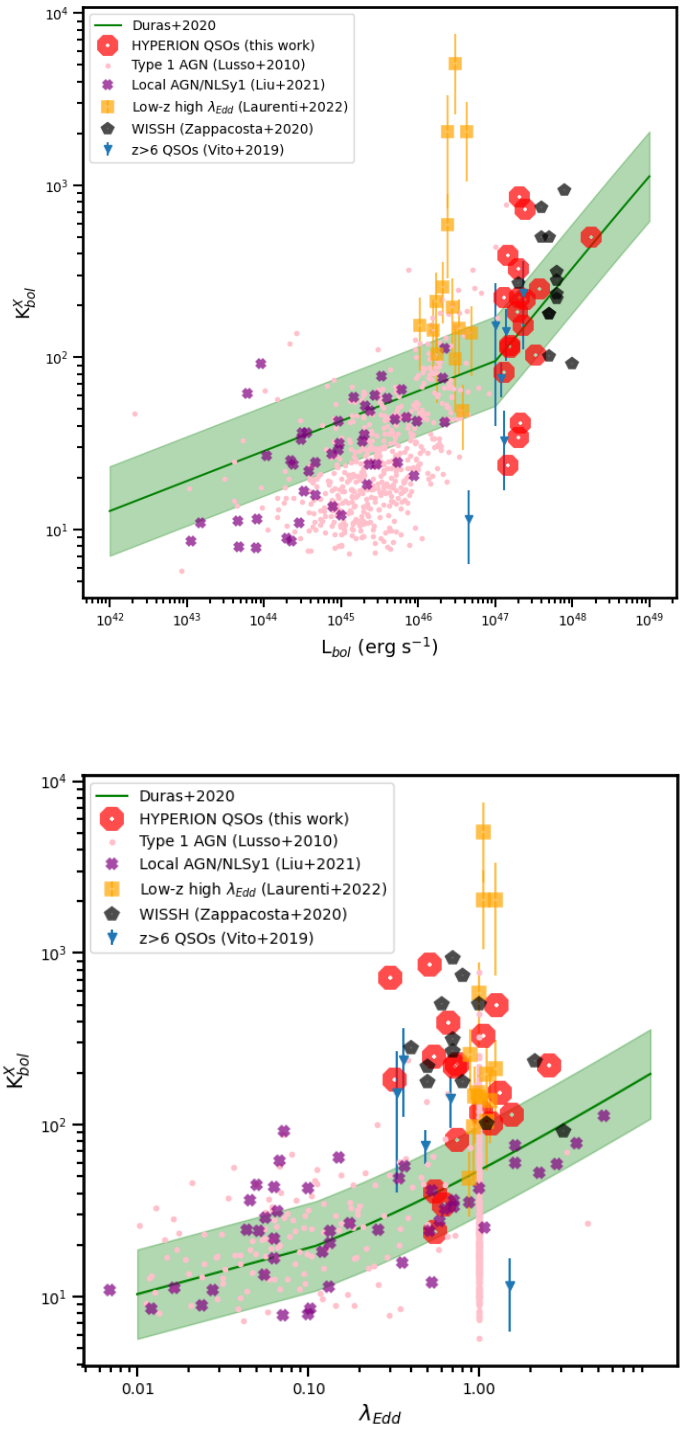

Figure 5.3: (Top) K^X_{bol} vs. L_{bol} for a compilation of broad-line mostly high-z QSOs and local AGN. We also added COSMOS Type 1 AGN (pink dots) from Lusso et al. (2010). (Bottom) K^X_{bol} vs. λ_{Edd} for the same sources with SMBH measurements available. The gree solid lines show the represent the fitting relation reported in Duras et al. (2020) and its 1σ spread.

low-z high λ_{Edd} QSOs of Laurenti et al. (2022). But the location of the HYPERION QSOs in Figure 5.3 that shows the λ_{Edd}-K^X_{bol} plane appear to be in disagreement with the trend reported by Duras et al. (2020) and shows the lack of a clear dependence between λ_{Edd} and K^X_{bol}. This is mainly due by the steep L_{bol} dependence of K^X_{bol} at high-luminosity regimes. The exception to this is the lower-luminosity sample of Laurenti et al. (2022), which mainly deviates because of the overall X-ray weakness of the sources, which is possibly a result of optical selection coupled to the high-λ_{Edd} requirement. This is not well sampled by Duras et al. (2020) and is dominated by the bulk of the low-luminosity, highly accreting AGN population.

5.2 On the Average X-ray Constraints

We combined the HYPERION QSOs using energy bins of 2 keV, 1 keV, 500 eV and 250 eV because we wanted to check the dependence of Γ on the binning size. We fit a simple power-law model on the average spectra and we see that we get steep $\Gamma > 2.3$. Indeed we find no dependence of the best fit Γ values from the binning size, obtaining values in the range 2.5 - 2.7. We obtained $\Gamma = 2.54 \pm 0.20$ for the average spectrum created using 1 keV energy bins and is, within errors, consistent with the values Zappacosta et al. (2023) obtained in the power-law joint spectral analysis of the ten detected sources which was $\Gamma \approx 2.4 \pm 0.1$.

In the Γ vs. z plot reported in Figure 5.4, we show the best fit Γ obtained from the average spectrum created using 1 keV energy bin, along with joint analysis Γ value from Zappacosta et al. (2023) and other independent joint analyses of $z \geq 6$ QSOs (Nanni et al. 2017; Vito et al. 2019; Wang et al. 2021). The average redshift of the HYPERION sample used here is $z = 6.71$. We also report in the plot, previous stacked spectral analysis Γ values from other luminous QSO samples at $1 < z < 6$ (Shemmer et al. 2008; Just et al. 2007), the average values for the WISSH QSOs from Zappacosta et al. (2020), and the local PG QSOs from Piconcelli et al. (2005). Other than the local QSOs in Piconcelli et al. (2005), these are samples of sources similar to the HYPERION sources in terms of L_{bol} and/or λ_{Edd}. All $z < 6$ results from these analogous sources show consistently $\Gamma \approx 1.8$ - 2. The average Γ from all the considered $z < 6$ QSO samples

is $\Gamma_{z<6} = 1.91 \pm 0.04$. This implies that our average gamma is significantly different at the 3 σ level over the average gamma for $z < 6$ sources. This is a confirmation, exploiting data from a different and larger HYPERION sub-sample and with a different methodology, of the average steep gamma reported by Zappacosta et al. (2023).

The Γ of HYPERION QSOs is steeper regardless of the luminosity or accretion rate of the QSOs and therefore shows that it is due to a new regime for the X-ray properties of bright QSOs at the EoR. Given the selection criteria used to build the HYPERION QSO sample and the average flat Γ from the > 30 counts $z >$ QSOs by Vito et al. (2019), which are excluded by the HYPERION selection, we think that, this evolutionary effect is possibly linked to the particularly fast SMBH mass growth history experienced these sources. To test the hypothesis, we divided the 13 HYPERION QSOs with counts between $\sim$ 40 and 110, into 2 approximately equal sub-samples according to their SMBH growth history and therefore based on their $M_{s,Edd}$. We adopted a threshold value between the 2 sub-samples as $M_{s,Edd} = 4 \times 10^3 M_{\odot}$ with the high $M_{s,Edd}$ sub-sample including J1342, J1120, J0020, J036, J1148, J231 and J1007 and low $M_{s,Edd}$ sub-sample including J0244, J0224, J083, J029, J025 and J0411. We combine the spectra in each sub-sample. Both the sub-samples have comparable number of counts with the high $M_{s,Edd}$ sub-sample having 465 net-counts and low $M_{s,Edd}$ sub-sample having 432 net-counts. We used a power-law model on the average spectrum of the high and low $M_{s,Edd}$ sub-sample and obtained $\Gamma = 3.06^{+0.40}_{-0.37}$ with $\chi^2/\mathrm{dof} = 17.61/22$ for the high $M_{s,Edd}$ sub-sample and $\Gamma = 2.31^{+0.32}_{-0.31}$ with $\chi^2/\mathrm{dof} = 17.29/22$ for the low $M_{s,Edd}$ sub-sample. Figure 5.5 shows the best fit model and spectra for these two cases. This is in agreement with the values and trend obtained by Zappacosta et al. (2023) who performed a joint spectral analysis for each sample. For the high-$M_{s,Edd}$ sample, they obtained $\Gamma = 2.64/2.7$, with an uncertainty of $\sim$ 0.16, and for the low-$M_{s,Edd}$ sample, they obtained $\Gamma = 2.21 \pm 0.13$. The average redshift of our sub-samples were 6.928 and 6.460 for the high and low $M_{s,Edd}$ sub-sample respectively. Therefore, the Γ difference could also be due to a redshift (i.e., temporal) dependence. We also used a cutoff power-law model on the high and low-$M_{s,Edd}$ sub-samples. For the high-$M_{s,Edd}$ we get $\mathrm{E_{cut}} = 10.57^{+8.11}_{-3.65}$ keV while for the low-$M_{s,Edd}$ sample we get the lower bound of $\mathrm{E_{cut}}$ as 23.93 keV.

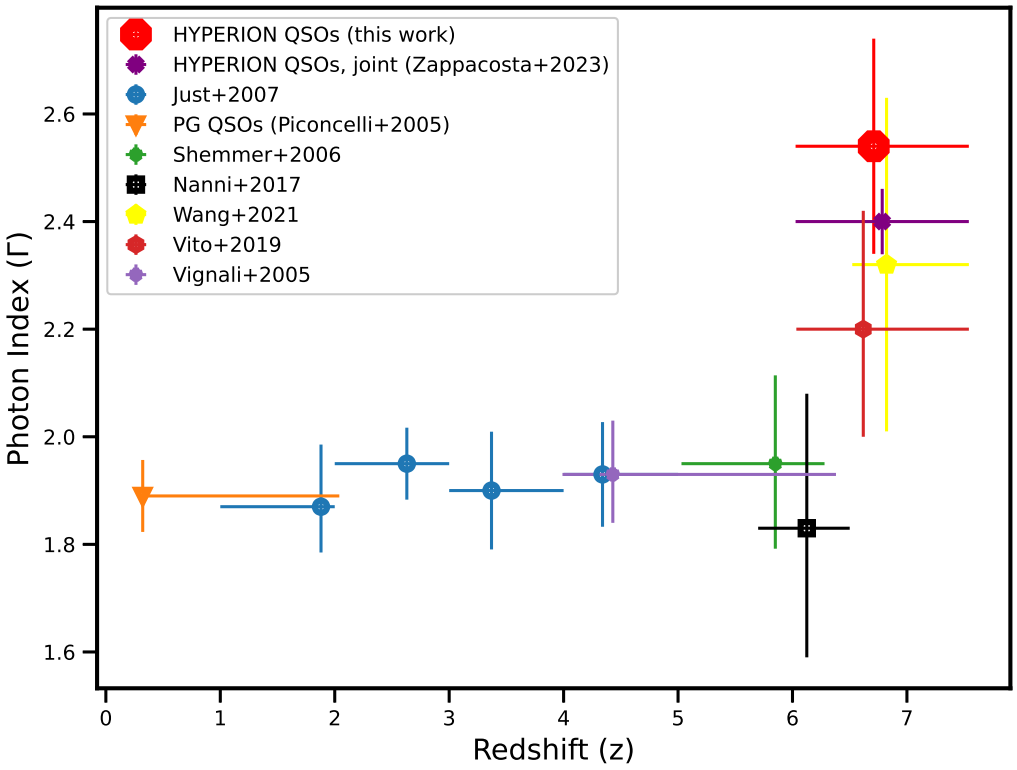

Figure 5.4: Distribution of the average Γ as a function of redshift. The plot includes data from joint spectral analysis or average values from samples of QSOs.The red octagon is from the average spectrum of the HYPERION sample created using 1 keV energy bins. The maroon circle, purple circle, red circle, the yellow point, the black squares are the HYPERION QSOs from Zappacosta et al. (2023), and the samples of Vignali et al. (2005), Vito et al. (2019), Wang et al. (2021), and Nanni et al. (2017) respectively. The blue circle and green circles are averages from the stacked spectral analyses of luminous and hyperluminous QSOs from Just et al. (2007), and Shemmer et al. (2006), respectively. The orange triangle represents the average Γ from the PG QSOs from Piconcelli et al. (2005). Vertical error bars report 1σ uncertainties on Γ while horizontal error bars indicate the redshift range covered by the QSO sample considered in each dataset.

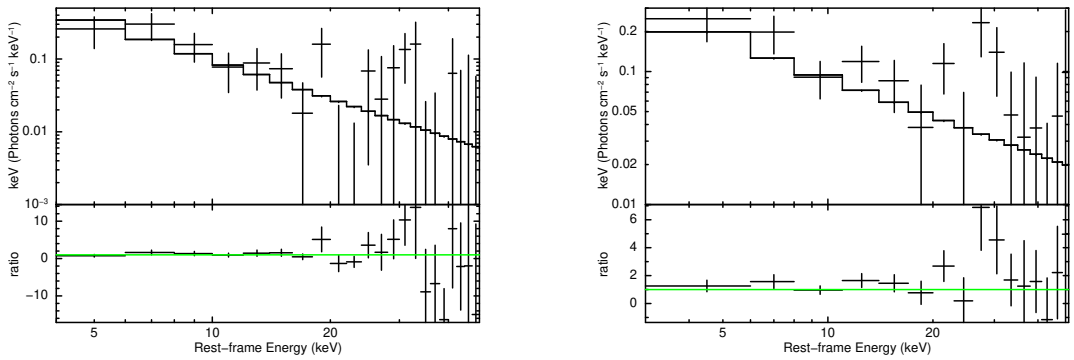

Figure 5.5: Best fit average spectrum using power-law model on the 0.3 - 7.0 keV energy range, presented in terms of rest frame energies of the high and low $M_{s,Edd}$ sub-sample. These spectra have been created using bins size of 1keV.

To explore the redshift dependence we divided the 13 HYPERION QSOs into low-z and high-z sub-samples with $z = 6.587$ as the dividing line as this also the mean of the HYPERION sample. The high-z sub-sample includes J231, J0244, J0411, J0200, J1120, J1007 and J1342 with an average $z = 7.01$ and ≈ 473 net-counts while the low$-z$ sub-sample includes J029, J025, J083, J0224 and J036 with average $z = 6.35$ with ≈ 473 net-counts. We obtained a best fit $\Gamma = 2.80^{+0.33}_{-0.34}$ with $\chi^2/\mathrm{dof} = 27.91/22$ while for a low-z sub-sample we get $\Gamma = 2.64^{+0.36}_{-0.38}$ with $\chi^2/\mathrm{dof} = 18.62/22$. So we see a trend of steeper Γ for high z samples than for low z samples. This is definitely consistent with the trend reported by Zappacosta et al. (2023) who performed joint analysis of the five lowest-redshift QSOs and five highest-redshift QSOs (z = 6.29 and z = 6.94, respectively) obtaining $\Gamma = 2.21/\ 2.29$ ($\pm \sim 0.14$) and $\Gamma = 2.64^{+0.17}_{-0.16}$ respectively. These evidences of dependence are marginal (< 2 sigma) but they are reported also in Zappacosta et al. (2023) analysis (at $\sim 2.3\ \sigma$). The average redshift of the two sub-samples (divided in z) implies that the redshift dependence would need to act on a time scale of $< 10^8$ years. This time scale is too short to act on a entire population of sources even at early cosmic times. Hence the most likely explanation is that Γ could depend on $M_{s,Edd}$, i.e. on the different growth rate histories experienced by the source in the two sub-samples.

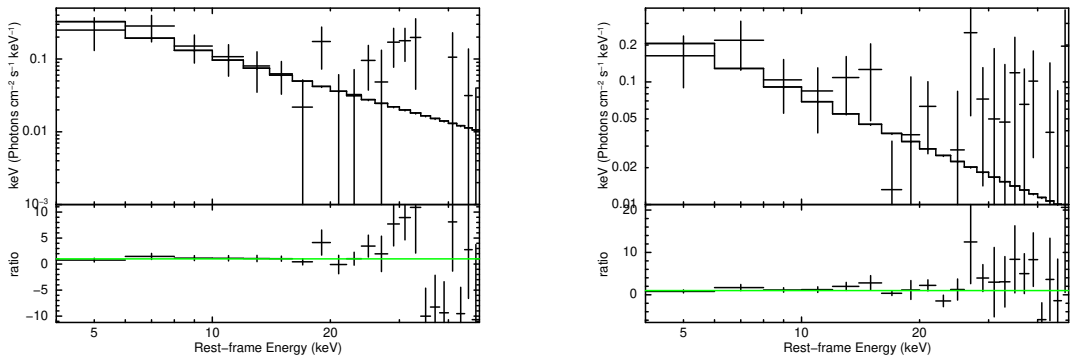

Figure 5.6: Best fit average spectrum using power-law model on the 0.3 - 7.0 keV energy range, presented in terms of rest frame energies of the high (left) and low-z (right) subsample.

A steep spectrum can also be mimicked by a power-law with canonical $\Gamma = 1.9$ and a high-energy cutoff at relatively low energies. Figure 5.7 shows the distribution of energy cutoff E_{cut} as a function of X-ray luminosity ($L_{2\text{-}10}$). The average of the 13 HYPERION QSOs has been compared to the joint spectral fit of 10 HYPERION QSOs from Zappacosta et al. (2023), $z < 0.5$ lower-luminosity AGN and to $z = 2$ - 4 hyperluminous lensed QSOs (Lanzuisi et al. 2019; Bertola et al. 2022) as well as to local super-Eddington accreting AGN from Tortosa et al. (2023).

We used a cutoff power-law model on the fiducial average spectrum created using 1 keV energy bins by assuming $\Gamma = 1.9$ and obtained $E_{cut} = 25.64^{+30.76}_{-9.86}$ keV. The HYPERION value of E_{cut} is at very low energies and although it is consistent with a few measurements for low-luminosity local AGN, it is inconsistent with the few measurements for QSOs at similar $L_{2\text{-}10}$ and also with the bulk of the lower luminosity AGNs (see Figure 5.7). This alternative hypothesis shows that also in this case the spectrum of the HYPERION QSOs is different from the bulk of the AGN population. This is a further confirmation that $z > 6$ sources are in a new regime of their nuclear properties. Figure 5.8 shows the comparison of best fit spectra using power-law and cutoff power-law. As can be seen, the two models are mostly indistinguishable at < 20 keV. They start deviating from each other at higher energies where the data have the largest uncertainties. Indeed the best-fit χ^2/dof are almost indistinguishable being 43.88/46 and 43.30/46 for the power-law and cutoff power-law case, respectively.

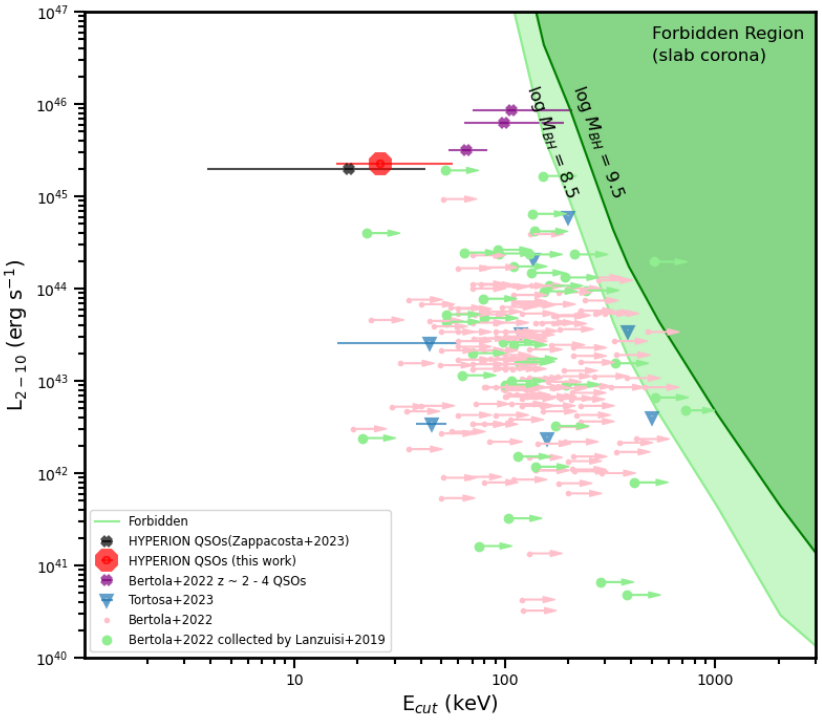

Figure 5.7: Distribution of E_{cut} as a function of L_{2-10}. The HYPERION E_{cut} measurement from average spectrum created using 1 keV energy bin (assuming $\Gamma = 1.9$) is shown in red. Purple points and green circles are estimates from a compilation of local AGN (Bertola et al. 2022, and references therein) and z $\sim$ 2 - 4 QSOs (Lanzuisi et al. 2019; Bertola et al. 2022). Blue triangle are from local super Eddington accreting AGN from Tortosa et al. (2023). The HYPERION average E_{cut} measurement (assuming $\Gamma = 1.9$) from the joint analysis by Zappacosta et al. (2023) is marked in black. Green regions are the forbidden regions (for a slab corona model) due to runaway electron-positron pair production (see Svensson 1984) for $\log(M_{BH}/M_\odot) = 8.5$ and $\log(M_{BH}/M_\odot) = 9.5$.

5.3 Looking for Additional Spectral Components on the Average X-ray Spectrum

In few of the combined spectra of the HYPERION QSOs, we report the presence of a excess of counts between $\sim$ 20 - 30 keV. This looks like a modification from the power-law model. The position of this feature is possibly consistent with a Compton hump from cold reflection component but the feature is much narrower to be modelled with a cold reflection model (we tried `pexrav`). We therefore modelled it with a Gaussian profile obtaining a best-fit of $\chi^2/\mathrm{dof} = 37.95/42$ and a measure of its position at $\sim$

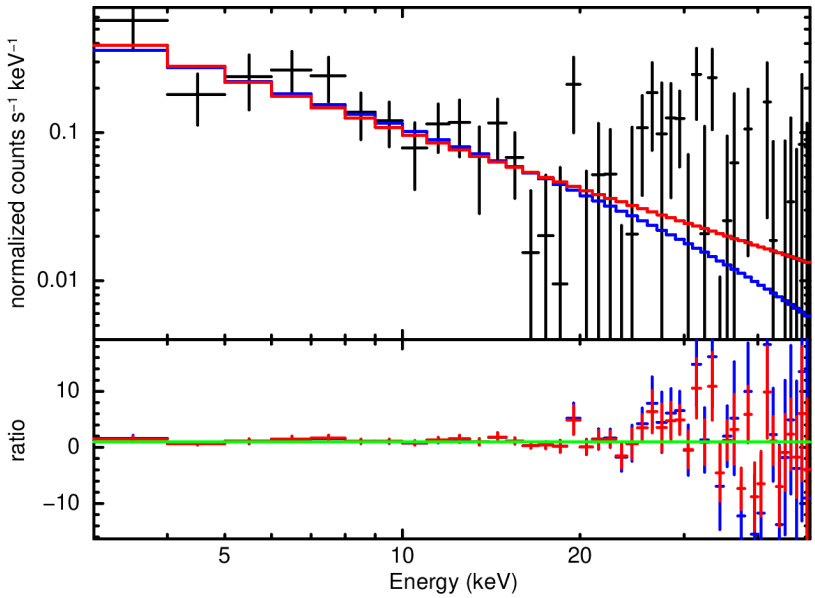

Figure 5.8: Comparison of best fit spectra using power-law model and cutoff power-law using the average spectrum created using 1keV energy bins. The black points indicate the data points, the red line is the best fit power-law model and the blue line is the best fit cutoff-powerlaw model.

28 keV and its width at $\sigma \sim 1.7$ keV (see Figure 5.9). Assuming this is the correct parametrization through an ftest we find that this is a better parametrization of the power-law model at only $\sim 91\%$ c.l. which is insufficient to prefer a model with this component over a power-law model without it. We do not know if it is a true component or due to an artifact of instrumental effect or a background feature. But we tested how its presence affects Γ of the average spectrum. So we perform a fit using a power-law model on the average spectrum created using 1 and 2 keV energy bins but we removed this component between 25 - 32 keV while performing the fit. We obtained $\Gamma = 2.80^{+0.27}_{-0.26}$ with $\chi^2/\mathrm{dof} = 12.59/18$ for the average spectrum created using 2 keV while for the 1 keV bin, we get $\Gamma = 2.64^{+0.21}_{-0.20}$ with $\chi^2/\mathrm{dof} = 33.22/38$. Figure 5.10 shows the best fit model and spectrum for these fits. If we use the cutoff-power law after removing this excess, the high energy cutoff is 25.45 keV. Hence, it's presence does not significantly affect our results.

We checked for the presence of a Fe Kα line (at 6.4 keV), a typical line emission feature in type 1 AGN with equivalent width (EW) of ~ 100 keV, to see if it is present in these sources. Therefore we adopt a finer binning spectrum of 500 eV and fit the average spectrum using a power-law model with an additional Gaussian component for

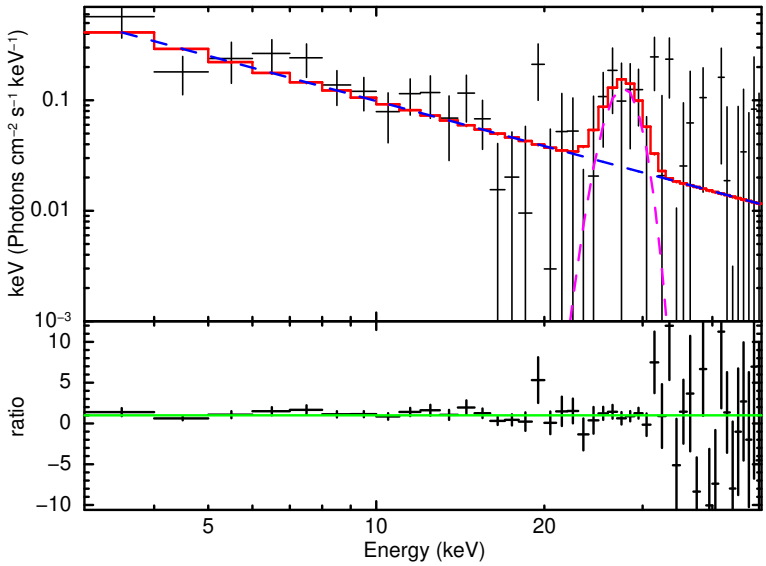

Figure 5.9: Best fit model and spectrum created using 1 keV energy bin to test for Compton hump from cold reflection. The data is shown in black while the best fit model is marked in red.

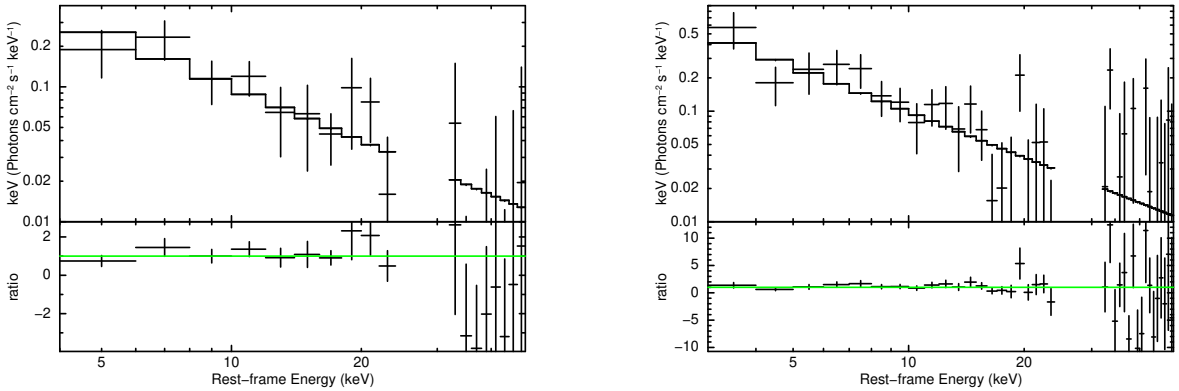

Figure 5.10: Best fit model and average spectrum created using 2 keV (left) and 1 keV (right) energy bins. A power-law model has been used here but in the spectrum we have removed the hump feature seen between 20 - 30 keV.

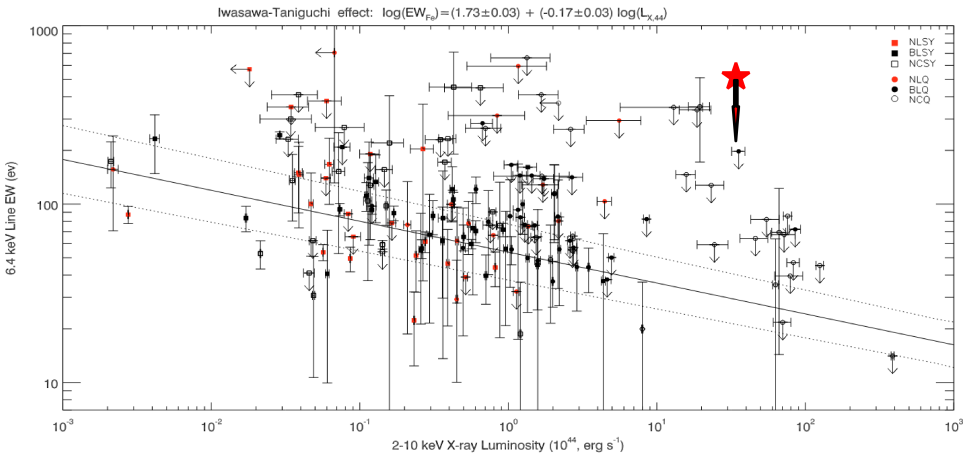

Figure 5.11: This plot, adopted from the Bianchi et al. (2007), show the "IT effect". It shows that neutral iron EW against 2 - 10 keV X-ray luminosity. We plot the upper limit of the equivalent width of the Fe kα line for this sample using average spectrum created using 500 eV energy bins (blue star). The anti-correlation between the two parameters is shown as the best fit line, whose analytical expression is reported on the top. The broken lines represent the combined error on the slope and normalization of the best fit of the sources studied by Bianchi et al. (2007). The different symbols refers to the classification of the objects, on the basis of their absolute magnitude and Hβ FWHM: NLSY, narrow-line Seyfert 1; BLSY, broad-line Seyfert 1; NCSY, not-classified Seyfert 1 (no Hβ FWHM measure available); NLQ, narrow-line quasar; BLQ, broad-line quasar; NCQ, not-classified quasar (no Hβ FWHM measure available). See (Bianchi et al., 2007) and references therein.

the Fe Kα line (`pow+gauss` model) fixing Γ to its best-fit value and the energy of the line (forced to be unresolved) to 6.4 keV. We obtained a best-fit with $\chi^2/\mathrm{dof} = 86.7/93$ (see Figure 5.12). The line is not detected and we get a 90% upper limit for its EW of 0.71 keV. Figure 5.11 shows the upper limit on the Fe Kα EW vs $L_{2\text{-}10}$ luminosity plot. At these high luminosities ($> 10^{45}$ erg/s) we expect to find the lowest EW according to the Iwasawa-Taniguchi (IT) effect (Iwasawa and Taniguchi 1993, Bianchi et al. 2007). We need data of much better quality to get to the few tens of keV expected EWs. In any case in this regime the majority of the data comes from upper limits and there are only few measurements, hence the relation is not well constrained.

HYPERION QSOs are high redshift type 1 sources. Therefore we do not expect very high levels of absorption at energies > 2 keV rest-frame (which are the rest-frame energies probed by *XMM-Newton* at $z > 6$). However we tried to see if some average level of absorption can be constrained. We therefore modelled our fiducial 1 keV binned

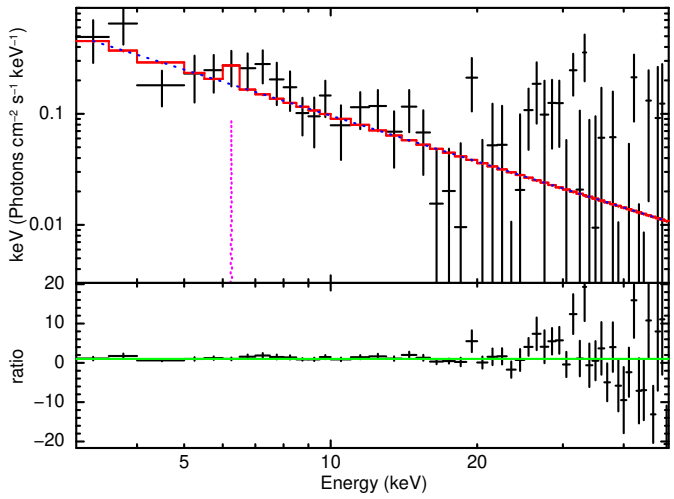

Figure 5.12: Best fit model and average spectra of the HYPERION sample created using 500 eV energy bins. The model used here is `pow+gauss` model where the `gauss` component is used to model an iron line.

spectrum with a `tbabs*pow` model. We obtain a best-fit model (χ^2/dof = 43.76/43) with N_H=4×10^{22} cm^{-2} and Γ=2.69. However this absorption term is not required as the N_H is unconstrained with an upper limit of 4×10^{23} cm^{-2}. This justifies our choice to adopt a simple power-law model to fit the spectra of these sources.

5.4 The Implication of Steep Spectra

In this work we are providing evidence for the presence of peculiar steep gamma or low-energy exponential cutoff. This result, consistent with what has been found by Zappacosta et al. (2023), for a different sample and a different approach provides a methodology-independent confirmation that these sources are in a new and never reported regime for the QSO population across cosmic time.

Our employed spectral stacking methodology allows to obtain the average spectrum of the HYPERION QSOs and hence enable us to evaluate not only the presence of the primary continuum spectral shape (i.e. power-law with or without a roll-off at high energies) but also the presence of expected or unexpected additional significant components, which are difficult to deal with in the joint spectral analysis employed by Zappacosta et al. (2023).

The spectral analysis of the average spectrum from the EPIC-pn only data, does not show significant evidence of modifications from the power-law continuum due to the presence of further known components. We find an unexpected low significance excess of counts at rest-frame energies 20 - 30 keV. This excess is narrower than a Compton reflection hump being only few keV wide. Its origin (if physical or instrumental) is unknown, but its relevance will need to be confirmed with more data. Hence with the current data no significant new components are reported over the standard power-law continuum.

The measured X-ray properties of the HYPERION QSOs are clearly different from QSOs that are similar to them in terms of bolometric luminosity and λ_{Edd} at lower z. The slopes obtained here are typically found in lower $M_{BH} < 10^6$ $M_{\odot}$ with highly accreting low-luminosity AGNs such as NLSy1 galaxies (e.g., Miniutti et al. 2009; Ludlam et al. 2015). Hence, we are characterizing versions of NLSy1 galaxies scaled up in SMBH mass and bolometric luminosity by several orders of magnitudes.

The steep Γ measured for the HYPERION QSOs are also confirmation of the results reported for single but peculiar $z > 6$ sources such as the very bright radio-loud or narrow-line QSOs for which $\Gamma = 2.5 \pm 0.2$ (Medvedev et al., 2021) and $\Gamma = 3.2 \pm 0.7$ (Wolf et al., 2023) have been obtained and on similar samples of luminous $z = 6$ - 7.5 QSOs (Vito et al. 2019, Wang et al. 2021) where marginal evidence for gamma steepening has been reported using both *XMM-Newton* and *Chandra* X-ray observatories.

It is possible that the steepness derives from a different geometry of the accretion disk-corona system (e.g. Kubota and Done 2018), a different coupling between the accretion disk and the corona, possibly mediated by disk-driven winds (e.g.Proga 2005, Laor and Davis 2014, Kawanaka and Mineshige 2021), or from peculiar coronal properties (e.g. Kara et al. 2017, Fabian et al. 2017, Tortosa et al. 2018, Kawanaka and Mineshige 2021).

In any case the characterization of the continuum coronal parameters, i.e. Γ and E_{cut} gives us clues on the physical properties of the corona. Indeed E_{cut} is directly related to the temperature of the corona once a geometry for it is assumed (e.g. for slab/spherical geometries $E_{cut} = 2$ - 3 kT where kT is the thermal energy of the corona; (Petrucci et al., 2000), while Γ is dependent on both temperature and optical depth of

the corona (Beloborodov, 1999).

Given the similarity with the X-ray properties of the NLSy1s we expect HYPERION QSOs to be highly accreting super Eddington sources, whose high soft UV radiation flux is capable to increase the Compton cooling of the corona (Pounds et al., 1995) hence lowering its temperature and giving rise to a steep spectrum. Also the presence of optically thick corona force seed disc photons to undergo multiple scatterings before leaving the corona hence lowering its electron temperature and leading to steep spectra (Tortosa et al., 2017).

The presence of steep spectra in HYPERION QSOs if extended to the $z > 6$ AGN population at lower luminosities implies that sources with similar 2 - 10 keV luminosities will result fainter at the probed rest-frame > 10 keV energies than sources with canonical $\Gamma = 1.8$ - 2 spectra. The faintness can reach also an order of magnitude for the steepest spectra or for sources at $z > 8$ with low energy cutoff. This will provide a natural way to explain the absence of X-ray emission in almost all the broad line AGN detected by *JWST* at $z > 6$ (e.g. Maiolino et al. 2024, Ananna et al. 2024) especially for the highest redshift sources.

Future developments of this study will consider the inclusion of the EPIC-MOS1 and MOS2 on the averaging procedure. Those data will add from up to 40% of the total available data counts in each XMM observation and this will allow us to tighten the constraints on the X-ray emission and possible presence of further spectral components, including the confirmation of the 20 - 30 keV emission feature. We will further optimize the spectral stacking procedure with additional testing:

1. We will optimize the energy range for the renormalization of the spectra;

2. We will use different re-gridding schemes, instead of equal uniform bins we will use binning driven by the signal-to-noise ratio and

3. We will calibrate better the procedure for de-absorption to remove the source of systematic shifts between Γ before and after the procedure.

4. We will test and simulate models comprising the high energy cutoff component, Fe Kα line and presence of variable semi-relativistic absorption from the UFO winds.

Chapter 6

Conclusions

The mere existence of SMBH with M_{BH} as large as 10^9 $M_\odot$ or more powering luminous QSOs at EoR poses challenges to theoretical models designed to explain how these systems formed so quickly in much less than 1 Gyr. A way to study their nature is through the QSO X-ray emission. Indeed, X-rays give us instantaneous information about the innermost accreting regions of the growing BH. The HYPERION sample of luminous QSOs are powered by the SMBH which experienced the most extreme mass growth and hence includes the sources most problematic to form. Therefore, these sources represent the most extreme QSOs at $z > 6$. Our aim is to study their nature in the X-ray for these sources, we have have a 2.4 Ms ($\sim$ 700 hours) of observations to collect unprecedented high-quality X-ray data for such a large sample of QSOs at EoR. This would ensure a good characterization of their X-ray spectral properties, in particularly the photon index of the power-law and the 2 - 10 keV luminosity ($L_{2\text{-}10}$) on these sources. In this thesis we study this $z > 6$ QSO sample by performing a stacking analysis of all the spectra to generate, for the first time, a good quality (> 1000 counts) average QSO spectrum at $z > 6$. Previous analysis had fewer sources and had combined net-counts that were an order of magnitude lower than what we have now.

The X-ray spectral analysis performed individually on 18 sources show that the Γ values range from 1.4 to 2.5, with an average of $\Gamma \sim 2.36 \pm 0.16$. This is remarkably steeper compared to similar QSOs at $z < 6$. The spectra of these sources have an average of $\sim$ 80 net-counts in the 0.3 - 7.0 keV energy range. The X-ray luminosities of these sources, compared to the total bolometric luminosity is in well agreement with

the expectations from low-z QSOs.

We create the average spectrum using data for 13 sources that had net-counts $\sim$ 40 - 110 (i.e. excluding outliers with fewer or many more counts). The spectral analysis resulted in a best-fit power-law model with $\Gamma = 2.54 \pm 0.2$. The Γ obtained here is steep and significant (at the 3 sigma level) over the Γ reported at $z < 6$ in other QSO samples. Given the similar luminosity and accretion rates of the considered $z < 6$ QSOs this is an indication of redshift evolution for the properties of QSOs at EoR. These $z > 6$ quasars have a different regime for their nuclear properties. Our results is in agreement with HYPERION analysis by Zappacosta et al. (2023) who use a different approach and a different sample, hence providing firm, unambiguous confirmation of this result.

To account for any alternative interpretation of the spectral steepness we evaluate the presence of a low energy cutoff in the power-law model which enters at these high redshifts the probed energy band and mimicks the steepening of the spectrum. This measured cutoff-energy is very low and almost unreported for the entire AGN population. The value of $E_{cut} \approx 25.6$ keV is the lowest found in QSOs. A similar interpretation would still confirm the peculiar regime of the X-ray properties of $z > 6$ QSOs.

We do not find significant deviations over the power-law models considered here. Apart from a low significance (90% confidence interval) excess of counts seen around 20-30 keV whose origin (physical or instrumental) is still unknown.

We think that the steep spectral continuum we are measuring might be an indication of peculiar properties on the disk-corona system. Possibly this is an indication that these sources are very highly accreting at close or above super Eddington rate and in this case there is a large release of soft UV photons from the accretion disk which enhances the Compton cooling of the corona reprocessing them in the X-rays. So this makes the corona cooler (lower temperature). A steep power-law spectrum or the presence of a low energy cutoff in these spectra is the typical sign of a low temperature corona.

The result has important implications at high$-z$, since the great majority of broad-line lower luminosity AGN discovered by *JWST* at $z = 6$ - 10 do not show the expected X-ray emission. This indicates that these sources are faint at the probed high energy rest-frame X-ray band (i.e. $>$ 10 keV). Having steep spectra at high redshift (as we find here) is a way to have faint $>$ 10 keV X-ray emission and therefore explain the

X-ray weakness in these sources.

Bibliography

Abdo, A., Ackermann, M., Ajello, M., Atwood, W., Baldini, L., Ballet, J., Barbiellini, G., Bastieri, D., Baughman, B., Bechtol, K., et al. (2010). Fermi large area telescope view of the core of the radio galaxy centaurus a. *The Astrophysical Journal*, 719(2):1433.

Abel, T., Bryan, G. L., and Norman, M. L. (2002). The formation of the first star in the universe. *science*, 295(5552):93–98.

Abramowicz, M. A. and Fragile, P. C. (2013). Foundations of black hole accretion disk theory. *Living Reviews in Relativity*, 16:1–88.

Ai, Y., Fabian, A., Fan, X., Walker, S., Ghisellini, G., Sbarrato, T., Dou, L., Wang, F., Wu, X.-B., and Feng, L. (2017). Xmm–newton observation of the ultraluminous quasar sdss j010013. 02+ 280225.8 at redshift 6.326. *Monthly Notices of the Royal Astronomical Society*, 470(2):1587–1592.

Ananna, T. T., Bogdán, Á., Kovács, O. E., Natarajan, P., and Hickox, R. C. (2024). X-ray view of little red dots: Do they host supermassive black holes? *arXiv preprint arXiv:2404.19010*.

Antonucci, R. and Miller, J. (1985). Spectropolarimetry and the nature of ngc 1068. *Astrophysical Journal, Part 1 (ISSN 0004-637X), vol. 297, Oct. 15, 1985, p. 621-632.*, 297:621–632.

Arnaud, K. A. (1996). XSPEC: The First Ten Years. In Jacoby, G. H. and Barnes, J., editors, *Astronomical Data Analysis Software and Systems V*, volume 101 of *Astronomical Society of the Pacific Conference Series*, page 17.

Bahcall, J. N., Kozlovsky, B.-Z., and Salpeter, E. (1972). On the time dependence of emission-line strengths from a photoionized nebula. *Astrophysical Journal, vol. 171, p. 467*, 171:467.

Bañados, E., Venemans, B., Decarli, R., Farina, E., Mazzucchelli, C., Walter, F., Fan, X., Stern, D., Schlafly, E., Chambers, K., et al. (2016). The pan-starrs1 distant z¿ 5.6 quasar survey: more than 100 quasars within the first gyr of the universe. *The Astrophysical Journal Supplement Series*, 227(1):11.

Barnett, R., Warren, S. J., Cross, N. J. G., Mortlock, D. J., Fan, X., Wang, F., and Hewett, P. C. (2021). A complete search for redshift z 6.5 quasars in the VIKING survey. , 501(2):1663–1676.

Beckmann, V. and Shrader, C. (2012). The AGN phenomenon: open issues. In *Proceedings of "An INTEGRAL view of the high-energy sky (the first 10 years)" - 9th INTEGRAL Workshop and celebration of the 10th anniversary of the launch (INTEGRAL 2012). 15-19 October 2012. Bibliotheque Nationale de France*, page 69.

Beloborodov, A. M. (1999). Accretion disk models. *arXiv preprint astro-ph/9901108*.

Berk, D. E. V., Richards, G. T., Bauer, A., Strauss, M. A., Schneider, D. P., Heckman, T. M., York, D. G., Hall, P. B., Fan, X., Knapp, G., et al. (2001). Composite quasar spectra from the sloan digital sky survey. *The Astronomical Journal*, 122(2):549.

Bertola, E., Vignali, C., Lanzuisi, G., Dadina, M., Cappi, M., Gilli, R., Matzeu, G., Chartas, G., Piconcelli, E., and Comastri, A. (2022). The properties of the x-ray corona in the distant (z= 3.91) quasar apm 08279+ 5255. *Astronomy & Astrophysics*, 662:A98.

Bianchi, S., Guainazzi, M., Matt, G., and Bonilla, N. F. (2007). On the iwasawa-taniguchi effect of radio-quiet agn. *Astronomy & Astrophysics*, 467(1):L19–L22.

Bianchi, S., Panessa, F., Barcons, X., Carrera, F. J., La Franca, F., Matt, G., Onori, F., Wolter, A., Corral, A., Monaco, L., et al. (2012). Simultaneous x-ray and optical observations of true type 2 seyfert galaxies. *Monthly Notices of the Royal Astronomical Society*, 426(4):3225–3240.

Bischetti, M., Feruglio, C., D'Odorico, V., Arav, N., Bañados, E., Becker, G., Bosman, S., Carniani, S., Cristiani, S., Cupani, G., et al. (2022). Suppression of black-hole growth by strong outflows at redshifts 5.8–6.6. *Nature*, 605(7909):244–247.

Bischetti, M., Feruglio, C., Piconcelli, E., Duras, F., Pérez-Torres, M., Herrero, R., Venturi, G., Carniani, S., Bruni, G., Gavignaud, I., et al. (2021). The wissh quasars project-ix. cold gas content and environment of luminous qsos at z 2.4–4.7. *Astronomy & Astrophysics*, 645:A33.

Bischetti, M., Fiore, F., Feruglio, C., D'Odorico, V., Arav, N., Costa, T., Zubovas, K., Becker, G., Bosman, S. E., Cupani, G., et al. (2023). The fraction and kinematics of broad absorption line quasars across cosmic time. *The Astrophysical Journal*, 952(1):44.

Blandford, R. and McKee, C. F. (1982). Reverberation mapping of the emission line regions of seyfert galaxies and quasars. *Astrophysical Journal, Part 1, vol. 255, Apr. 15, 1982, p. 419-439. Research supported by the Alfred P. Sloan Foundation*, 255:419–439.

Blandford, R. D. and Znajek, R. L. (1977). Electromagnetic extraction of energy from Kerr black holes. , 179:433–456.

Bloom, S. D. and Marscher, A. P. (1996). An Analysis of the Synchrotron Self-Compton Model for the Multi–Wave Band Spectra of Blazars. , 461:657.

Bondi, H. (1952). On spherically symmetrical accretion. *Monthly Notices of the Royal Astronomical Society*, 112(2):195–204.

Boselli, A., Ciesla, L., Cortese, L., Buat, V., Boquien, M., Bendo, G., Boissier, S., Eales, S., Gavazzi, G., Hughes, T., et al. (2012). Far-infrared colours of nearby late-type galaxies in the herschel reference survey. *Astronomy & Astrophysics*, 540:A54.

Cackett, E. M., Bentz, M. C., and Kara, E. (2021). Reverberation mapping of active galactic nuclei: From x-ray corona to dusty torus. *Iscience*, 24(6).

Carilli, C. and Walter, F. (2013). Cool gas in high-redshift galaxies. *Annual Review of Astronomy and Astrophysics*, 51(1):105–161.

Cash, W. (1979). Parameter estimation in astronomy through application of the likelihood ratio. , 228:939–947.

Coatman, L., Hewett, P. C., Banerji, M., Richards, G. T., Hennawi, J. F., and Prochaska, J. X. (2017). Correcting c iv-based virial black hole masses. *Monthly Notices of the Royal Astronomical Society*, 465(2):2120–2142.

Connor, T., Bañados, E., Mazzucchelli, C., Stern, D., Decarli, R., Fan, X., Farina, E. P., Lusso, E., Neeleman, M., and Walter, F. (2020). X-ray observations of a [c ii]-bright, z= 6.59 quasar/companion system. *The Astrophysical Journal*, 900(2):189.

Corral, A., Page, M., Carrera, F. J., Barcons, X., Mateos, S., Ebrero, J., Krumpe, M., Schwope, A., Tedds, J., and Watson, M. (2008). Average fe k emission from distant agn. *Astronomy & Astrophysics*, 492(1):71–80.

Crenshaw, D. M. and Kraemer, S. B. (2012). Feedback from Mass Outflows in Nearby Active Galactic Nuclei. I. Ultraviolet and X-Ray Absorbers. , 753(1):75.

Crenshaw, D. M., Kraemer, S. B., Boggess, A., Maran, S. P., Mushotzky, R. F., and Wu, C.-C. (1999). Intrinsic absorption lines in seyfert 1 galaxies. i. ultraviolet spectra from the hubble space telescope. *The Astrophysical Journal*, 516(2):750.

Dadina, M. (2008). Seyfert galaxies in the local universe (z 0.1): the average x-ray spectrum as seen by bepposax. *Astronomy & Astrophysics*, 485(2):417–424.

De Rosa, G., Decarli, R., Walter, F., Fan, X., Jiang, L., Kurk, J., Pasquali, A., and Rix, H.-W. (2011). Evidence for non-evolving fe ii/mg ii ratios in rapidly accreting z 6 qsos. *The Astrophysical Journal*, 739(2):56.

De Rosa, G., Decarli, R., Walter, F., Fan, X., Jiang, L., Kurk, J., Pasquali, A., and Rix, H. W. (2011). Evidence for Non-evolving Fe II/Mg II Ratios in Rapidly Accreting z ~6 QSOs. , 739(2):56.

De Rosa, G., Venemans, B. P., Decarli, R., Gennaro, M., Simcoe, R. A., Dietrich, M., Peterson, B. M., Walter, F., Frank, S., McMahon, R. G., et al. (2014). Black hole mass estimates and emission-line properties of a sample of redshift z¿ 6.5 quasars. *The Astrophysical Journal*, 790(2):145.

Den Herder, J., Brinkman, A., Kahn, S., Branduardi-Raymont, G., Thomsen, K., Aarts, H., Audard, M., Bixler, J., den Boggende, A., Cottam, J., et al. (2001). The reflection grating spectrometer on board xmm-newton. *Astronomy & Astrophysics*, 365(1):L7–L17.

Duras, F., Bongiorno, A., Ricci, F., Piconcelli, E., Shankar, F., Lusso, E., Bianchi, S., Fiore, F., Maiolino, R., Marconi, A., et al. (2020). Universal bolometric corrections for active galactic nuclei over seven luminosity decades. *Astronomy & Astrophysics*, 636:A73.

Eddington, A. S. (1920). The meaning of matter and the laws of nature according to the theory of relativity. *Mind*, 29(114):145–158.

Elvis, M. (2000). A structure for quasars. *The Astrophysical Journal*, 545(1):63.

Fabian, A., Lohfink, A., Belmont, R., Malzac, J., and Coppi, P. (2017). Properties of agn coronae in the nustar era–ii. hybrid plasma. *Monthly Notices of the Royal Astronomical Society*, 467(3):2566–2570.

Fan, X., Bañados, E., and Simcoe, R. A. (2023). Quasars and the intergalactic medium at cosmic dawn. *Annual Review of Astronomy and Astrophysics*, 61(1):373–426.

Fan, X., Strauss, M. A., Becker, R. H., White, R. L., Gunn, J. E., Knapp, G. R., Richards, G. T., Schneider, D. P., Brinkmann, J., and Fukugita, M. (2006). Constraining the evolution of the ionizing background and the epoch of reionization with z 6 quasars. ii. a sample of 19 quasars. *The Astronomical Journal*, 132(1):117.

Fan, X., White, R. L., Davis, M., Becker, R. H., Strauss, M. A., Haiman, Z., Schneider, D. P., Gregg, M. D., Gunn, J. E., Knapp, G. R., et al. (2000). The discovery of a luminous z= 5.80 quasar from the sloan digital sky survey. *The Astronomical Journal*, 120(3):1167.

Fanaroff, B. L. and Riley, J. M. (1974). The morphology of extragalactic radio sources of high and low luminosity. *Monthly Notices of the Royal Astronomical Society*, 167(1):31P–36P.

Farina, E. P., Schindler, J.-T., Walter, F., Bañados, E., Davies, F. B., Decarli, R., Eilers, A.-C., Fan, X., Hennawi, J. F., Mazzucchelli, C., et al. (2022). The x–shooter/alma sample of quasars in the epoch of reionization. ii. black hole masses, eddington ratios, and the formation of the first quasars. *The Astrophysical Journal*, 941(2):106.

Feruglio, C., Fiore, F., Carniani, S., Maiolino, R., D'Odorico, V., Luminari, A., Barai, P., Bischetti, M., Bongiorno, A., Cristiani, S., et al. (2018). The dense molecular gas in the z 6 qso sdss j231038. 88+ 185519.7 resolved by alma. *Astronomy & Astrophysics*, 619:A39.

Feruglio, C., Maio, U., Tripodi, R., Winters, J. M., Zappacosta, L., Bischetti, M., Civano, F., Carniani, S., D'Odorico, V., Fiore, F., et al. (2023). First constraints on dense molecular gas at z= 7.5149 from the quasar pōniuā 'ena. *The Astrophysical Journal Letters*, 954(1):L10.

Fukumura, K., Dadina, M., Matzeu, G., Tombesi, F., Shrader, C., and Kazanas, D. (2022). Tell-tale spectral signatures of mhd-driven ultrafast outflows in agns. *The Astrophysical Journal*, 940(1):6.

Gallerani, S., Neri, R., Maiolino, R., Martín, S., De Breuck, C., Walter, F., Caselli, P., Krips, M., Meneghetti, M., Nagao, T., et al. (2012). Resolved [cii] emission in a lensed quasar at z= 4.4. *Astronomy & Astrophysics*, 543:A114.

Ganguly, R. and Brotherton, M. S. (2008). On the fraction of quasars with outflows. *The Astrophysical Journal*, 672(1):102.

Gehrels, N. (1986). Confidence limits for small numbers of events in astrophysical data. *Astrophysical Journal, Part 1 (ISSN 0004-637X), vol. 303, April 1, 1986, p. 336-346.*, 303:336–346.

George, I. and Fabian, A. (1991). X-ray reflection from cold matter in active galactic nuclei and x-ray binaries. *Monthly Notices of the Royal Astronomical Society*, 249(2):352–367.

George, I., Turner, T., Netzer, H., Nandra, K., Mushotzky, R., and Yaqoob, T. (1998).

Asca observations of seyfert 1 galaxies. iii. the evidence for absorption and emission due to photoionized gas. *The Astrophysical Journal Supplement Series*, 114(1):73.

Ghisellini, G., Haardt, F., and Matt, G. (1994). The contribution of the obscuring torus to the x-ray spectrum of seyfert galaxies: a test for the unification model. *Monthly Notices of the Royal Astronomical Society*, 267(3):743–754.

Gillessen, S., Eisenhauer, F., Fritz, T., Bartko, H., Dodds-Eden, K., Pfuhl, O., Ott, T., and Genzel, R. (2009). The orbit of the star s2 around sgr a* from very large telescope and keck data. *The Astrophysical Journal*, 707(2):L114.

Gilli, R., Comastri, A., and Hasinger, G. (2007). The synthesis of the cosmic x-ray background in the chandra and xmm-newton era. *Astronomy & Astrophysics*, 463(1):79–96.

Grier, C., Peterson, B., Horne, K., Bentz, M., Pogge, R., Denney, K. e., De Rosa, G., Martini, P., Kochanek, C., Zu, Y., et al. (2013). The structure of the broad-line region in active galactic nuclei. i. reconstructed velocity-delay maps. *The Astrophysical Journal*, 764(1):47.

Gunn, J. E. and Peterson, B. A. (1965). On the density of neutral hydrogen in intergalactic space. *Astrophysical Journal, vol. 142, p. 1633-1636*, 142:1633–1636.

Holt, S. and Smith, E. (1999). After the dark ages: When galaxies were young (the universe at 2¡ z¡ 5). *After the Dark Ages: When Galaxies were Young (the Universe at 2¡ Z¡ 5)*, 470.

Iwasawa, K., Mainieri, V., Brusa, M., Comastri, A., Gilli, R., Vignali, C., Hasinger, G., Sanders, D., Cappelluti, N., Impey, C., et al. (2012). Fe k emission from active galaxies in the cosmos field. *Astronomy & Astrophysics*, 537:A86.

Iwasawa, K. and Taniguchi, Y. (1993). The x-ray baldwin effect. *Astrophysical Journal, Part 2-Letters (ISSN 0004-637X), vol. 413, no. 1, p. L15-L18.*, 413:L15–L18.

Izumi, T., Onoue, M., Matsuoka, Y., Nagao, T., Strauss, M. A., Imanishi, M., Kashikawa, N., Fujimoto, S., Kohno, K., Toba, Y., Umehata, H., Goto, T., Ueda, Y.,

Shirakata, H., Silverman, J. D., Greene, J. E., Harikane, Y., Hashimoto, Y., Ikarashi, S., Iono, D., Iwasawa, K., Lee, C.-H., Minezaki, T., Nakanishi, K., Tamura, Y., Tang, J.-J., and Taniguchi, A. (2019). Subaru High-z Exploration of Low-Luminosity Quasars (SHELLQs). VIII. A less biased view of the early co-evolution of black holes and host galaxies. , 71(6):111.

Izumi, T., Onoue, M., Shirakata, H., Nagao, T., Kohno, K., Matsuoka, Y., Imanishi, M., Strauss, M. A., Kashikawa, N., Schulze, A., Silverman, J. D., Fujimoto, S., Harikane, Y., Toba, Y., Umehata, H., Nakanishi, K., Greene, J. E., Tamura, Y., Taniguchi, A., Yamaguchi, Y., Goto, T., Hashimoto, Y., Ikarashi, S., Iono, D., Iwasawa, K., Lee, C.-H., Makiya, R., Minezaki, T., and Tang, J.-J. (2018). Subaru High-z Exploration of Low-Luminosity Quasars (SHELLQs). III. Star formation properties of the host galaxies at z 6 studied with ALMA. *Publications of the Astronomical Society of Japan*, 70(3):36.

Jiang, L., McGreer, I. D., Fan, X., Strauss, M. A., Bañados, E., Becker, R. H., Bian, F., Farnsworth, K., Shen, Y., Wang, F., et al. (2016). The final sdss high-redshift quasar sample of 52 quasars at z¿ 5.7. *The Astrophysical Journal*, 833(2):222.

Jiang, Y.-F., Greene, J. E., and Ho, L. C. (2011). Black hole mass and bulge luminosity for low-mass black holes. *The Astrophysical Journal Letters*, 737(2):L45.

Johnson, J. L. and Bromm, V. (2007). The aftermath of the first stars: massive black holes. *Monthly Notices of the Royal Astronomical Society*, 374(4):1557–1568.

Johnson, J. L. and Haardt, F. (2016). The Early Growth of the First Black Holes. , 33:e007.

Just, D. W., Brandt, W., Shemmer, O., Steffen, A., Schneider, D., Chartas, G., and Garmire, G. (2007). The x-ray properties of the most luminous quasars from the sloan digital sky survey. *The Astrophysical Journal*, 665(2):1004.

Kara, E., García, J., Lohfink, A., Fabian, A., Reynolds, C., Tombesi, F., and Wilkins, D. (2017). The high-eddington nls1 ark 564 has the coolest corona. *Monthly Notices of the Royal Astronomical Society*, 468(3):3489–3498.

Kashikawa, N., Ishizaki, Y., Willott, C. J., Onoue, M., Im, M., Furusawa, H., Toshikawa, J., Ishikawa, S., Niino, Y., Shimasaku, K., et al. (2014). The subaru high-z quasar survey: discovery of faint z 6 quasars. *The Astrophysical Journal*, 798(1):28.

Kaspi, S., Smith, P. S., Netzer, H., Maoz, D., Jannuzi, B. T., and Giveon, U. (2000). Reverberation measurements for 17 quasars and the size-mass-luminosity relations in active galactic nuclei. *The Astrophysical Journal*, 533(2):631.

Kawanaka, N. and Mineshige, S. (2021). What determines the unique spectra of super-eddington accretors? origin of optically thick and low-temperature coronae in super-eddington accretion flows. *Publications of the Astronomical Society of Japan*, 73(3):630–638.

Kerr, R. P. (1963). Gravitational field of a spinning mass as an example of algebraically special metrics. *Physical review letters*, 11(5):237.

King, A. and Muldrew, S. I. (2016). Black hole winds ii: Hyper-eddington winds and feedback. *Monthly Notices of the Royal Astronomical Society*, 455(2):1211–1217.

King, A. R. and Pounds, K. A. (2003). Black hole winds. *Monthly Notices of the Royal Astronomical Society*, 345(2):657–659.

Kormendy, J. and Ho, L. C. (2013). Coevolution (Or Not) of Supermassive Black Holes and Host Galaxies. , 51(1):511–653.

Kraemer, S., Tombesi, F., and Bottorff, M. (2018). Physical conditions in ultra-fast outflows in agn. *The Astrophysical Journal*, 852(1):35.

Krawczynski, H., Muleri, F., Dovčiak, M., Veledina, A., Rodriguez Cavero, N., Svoboda, J., Ingram, A., Matt, G., Garcia, J. A., Loktev, V., et al. (2022). Polarized x-rays constrain the disk-jet geometry in the black hole x-ray binary cygnus x-1. *Science*, 378(6620):650–654.

Kubota, A. and Done, C. (2018). A physical model of the broad-band continuum of agn and its implications for the uv/x relation and optical variability. *Monthly Notices of the Royal Astronomical Society*, 480(1):1247–1262.

Lanzuisi, G., Gilli, R., Cappi, M., Dadina, M., Bianchi, S., Brusa, M., Chartas, G., Civano, F., Comastri, A., Marinucci, A., et al. (2019). Nustar measurement of coronal temperature in two luminous, high-redshift quasars. *The Astrophysical Journal Letters*, 875(2):L20.

Laor, A. and Davis, S. W. (2014). Line-driven winds and the uv turnover in agn accretion discs. *Monthly Notices of the Royal Astronomical Society*, 438(4):3024–3038.

Laurenti, M., Piconcelli, E., Zappacosta, L., Tombesi, F., Vignali, C., Bianchi, S., Marziani, P., Vagnetti, F., Bongiorno, A., Bischetti, M., et al. (2022). X-ray spectroscopic survey of highly accreting agn. *Astronomy & Astrophysics*, 657:A57.

Liu, H., Luo, B., Brandt, W., Brotherton, M. S., Gallagher, S. C., Ni, Q., Shemmer, O., and Timlin, J. (2021). On the observational difference between the accretion disk–corona connections among super-and sub-eddington accreting active galactic nuclei. *The Astrophysical Journal*, 910(2):103.

Ludlam, R., Cackett, E., Gültekin, K., Fabian, A., Gallo, L., and Miniutti, G. (2015). X-ray spectral and variability properties of low-mass active galactic nuclei. *Monthly Notices of the Royal Astronomical Society*, 447(3):2112–2122.

Lusso, E., Comastri, A., Vignali, C., Zamorani, G., Brusa, M., Gilli, R., Iwasawa, K., Salvato, M., Civano, F., Elvis, M., et al. (2010). The x-ray to optical-uv luminosity ratio of x-ray selected type 1 agn in xmm-cosmos. *Astronomy & Astrophysics*, 512:A34.

Lusso, E. and Risaliti, G. (2016). The tight relation between x-ray and ultraviolet luminosity of quasars. *The Astrophysical Journal*, 819(2):154.

Mainieri, V., Hasinger, G., Cappelluti, N., Brusa, M., Brunner, H., Civano, F., Comastri, A., Elvis, M., Finoguenov, A., Fiore, F., et al. (2007). The xmm-newton wide-field survey in the cosmos field. iv. x-ray spectral properties of active galactic nuclei. *The Astrophysical Journal Supplement Series*, 172(1):368.

Maiolino, R., Cox, P., Caselli, P., Beelen, A., Bertoldi, F., Carilli, C., Kaufman, M., Menten, K., Nagao, T., Omont, A., et al. (2005). First detection of [cii] 158 μm at high redshift: vigorous star formation in the early universe. *Astronomy & Astrophysics*, 440(2):L51–L54.

Maiolino, R., Risaliti, G., Signorini, M., Trefoloni, B., Juodzbalis, I., Scholtz, J., Uebler, H., d'Eugenio, F., Carniani, S., Fabian, A., et al. (2024). Jwst meets chandra: a large population of compton thick, feedback-free, and x-ray weak agn, with a sprinkle of sne. *arXiv preprint arXiv:2405.00504*.

Malizia, A., Molina, M., Bassani, L., Stephen, J. B., Bazzano, A., Ubertini, P., and Bird, A. J. (2014). The INTEGRAL High-energy Cut-off Distribution of Type 1 Active Galactic Nuclei. , 782(2):L25.

Malkan, M. A. and Sargent, W. L. (1982). The ultraviolet excess of seyfert 1 galaxies and quasars. *Astrophysical Journal, Part 1, vol. 254, Mar. 1, 1982, p. 22-37.*, 254:22–37.

Maraschi, L., Ghisellini, G., and Celotti, A. (1992). A Jet Model for the Gamma-Ray–emitting Blazar 3C 279. , 397:L5.

Marchesi, S., Lanzuisi, G., Civano, F., Iwasawa, K., Suh, H., Comastri, A., Zamorani, G., Allevato, V., Griffiths, R., Miyaji, T., et al. (2016). The chandra cosmos-legacy survey: source x-ray spectral properties. *The Astrophysical Journal*, 830(2):100.

Mason, K., Breeveld, A., Much, R., Carter, M., Cordova, F., Cropper, M., Fordham, J., Huckle, H., Ho, C., Kawakami, H., et al. (2001). The xmm-newton optical/uv monitor telescope. *Astronomy & Astrophysics*, 365(1):L36–L44.

Matt, G., Guainazzi, M., and Maiolino, R. (2003). Changing look: from compton-thick to compton-thin, or the rebirth of fossil active galactic nuclei. *Monthly Notices of the Royal Astronomical Society*, 342(2):422–426.

Mazzucchelli, C., Bañados, E., Venemans, B. P., Decarli, R., Farina, E. P., Walter, F., Eilers, A. C., Rix, H. W., Simcoe, R., Stern, D., Fan, X., Schlafly, E., De Rosa, G., Hennawi, J., Chambers, K. C., Greiner, J., Burgett, W., Draper, P. W., Kaiser, N.,

Kudritzki, R. P., Magnier, E., Metcalfe, N., Waters, C., and Wainscoat, R. J. (2017). Physical Properties of 15 Quasars at z 6.5. , 849(2):91.

McLure, R. J. and Dunlop, J. S. (2004). The cosmological evolution of quasar black hole masses. *Monthly Notices of the Royal Astronomical Society*, 352(4):1390–1404.

Medvedev, P., Gilfanov, M., Sazonov, S., Schartel, N., and Sunyaev, R. (2021). Xmm–newton observations of the extremely x-ray luminous quasar cfhqs j142952+ 544717= srge j142952. 1+ 544716 at redshift z= 6.18. *Monthly Notices of the Royal Astronomical Society*, 504(1):576–582.

Merloni, A., Alexander, D. A., Banerji, M., Boller, T., Comparat, J., Dwelly, T., Fotopoulou, S., McMahon, R., Nandra, K., Salvato, M., et al. (2019). 4most consortium survey 6: Active galactic nuclei. *arXiv preprint arXiv:1903.02472*.

Meyer, R. A., Bosman, S. E., and Ellis, R. S. (2019). New constraints on quasar evolution: broad-line velocity shifts over 1.5 z 7.5. *Monthly Notices of the Royal Astronomical Society*, 487(3):3305–3323.

Miniutti, G. and Fabian, A. (2004). A light bending model for the x-ray temporal and spectral properties of accreting black holes. *Monthly Notices of the Royal Astronomical Society*, 349(4):1435–1448.

Miniutti, G., Ponti, G., Greene, J. E., Ho, L. C., Fabian, A., and Iwasawa, K. (2009). The xmm–newton view of agn with intermediate-mass black holes. *Monthly Notices of the Royal Astronomical Society*, 394(1):443–453.

Mizumoto, M., Nomura, M., Done, C., Ohsuga, K., and Odaka, H. (2021). Uv line-driven disc wind as the origin of ultrafast outflows in agn. *Monthly Notices of the Royal Astronomical Society*, 503(1):1442–1458.

Morris, M. R., Meyer, L., and Ghez, A. M. (2012). Galactic center research: manifestations of the central black hole. *Research in Astronomy and Astrophysics*, 12(8):995.

Mortlock, D. J., Patel, M., Warren, S. J., Hewett, P. C., Venemans, B. P., McMahon, R. G., and Simpson, C. (2012). Probabilistic selection of high-redshift quasars. , 419(1):390–410.

Nandra, K. and Pounds, K. (1994). Ginga observations of the x-ray spectra of seyfert galaxies. *Monthly Notices of the Royal Astronomical Society*, 268(2):405–429.

Nanni, R., Hennawi, J. F., Wang, F., Yang, J., Schindler, J.-T., and Fan, X. (2022). Paving the way for euclid and jwst via probabilistic selection of high-redshift quasars. *Monthly Notices of the Royal Astronomical Society*, 515(3):3224–3248.

Nanni, R., Vignali, C., Gilli, R., Moretti, A., and Brandt, W. (2017). The x-ray properties of z˜ 6 luminous quasars. *Astronomy & Astrophysics*, 603:A128.

Nardini, E., Reeves, J., Gofford, J., Harrison, F., Risaliti, G., Braito, V., Costa, M., Matzeu, G., Walton, D., Behar, E., et al. (2015). Black hole feedback in the luminous quasar pds 456. *Science*, 347(6224):860–863.

Neeleman, M., Novak, M., Venemans, B. P., Walter, F., Decarli, R., Kaasinen, M., Schindler, J.-T., Bañados, E., Carilli, C. L., Drake, A. B., Fan, X., and Rix, H.-W. (2021). The Kinematics of z 6 Quasar Host Galaxies. , 911(2):141.

Neeleman, M., Novak, M., Venemans, B. P., Walter, F., Decarli, R., Kaasinen, M., Schindler, J.-T., Banados, E., Carilli, C. L., Drake, A. B., et al. (2021). The kinematics of z 6 quasar host galaxies. *The Astrophysical Journal*, 911(2):141.

Netzer, H. (1993). Ionized absorbers, ionized emitters, and the x-ray spectrum of active galactic nuclei. *Astrophysical Journal-Part 1 (ISSN 0004-637X), vol. 411, no. 2, p. 594-601.*, 411:594–601.

Netzer, H. and Laor, A. (1993). Dust in the narrow-line region of active galactic nuclei. *Astrophysical Journal, Part 2-Letters (ISSN 0004-637X), vol. 404, no. 2, p. L51-L54.*, 404:L51–L54.

Norman, C., Hasinger, G., Giacconi, R., Gilli, R., Kewley, L., Nonino, M., Rosati, P., Szokoly, G., Tozzi, P., Wang, J., et al. (2002). A classic type 2 qso. *The Astrophysical Journal*, 571(1):218.

Peterson, B., Denney, K., De Rosa, G., Grier, C., Pogge, R., Bentz, M., Kochanek, C., Vestergaard, M., Kilerci-Eser, E., Dalla Bontà, E., et al. (2013). The size of

the narrow-line-emitting region in the seyfert 1 galaxy ngc 5548 from emission-line variability. *The Astrophysical Journal*, 779(2):109.

Peterson, B. M., Ferrarese, L., Gilbert, K. M., Kaspi, S., Malkan, M. A., Maoz, D., Merritt, D., Netzer, H., Onken, C. A., Pogge, R. W., Vestergaard, M., and Wandel, A. (2004). Central Masses and Broad-Line Region Sizes of Active Galactic Nuclei. II. A Homogeneous Analysis of a Large Reverberation-Mapping Database. , 613(2):682–699.

Peterson, B. M., Somerville, R. S., and Storchi-Bergmann, T. (2010). Co-evolution of central black holes and galaxies (iau s267). *Co-Evolution of Central Black Holes and Galaxies*, 267.

Petrucci, P., Haardt, F., Maraschi, L., Grandi, P., Matt, G., Nicastro, F., Piro, L., Perola, G., and De Rosa, A. (2000). Testing comptonizing coronae on a long bepposax observation of the seyfert 1 galaxy ngc 5548. *The Astrophysical Journal*, 540(1):131.

Piconcelli, E., Jimenez-Bailón, E., Guainazzi, M., Schartel, N., Rodríguez-Pascual, P., and Santos-Lleó, M. (2005). The xmm-newton view of pg quasars-i. x-ray continuum and absorption. *Astronomy & Astrophysics*, 432(1):15–30.

Polletta, M. d., Wilkes, B. J., Siana, B., Lonsdale, C. J., Kilgard, R., Smith, H. E., Kim, D.-W., Owen, F., Efstathiou, A., Jarrett, T., et al. (2006). Chandra and spitzer unveil heavily obscured quasars in the swire/chandra survey. *arXiv preprint astro-ph/0602228*.

Pons, E., McMahon, R. G., Simcoe, R. A., Banerji, M., Hewett, P. C., and Reed, S. L. (2019). A new bright z = 6.82 quasar discovered with VISTA: VHS J0411-0907. , 484(4):5142–5154.

Pons, E., McMahon, R. G., Simcoe, R. A., Banerji, M., Hewett, P. C., and Reed, S. L. (2019). A new bright z= 6.82 quasar discovered with vista: Vhs j0411–0907. *Monthly Notices of the Royal Astronomical Society*, 484(4):5142–5154.

Pounds, K., Done, C., and Osborne, J. (1995). Re 1034+ 39: a high-state seyfert galaxy? *Monthly Notices of the Royal Astronomical Society*, 277(1):L5–L10.

Pounds, K. A., Reeves, J., King, A. R., Page, K. L., O'Brien, P. T., and Turner, M. J. (2003). A high-velocity ionized outflow and xuv photosphere in the narrow emission line quasar pg1211+ 143. *Monthly Notices of the Royal Astronomical Society*, 345(3):705–713.

Proga, D. (2005). How much x-ray and uv radiation processes are coupled in accretion disks? the active galactic nucleus case. *The Astrophysical Journal*, 630(1):L9.

Reed, S. L., Banerji, M., Becker, G., Hewett, P. C., Martini, P., McMahon, R., Pons, E., Rauch, M., Abbott, T., Allam, S., et al. (2019). Three new vhs–des quasars at 6.7¡ z¡ 6.9 and emission line properties at z¿ 6.5. *Monthly Notices of the Royal Astronomical Society*, 487(2):1874–1885.

Reed, S. L., McMahon, R. G., Martini, P., Banerji, M., Auger, M., Hewett, P. C., Koposov, S. E., Gibbons, S. L. J., Gonzalez-Solares, E., Ostrovski, F., Tie, S. S., Abdalla, F. B., Allam, S., Benoit-Lévy, A., Bertin, E., Brooks, D., Buckley-Geer, E., Burke, D. L., Carnero Rosell, A., Carrasco Kind, M., Carretero, J., da Costa, L. N., DePoy, D. L., Desai, S., Diehl, H. T., Doel, P., Evrard, A. E., Finley, D. A., Flaugher, B., Fosalba, P., Frieman, J., García-Bellido, J., Gaztanaga, E., Goldstein, D. A., Gruen, D., Gruendl, R. A., Gutierrez, G., James, D. J., Kuehn, K., Kuropatkin, N., Lahav, O., Lima, M., Maia, M. A. G., Marshall, J. L., Melchior, P., Miller, C. J., Miquel, R., Nord, B., Ogando, R., Plazas, A. A., Romer, A. K., Sanchez, E., Scarpine, V., Schubnell, M., Sevilla-Noarbe, I., Smith, R. C., Sobreira, F., Suchyta, E., Swanson, M. E. C., Tarle, G., Tucker, D. L., Walker, A. R., and Wester, W. (2017). Eight new luminous z $\geq$ 6 quasars discovered via SED model fitting of VISTA, WISE and Dark Energy Survey Year 1 observations. , 468(4):4702–4718.

Reeves, J., O'Brien, P., Braito, V., Behar, E., Miller, L., Turner, T., Fabian, A., Kaspi, S., Mushotzky, R., and Ward, M. (2009). A compton-thick wind in the high-luminosity quasar, pds 456. *The Astrophysical Journal*, 701(1):493.

Reichert, G. A., Rodriguez-Pascual, P. M., Alloin, D., Clavel, J., Crenshaw, D. M., Kriss, G. A., Krolik, J. H., Malkan, M. A., Netzer, H., Peterson, B. M., Wamsteker, W., Altamore, A., Altieri, B., Anderson, K. S., Blackwell, J. H., J., Boisson, C.,

Brosch, N., Carone, T. E., Dietrich, M., England, M. N., Evans, I. N., Filippenko, A. V., Gaskell, C. M., Goad, M., Gondhalekar, P. M., Horne, K., Kazanas, D., Kollatschny, W., Koratkar, A. P., Korista, K. T., MacAlpine, G. M., Maoz, D., Mazeh, T., McCollum, B., Miller, H. R., Mendes de Oliveira, C., O'Brien, P. T., Pastoriza, M. G., Pelat, D., Perez, E., Perola, G. C., Pogge, R. W., Ptak, R. L., Recondo-Gonzalez, M. C., Rodriguez-Espinosa, J., Rosenblatt, E. I., Sadun, A. C., Santos-Lleo, M., Shields, J. C., Shrader, C. R., Shull, J. M., Simkin, S. M., Sitko, M. L., Snijders, M. A. J., Sparke, L. S., Stirpe, G. M., Stoner, R., Storchi-Bergmann, T., Sun, W. H., Wang, T., Welsh, W. F., White, R. J., Winge, C., and Zheng, W. (1994). Steps toward Determination of the Size and Structure of the Broad-Line Region in Active Galactic Nuclei. V. Variability of the Ultraviolet Continuum and Emission Lines of NGC 3783. , 425:582.

Reynolds, C. S. and Nowak, M. A. (2003). Fluorescent iron lines as a probe of astrophysical black hole systems. *Physics Reports*, 377(6):389–466.

Richards, G. T., Kruczek, N. E., Gallagher, S., Hall, P. B., Hewett, P. C., Leighly, K. M., Deo, R. P., Kratzer, R. M., and Shen, Y. (2011). Unification of luminous type 1 quasars through c iv emission. *The Astronomical Journal*, 141(5):167.

Richards, G. T., Lacy, M., Storrie-Lombardi, L. J., Hall, P. B., Gallagher, S., Hines, D. C., Fan, X., Papovich, C., Berk, D. E. V., Trammell, G. B., et al. (2006). Spectral energy distributions and multiwavelength selection of type 1 quasars. *The Astrophysical Journal Supplement Series*, 166(2):470.

Risaliti, G. and Elvis, M. (2004). A panchromatic view of agn. In *Supermassive Black Holes in the Distant Universe*, pages 187–224. Springer.

Risaliti, G., Maiolino, R., and Salvati, M. (1999). The distribution of absorbing column densities among seyfert 2 galaxies. *The Astrophysical Journal*, 522(1):157.

Sanders, D., Phinney, E., Neugebauer, G., Soifer, B., and Matthews, K. (1989). Continuum energy distribution of quasars-shapes and origins. *Astrophysical Journal, Part 1 (ISSN 0004-637X), vol. 347, Dec. 1, 1989, p. 29-51. Research supported by NASA IRAS Extended Mission Program and Irvine Foundation.*, 347:29–51.

Schindler, J.-T., Farina, E., Banados, E., Eilers, A.-C., Hennawi, J., Onoue, M., Venemans, B., Walter, F., Wang, F., Davies, F., et al. (2022). Vizier online data catalog: X-shooter/alma qsos at 5.78¡ z¡ 7.54. i. nir sp.(schindler+, 2020). *VizieR Online Data Catalog*, pages J–ApJ.

Schmidt, M. and Green, R. F. (1983). Quasar evolution derived from the Palomar bright quasar survey and other complete quasar surveys. , 269:352–374.

Shakura, N. I. and Sunyaev, R. A. (1973). Black holes in binary systems. Observational appearance. , 24:337–355.

Shemmer, O., Brandt, W., Netzer, H., Maiolino, R., and Kaspi, S. (2008). The hard x-ray spectrum as a probe for black hole growth in radio-quiet active galactic nuclei. *The Astrophysical Journal*, 682(1):81.

Shemmer, O., Brandt, W., Schneider, D. P., Fan, X., Strauss, M. A., Diamond-Stanic, A. M., Richards, G. T., Anderson, S. F., Gunn, J. E., and Brinkmann, J. (2006). Chandra observations of the highest redshift quasars from the sloan digital sky survey. *The Astrophysical Journal*, 644(1):86.

Shen, Y., Greene, J. E., Strauss, M. A., Richards, G. T., and Schneider, D. P. (2008). Biases in virial black hole masses: an sdss perspective. *The Astrophysical Journal*, 680(1):169.

Shen, Y. and Liu, X. (2012). Comparing single-epoch virial black hole mass estimators for luminous quasars. *The Astrophysical Journal*, 753(2):125.

Shen, Y., Richards, G. T., Strauss, M. A., Hall, P. B., Schneider, D. P., Snedden, S., Bizyaev, D., Brewington, H., Malanushenko, V., Malanushenko, E., et al. (2011). A catalog of quasar properties from sloan digital sky survey data release 7. *The Astrophysical Journal Supplement Series*, 194(2):45.

Shen, Y., Wu, J., Jiang, L., Bañados, E., Fan, X., Ho, L. C., Riechers, D. A., Strauss, M. A., Venemans, B., Vestergaard, M., et al. (2019). Gemini gnirs near-infrared spectroscopy of 50 quasars at z 5.7. *The Astrophysical Journal*, 873(1):35.

Shields, G. (1978). Thermal continuum from accretion disks in quasars. *Nature*, 272(5655):706–708.

Soldi, S., Türler, M., Paltani, S., Aller, H. D., Aller, M. F., Burki, G., Chernyakova, M., Lähteenmäki, A., McHardy, I. M., Robson, E. I., Staubert, R., Tornikoski, M., Walter, R., and Courvoisier, T. J. L. (2008). The multiwavelength variability of 3C 273. , 486(2):411–425.

Stark, D. P. (2016). Galaxies in the first billion years after the big bang. *Annual Review of Astronomy and Astrophysics*, 54(1):761–803.

Steffen, A. T., Strateva, I., Brandt, W., Alexander, D., Koekemoer, A., Lehmer, B., Schneider, D., and Vignali, C. (2006). The x-ray-to-optical properties of optically selected active galaxies over wide luminosity and redshift ranges. *The Astronomical Journal*, 131(6):2826.

Strüder, L., Briel, U., Dennerl, K., Hartmann, R., Kendziorra, E., Meidinger, N., Pfeffermann, E., Reppin, C., Aschenbach, B., Bornemann, W., et al. (2001). The european photon imaging camera on xmm-newton: the pn-ccd camera. *Astronomy & Astrophysics*, 365(1):L18–L26.

Svensson, R. (1984). Steady mildly relativistic thermal plasmas: processes and properties. *Monthly Notices of the Royal Astronomical Society*, 209(2):175–208.

Thorne, K. S. (1974). Disk-accretion onto a black hole. ii. evolution of the hole. *Astrophysical Journal, Vol. 191, pp. 507-520 (1974)*, 191:507–520.

Tombesi, F., Cappi, M., Reeves, J., Palumbo, G., Braito, V., and Dadina, M. (2011a). Evidence for ultra-fast outflows in radio-quiet active galactic nuclei. ii. detailed photoionization modeling of fe k-shell absorption lines. *The Astrophysical Journal*, 742(1):44.

Tombesi, F., Cappi, M., Reeves, J., Palumbo, G., Yaqoob, T., Braito, V., and Dadina, M. (2010). Evidence for ultra-fast outflows in radio-quiet agns-i. detection and statistical incidence of fe k-shell absorption lines. *Astronomy & Astrophysics*, 521:A57.

Tombesi, F., Sambruna, R., Reeves, J., Reynolds, C., and Braito, V. (2011b). X-ray evidence for the accretion disc–outflow connection in 3c 111. *Monthly Notices of the Royal Astronomical Society: Letters*, 418(1):L89–L93.

Tortosa, A., Bianchi, S., Marinucci, A., Matt, G., and Petrucci, P.-O. (2018). A nustar census of coronal parameters in seyfert galaxies. *Astronomy & Astrophysics*, 614:A37.

Tortosa, A., Marinucci, A., Matt, G., Bianchi, S., La Franca, F., Ballantyne, D., Boorman, P., Fabian, A., Farrah, D., Fuerst, F., et al. (2017). Broad-band x-ray spectral analysis of the seyfert 1 galaxy grs 1734- 292. *Monthly Notices of the Royal Astronomical Society*, 466(4):4193–4200.

Tortosa, A., Ricci, C., Ho, L. C., Tombesi, F., Du, P., Inayoshi, K., Wang, J.-M., Shangguan, J., and Li, R. (2023). Systematic broad-band x-ray study of super-eddington accretion on to supermassive black holes–i. x-ray continuum. *Monthly Notices of the Royal Astronomical Society*, 519(4):6267–6283.

Trakhtenbrot, B., Lira, P., Netzer, H., Cicone, C., Maiolino, R., and Shemmer, O. (2017). Alma observations show major mergers among the host galaxies of fast-growing, high-redshift, supermassive black holes. *The Astrophysical Journal*, 836(1):8.

Trefoloni, B., Lusso, E., Nardini, E., Risaliti, G., Bargiacchi, G., Bisogni, S., Civano, F. M., Elvis, M., Fabbiano, G., Gilli, R., et al. (2023). The most luminous blue quasars at 3.0¡ z¡ 3.3-iii. lbt spectra and accretion parameters. *Astronomy & Astrophysics*, 677:A111.

Tripodi, R., Feruglio, C., Fiore, F., Bischetti, M., D'Odorico, V., Carniani, S., Cristiani, S., Gallerani, S., Maiolino, R., Marconi, A., et al. (2022). Black hole and host galaxy growth in an isolated z 6 qso observed with alma. *Astronomy & Astrophysics*, 665:A107.

Tripodi, R., Feruglio, C., Kemper, F., Civano, F., Costa, T., Elvis, M., Bischetti, M., Carniani, S., Di Mascia, F., D'Odorico, V., et al. (2023). Accurate dust temperature and star formation rate in the most luminous z¿ 6 quasar in the hyperluminous

quasars at the epoch of reionization (hyperion) sample. *The Astrophysical Journal Letters*, 946(2):L45.

Turner, M. J., Abbey, A., Arnaud, M., Balasini, M., Barbera, M., Belsole, E., Bennie, P., Bernard, J., Bignami, G., Boer, M., et al. (2001). The european photon imaging camera on xmm-newton: the mos cameras. *Astronomy & Astrophysics*, 365(1):L27–L35.

Turner, T., George, I., Nandra, K., and Mushotzky, R. (1997). Asca observations of type 2 seyfert galaxies. i. data analysis results. *The Astrophysical Journal Supplement Series*, 113(1):23.

Venemans, B. P., McMahon, R., Warren, S., Gonzalez-Solares, E., Hewett, P. C., Mortlock, D., Dye, S., and Sharp, R. (2007). The discovery of the first luminous z 6 quasar in the ukidss large area survey. *Monthly Notices of the Royal Astronomical Society: Letters*, 376(1):L76–L80.

Venemans, B. P., Walter, F., Decarli, R., Ferkinhoff, C., Weiß, A., Findlay, J. R., McMahon, R. G., Sutherland, W. J., and Meijerink, R. (2017). Molecular gas in three z 7 quasar host galaxies. *The Astrophysical Journal*, 845(2):154.

Venemans, B. P., Walter, F., Neeleman, M., Novak, M., Otter, J., Decarli, R., Bañados, E., Drake, A., Farina, E. P., Kaasinen, M., et al. (2020). Kiloparsec-scale alma imaging of [c ii] and dust continuum emission of 27 quasar host galaxies at z 6. *The Astrophysical Journal*, 904(2):130.

Véron-Cetty, M.-P. and Véron, P. (2003). A catalogue of quasars and active nuclei. *Astronomy & Astrophysics*, 412(2):399–403.

Vestergaard, M. (2002). Determining Central Black Hole Masses in Distant Active Galaxies. , 571(2):733–752.

Vestergaard, M. and Osmer, P. S. (2009). Mass Functions of the Active Black Holes in Distant Quasars from the Large Bright Quasar Survey, the Bright Quasar Survey, and the Color-selected Sample of the SDSS Fall Equatorial Stripe. , 699(1):800–816.

Vestergaard, M. and Peterson, B. M. (2006). Determining central black hole masses in distant active galaxies and quasars. ii. improved optical and uv scaling relationships. *The Astrophysical Journal*, 641(2):689.

Vietri, G., Piconcelli, E., Bischetti, M., Duras, F., Martocchia, S., Bongiorno, A., Marconi, A., Zappacosta, L., Bisogni, S., Bruni, G., Brusa, M., Comastri, A., Cresci, G., Feruglio, C., Giallongo, E., La Franca, F., Mainieri, V., Mannucci, F., Ricci, F., Sani, E., Testa, V., Tombesi, F., Vignali, C., and Fiore, F. (2018). The WISSH quasars project. IV. Broad line region versus kiloparsec-scale winds. , 617:A81.

Vignali, C., Brandt, W., Schneider, D., and Kaspi, S. (2005). X-ray lighthouses of the high-redshift universe. ii. further snapshot observations of the most luminous z 4 quasars with chandra. *The Astronomical Journal*, 129(6):2519.

Vito, F., Brandt, W. N., Bauer, F. E., Calura, F., Gilli, R., Luo, B., Shemmer, O., Vignali, C., Zamorani, G., Brusa, M., et al. (2019). The x-ray properties of z¿ 6 quasars: no evident evolution of accretion physics in the first gyr of the universe. *Astronomy & Astrophysics*, 630:A118.

Volonteri, M. (2010). Formation of supermassive black holes. , 18(3):279–315.

Volonteri, M., Habouzit, M., and Colpi, M. (2021). The origins of massive black holes. *Nature Reviews Physics*, 3(11):732–743.

Wachter, K., Leach, R., and Kellogg, E. (1979). Parameter estimation in x-ray astronomy using maximum likelihood. *Astrophysical Journal, Part 1, vol. 230, May 15, 1979, p. 274-287.*, 230:274–287.

Wang, F., Fan, X., Yang, J., Wu, X.-B., Yang, Q., Bian, F., McGreer, I. D., Li, J.-T., Li, Z., Ding, J., Dey, A., Dye, S., Findlay, J. R., Green, R., James, D., Jiang, L., Lang, D., Lawrence, A., Myers, A. D., Ross, N. P., Schlegel, D. J., and Shanks, T. (2017). First Discoveries of z ¿ 6 Quasars with the DECam Legacy Survey and UKIRT Hemisphere Survey. , 839(1):27.

Wang, F., Yang, J., Fan, X., Hennawi, J. F., Barth, A. J., Banados, E., Bian, F.,

Boutsia, K., Connor, T., Davies, F. B., et al. (2021). A luminous quasar at redshift 7.642. *The Astrophysical Journal Letters*, 907(1):L1.

Wang, F., Yang, J., Fan, X., Wu, X.-B., Yue, M., Li, J.-T., Bian, F., Jiang, L., Bañados, E., Schindler, J.-T., Findlay, J. R., Davies, F. B., Decarli, R., Farina, E. P., Green, R., Hennawi, J. F., Huang, Y.-H., Mazzuccheli, C., McGreer, I. D., Venemans, B., Walter, F., Dye, S., Lyke, B. W., Myers, A. D., and Nunez, E. H. (2019). Exploring Reionization-era Quasars. III. Discovery of 16 Quasars at 6.4 z 6.9 with DESI Legacy Imaging Surveys and the UKIRT Hemisphere Survey and Quasar Luminosity Function at z $\sim$ 6.7. , 884(1):30.

Wang, F., Yang, J., Fan, X., Wu, X.-B., Yue, M., Li, J.-T., Bian, F., Jiang, L., Bañados, E., Schindler, J.-T., et al. (2019). Exploring reionization-era quasars. iii. discovery of 16 quasars at 6.4 z 6.9 with desi legacy imaging surveys and the ukirt hemisphere survey and quasar luminosity function at z 6.7. *The Astrophysical Journal*, 884(1):30.

Wang, R., Carilli, C. L., Neri, R., Riechers, D. A., Wagg, J., Walter, F., Bertoldi, F., Menten, K. M., Omont, A., Cox, P., and Fan, X. (2010). Molecular gas in z 6 quasar host galaxies. *The Astrophysical Journal*, 714(1):699.

Wang, S., Brandt, W., Luo, B., Smail, I., Alexander, D., Danielson, A., Hodge, J., Karim, A., Lehmer, B., Simpson, J., et al. (2013). An alma survey of submillimeter galaxies in the extended chandra deep field-south: the agn fraction and x-ray properties of submillimeter galaxies. *The Astrophysical Journal*, 778(2):179.

Ward, M., Elvis, M., Fabbiano, G., Carleton, N., Willner, S., and Lawrence, A. (1987). The continuum of type 1 seyfert galaxies. i-a single form modified by the effects of dust. *Astrophysical Journal, Part 1 (ISSN 0004-637X), vol. 315, April 1, 1987, p. 74-91.*, 315:74–91.

Warren, S. J. and Hewett, P. C. (1990). REVIEW: The detection of high-redshift quasars. *Reports on Progress in Physics*, 53(8):1095–1135.

Wenzl, L., Schindler, J.-T., Fan, X., Andika, I. T., Banados, E., Decarli, R., Jahnke, K., Mazzucchelli, C., Onoue, M., Venemans, B. P., et al. (2021). Random forests

as a viable method to select and discover high-redshift quasars. *The Astronomical Journal*, 162(2):72.

Wilkins, D., Cackett, E., Fabian, A., and Reynolds, C. (2016). Towards modelling x-ray reverberation in agn: piecing together the extended corona. *Monthly Notices of the Royal Astronomical Society*, 458(1):200–225.

Willott, C. J., Bergeron, J., and Omont, A. (2017). A wide dispersion in star formation rate and dynamical mass of 108 solar mass black hole host galaxies at redshift 6. *The Astrophysical Journal*, 850(1):108.

Wolf, J., Nandra, K., Salvato, M., Buchner, J., Onoue, M., Liu, T., Arcodia, R., Merloni, A., Ciroi, S., Di Mille, F., et al. (2023). X-ray emission from a rapidly accreting narrow-line seyfert 1 galaxy at z= 6.56. *Astronomy & Astrophysics*, 669:A127.

Wolf, J., Nandra, K., Salvato, M., Liu, T., Buchner, J., Brusa, M., Hoang, D. N., Moss, V., Arcodia, R., Brüggen, M., et al. (2021). First constraints on the agn x-ray luminosity function at z˜ 6 from an erosita-detected quasar. *Astronomy & Astrophysics*, 647:A5.

Woo, J.-H., Treu, T., Barth, A. J., Wright, S. A., Walsh, J. L., Bentz, M. C., Martini, P., Bennert, V. N., Canalizo, G., Filippenko, A. V., et al. (2010). The lick agn monitoring project: the mbh–σ* relation for reverberation-mapped active galaxies. *The Astrophysical Journal*, 716(1):269.

Wright, E. L., Eisenhardt, P. R., Mainzer, A. K., Ressler, M. E., Cutri, R. M., Jarrett, T., Kirkpatrick, J. D., Padgett, D., McMillan, R. S., Skrutskie, M., et al. (2010). The wide-field infrared survey explorer (wise): mission description and initial on-orbit performance. *The Astronomical Journal*, 140(6):1868.

Wu, X.-B., Wang, F., Fan, X., Yi, W., Zuo, W., Bian, F., Jiang, L., McGreer, I. D., Wang, R., Yang, J., et al. (2015). An ultraluminous quasar with a twelve-billion-solar-mass black hole at redshift 6.30. *Nature*, 518(7540):512–515.

Yang, J., Wang, F., Fan, X., Barth, A., Hennawi, J., Nanni, R., Bian, F., Davies, F.,

Farina, E., Schindler, J.-T., et al. (2023). Vizier online data catalog: Nir spectroscopic obs. of z¿ 6.5 quasars (yang+, 2021). *VizieR Online Data Catalog*, pages J–ApJ.

Yang, J., Wang, F., Fan, X., Barth, A. J., Hennawi, J. F., Nanni, R., Bian, F., Davies, F. B., Farina, E. P., Schindler, J.-T., Bañados, E., Decarli, R., Eilers, A.-C., Green, R., Guo, H., Jiang, L., Li, J.-T., Venemans, B., Walter, F., Wu, X.-B., and Yue, M. (2021). Probing Early Supermassive Black Hole Growth and Quasar Evolution with Near-infrared Spectroscopy of 37 Reionization-era Quasars at 6.3 ¡ z $\leq$ 7.64. , 923(2):262.

Yang, J., Wang, F., Fan, X., Hennawi, J. F., Davies, F. B., Yue, M., Banados, E., Wu, X.-B., Venemans, B., Barth, A. J., et al. (2020). Pōniuā ‘ena: A luminous z= 7.5 quasar hosting a 1.5 billion solar mass black hole. *The Astrophysical Journal Letters*, 897(1):L14.

Zappacosta, L., Piconcelli, E., Fiore, F., Saccheo, I., Valiante, R., Vignali, C., Vito, F., Volonteri, M., Bischetti, M., Comastri, A., et al. (2023). Hyperluminous quasars at the epoch of reionization (hyperion): A new regime for the x-ray nuclear properties of the first quasars. *Astronomy & Astrophysics*, 678:A201.

Zappacosta, L., Piconcelli, E., Giustini, M., Vietri, G., Duras, F., Miniutti, G., Bischetti, M., Bongiorno, A., Brusa, M., Chiaberge, M., et al. (2020). The wissh quasars project-vii. the impact of extreme radiative field in the accretion disc and x-ray corona interplay. *Astronomy & Astrophysics*, 635:L5.

Zhang, S., Wang, T.-G., Wang, H., Zhou, H., Dong, X.-B., and Wang, J.-G. (2010). Low-z mg ii broad absorption-line quasars from the sloan digital sky survey. *The Astrophysical Journal*, 714(1):367.

Zoghbi, A., Fabian, A. C., Uttley, P., Miniutti, G., Gallo, L., Reynolds, C. S., Miller, J. M., and Ponti, G. (2010). Broad iron l line and x-ray reverberation in 1h0707-495. *Monthly Notices of the Royal Astronomical Society*, 401(4):2419–2432.